# Computational analysis of fracture and healing in thermal barrier coatings

Krishnasamy, J.

**Important note**
To cite this publication, please use the final published version (if applicable).
Please check the document version above.

# COMPUTATIONAL ANALYSIS OF FRACTURE AND HEALING IN THERMAL BARRIER COATINGS

**Jayaprakash KRISHNASAMY**

# COMPUTATIONAL ANALYSIS OF FRACTURE AND HEALING IN THERMAL BARRIER COATINGS

## Dissertation

for the purpose of obtaining the degree of doctor
at Delft University of Technology
by the authority of the Rector Magnificus, prof.dr.ir. T.H.J.J. van der Hagen,
Chair of the Board for Doctorates
to be defended publicly on
Wednesday 16 December 2020 at 17.30 o'clock

by

## Jayaprakash KRISHNASAMY

Master of Technology, Indian Institute of Technology, Bombay, India
born in Tamil Nadu, India

This dissertation has been approved by the promotors:
Prof. dr. ir. S. van der Zwaag and Dr. S. R. Turteltaub

Composition of the doctoral committee:

| | |
|---|---|
| Rector Magnificus | chairperson |
| Prof. dr. ir. S. van der Zwaag | Delft University of Technology, promotor |
| Dr. S. R. Turteltaub | Delft University of Technology, promotor |

Independent members:

| | |
|---|---|
| Prof. dr. ir. E. Schlangen | Delft University of Technology |
| Prof. dr. C. Bisagni | Delft University of Technology |
| Prof. dr. ir. A. S. J. Suiker | Eindhoven University of Technology |
| Prof. dr. T. Pardoen | Universite Catholique de Louvain, Belgium |

Other member:

| | |
|---|---|
| Dr. ir. W. G. Sloof | Delft University of Technology |

**TU**Delft

Email:  prakasjp@gmail.com

An electronic version of this dissertation is available at
http://repository.tudelft.nl/.

*To my family and teachers*

# CONTENTS

# 1

## INTRODUCTION

Modern day commercial aircraft are powered by jet engines due to their high thrust to weight ratio and efficiency. A typical jet engine consists of five main sections namely, (1) Air inlet (2) Compressor (3) Combustor (4) Turbine and (5) Exhaust nozzle. The schematic of a typical jet engine is depicted in Fig. 1.1 [1]. In the compressor, the engine inlet air is compressed to a high pressure. This high-pressure air is then mixed with fuel and burned at constant pressure in the combustor. The high energy hot gases from the combustor expand through the turbine and nozzle, through which the power necessary to propel the aircraft is extracted. Owing to the nature of the function, each section of the engine operates under a different thermo-mechanical loading environment. The temperature distribution inside a typical jet engine is shown in Fig. 1.1, where blue color represents the coldest region and the red region being the hottest. The engine intake and the compressor section are in the colder section of the engine whereas the combustor, turbine and exhaust are in the hotter regions of the engine. The peak temperature in the hot region of the typical engine is around 1500 °C [Boy12] and it occurs in the turbine section. It is worth mentioning that the thermodynamic efficiency of the turbine is directly related to the peak operating temperature under ideal conditions [Spa20]. However, the structural degradation of the turbine components sets the limiting point to this turbine operating temperature [KT80]. In order to protect the turbine component especially the turbine blades from these high temperatures, a thermal insulation coating called as Thermal Barrier Coating (TBC) [PGJ02, DMG94] is applied on the blades.

---

[1]Copyright ©GNU Free Documentation License: Permission is granted to copy, distribute and/or modify this document.
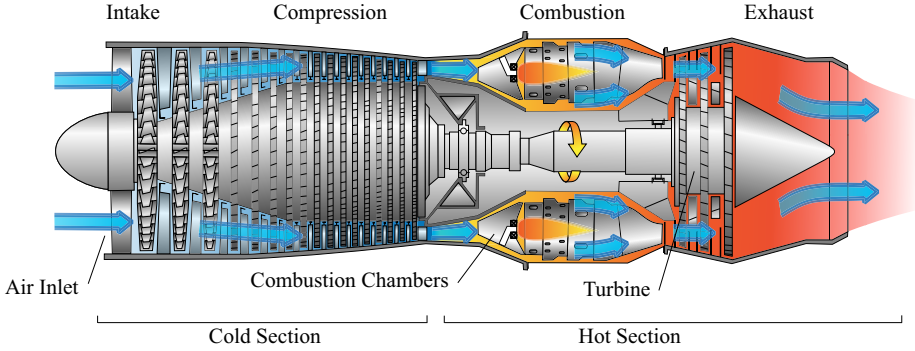
Figure 1.1: Schematic of a Jet Engine showing all the major components along with the temperature distribution[1]

**1**

## 1.1. TBC SYSTEM

A typical TBC system consists of three different layers namely, (i) a Topcoat (TC) (ii) a Thermally Grown Oxide layer (TGO) and (iii) a Bond Coat (BC) layer. The Micrographs of the TBC systems are shown in Fig. 1.2. The TC is a ceramic layer and it is usually made of Yttria Stabilized Zirconia (YSZ)[CVS04, SAK08]. It acts as a thermal insulating layer due to its very low thermal conductivity and it protects underlying the turbine blades from the high temperature gases. The BC layer is an intermediate metallic layer made of McrAlY [ET01, NSSQ09] which serves as the bonding layer between the ceramic TC and the metallic blade, providing optimal adhesion. In addition, it acts as a sacrificial layer by preventing oxidation of the underlying blade substrate. As a result of this process, a third layer called as Thermally Grrown Oxide (TGO) layer is formed between the TC and BC [TVG$^+$06, YCH$^+$08, CAHM08]. The TGO layer is a relatively thin alumina ($Al_2O_3$) layer formed due to the sacrificial oxidation of the aluminium atoms in the BC under high temperature and presence of the oxygenated atmosphere.

## 1.2. MORPHOLOGY OF TBC SYSTEM

For jet engine applications, the protective TBC layer is deposited using one of the following two techniques: Air Plasma Spray (APS) and Electron Beam Physical Vapour Deposition (EB-PVD) [Jon97, SB03]. A typical TBC coating thickness ranges from 300 to 600 $\mu$m [PGJ02, GS06, ASM05] depending on its application. As shown in Fig. 1.2, the internal microstructure of the TBC vastly differs. For instance, in EB-PVD coated TBC, the microstructure is comprised of long columnar and porous TC structure and a nearly flat interface between the TC and the TGO/BC layer[SWS02, SW05, SSFL05, SRJB07]. In contrast, the APS coated TBC consists of splats and lamellas in the TC layer along with interlamellar and intralamellar
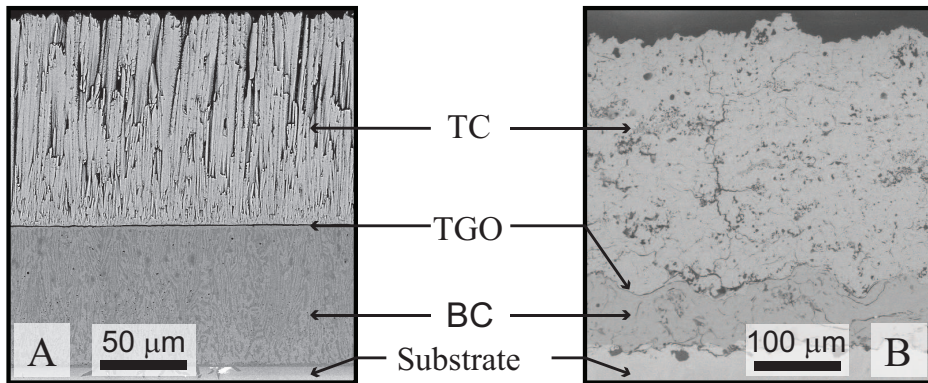
Figure 1.2: Microcraph of TBC systems where the TC and BC layer are deposited using two different deposition process (a) Electron Beam Physical Vapour Deposition (EB-PVD) (b) Air Plasma Spray (APS) [Hil09]

pores [CBMS08, Yam08, CBM09, Now14]. Further, an APS coated TBC possesses a highly wavy TC/TGO interface caused by the deformation of the substrate due to the impacting particles during deposition. Such microstructural features influence the evolution of the TBC system in terms of its failure processes and hence the lifetime. In the current research, the most commonly used APS based TBC system is considered for the study.

## 1.3. FAILURE OF TBC

The TBC system undergoes a thermal cycle during each engine start and stops as the turbine's temperature increases from ambient to operating temperature and subsequently decreases back to the ambient temperature. During each thermal cycle, the layers of the TBC system expand and shrink unequally due to a mismatch in coefficients of thermal expansion (CTE) of the TBC layers as illustrated in Fig. 1.3. The resulting thermal stresses, together with the microstructural features cause nucleation and growth of micro-cracks in the TBC system [RE00, SPJG03, KJH13, RES04]. In addition, cracking also occurs due to the thickening of the TGO layer as the oxidation of the metallic bond coat [CAHM08, YCH+08, Eva11, HTS11, NSSQ09] generates more alumina, see Fig. 1.3.a and Fig. 1.3.b. After several hundreds of thermal cycles, the micro-cracks eventually coalesce, forming a relatively large crack initially more or less parallel to the TBC-substrate interface. As large cracks deflect towards the free surface via local imperfections, the TBC separates from the substrate, which is known as spallation, as illustrated in Fig. 1.3.b. Therefore, large portions of the TC separate, which may lead to direct exposure of the critical metallic engine components to the high-temperature gases, ultimately resulting in a catastrophic failure of the entire turbine.

**1**



Uneven deformations
due to thermal cycling

TC

TGO

BC

Heating:
expansion

Cooling:
contraction

TGO growth strain

Pores

Splats

Top
Coat (TC)

Bond
Coat (BC)

micro-cracks

Thermally-
Grown
Oxide (TGO)

Spallation

TBC loading conditions

(a)

Crack coalescence and TBC failure

(b)
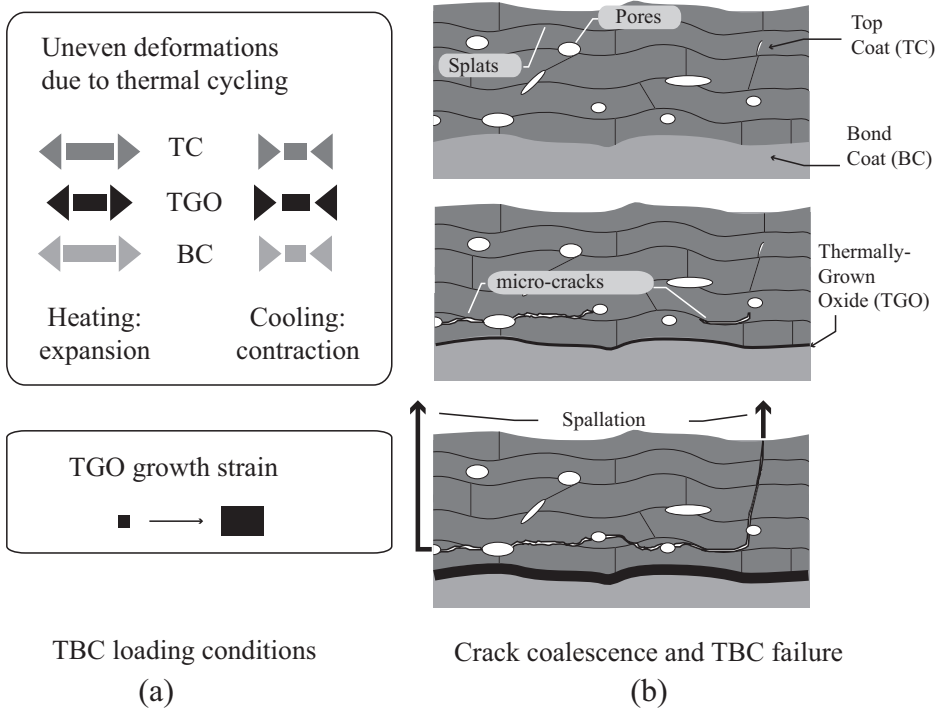
Figure 1.3: A schematic of APS TBC system showing the failure mechanisms and the governing loading
conditions

## 1.4. SELF-HEALING TBC

The lifetime of a typical system lies between 500 to 2000 cycles [LPW04, VGS09, VKS⁺10], after which, a cost and time intensive maintenance operation is necessary to replace the coating in order to continue safe operation of the engine. Numerous efforts have been made in the past to enhance the lifetime of the coating system such as changing the deposition technique, tuning the microstructure or proposing an entirely different TBC system such as using a functionally graded material for the TBC [LMK⁺14, LW19, VKS⁺10, DSZ⁺13, PLH17, GMLP17]. More recently, the concept of self-healing materials [Slo07, STD⁺15] has gained significant attention due to the promise of enhanced lifetime through incorporation of autonomous healing mechanisms in a material system. The principle of the self-healing mechanism in a TBC system is demonstrated in Fig. 1.4. A solid self-healing agent is encapsulated and embedded within the TBC topcoat layer during the coating process. When the crack induced by thermal cycling reaches the microcapsule, the capsule breaks and the oxidised self-healing agent flows into the crack, where it can further react with the matrix material and heal the crack. The best studied concept of the self-healing TBC is based on alumina ($Al_2O_3$) coated Mo-Si particles embedded in the TC layer close to the TC/BC coat interface where the micro-cracks are likely to initiate. Upon cracking in the TBC, the micro-cracks interact with the healing particles, resulting in fracture of the particles. Subsequently, the healing agent within the particles oxidises and diffuses into the crack to form a glassy silica ($SiO_2$) phase which in turn reacts with the surrounding matrix to form a load-bearing crystalline $ZrSiO_4$ (zircon) at the crack surface. The resulting healing of the micro-cracks delays the formation of a macro-crack by preventing crack coalescence which, in turn, extends the life time of the TBC system. The micrograph of the crack healing with particles containing Mo-Si is based on the formation of $SiO_2$ by oxidation when such a particle is exposed to the ambient gas at high temperature through a crack in the TBC is shown in Fig. 1.5. Further details of the above-discussed self-healing TBC system such as detailed description of the healing mechanism, type of healing particle, fabrication routes and associated challenges can be found in the following works [vdZB15, STD⁺15, DCS⁺15, NEC⁺18, NME16, CMB⁺18, CvdZS15, Pon18].

## 1.5. RESEARCH SCOPE AND OBJECTIVES

The key objective of the research present here is to develop a computational methodology to determine life time extension offered by self-healing TBC system as opposed to conventional TBC systems. The final deliverable is a modelling and analysis tool capable of simulating fracture and healing processes in the TBC system. A attention is focussed on (1) explicitly modelling the effect of TBC microstructural features such as splats and pores on fracture process, (2) simulation of the interaction of randomly dispersed healing particles with the emanating microcracks, (3) developing and implementation of crack healing model in a multiscale TBC modelling setup.
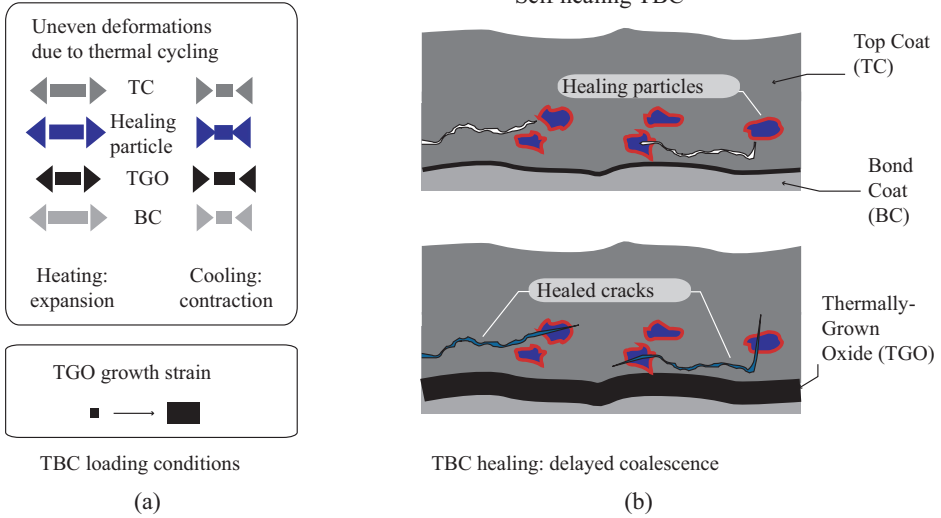
Figure 1.4: Schematic of proposed self healing TBC and its fracture behavior under given loading conditions

## MODELLING CRACK GROWTH

Nucleation and growth of microcracks will be modelled using cohesive elements and cohesive laws for each bulk material and for each interface. The choice of cohesive elements lies on their numerical robustness in complex fracture simulations involving multiple cracking and their coalescence. The fracture evolution is modelled in a multiscale framework whereby the microstructural features of the TBC such as splats, pores, TC/TGO interface waviness are explicitly taken into account.

## MODELLING TBC MICROSTRUCTURAL FEATURES

An important feature of TBC systems lies in its complex microstructure morphology characterised by the presence of pores, splats and interfaces. It is generally known that such microstructural features significantly influence the fracture evolution in TBC systems and hence their lifetime. In this thesis, the fracture evolution in TBC is modelled in a multiscale framework whereby the microstructural features such as splats, pores, TC/TGO interface waviness are explicitly taken into account. The volume fraction, size and distribution of these features are appropriately chosen using experimental evidence from collaborators obtained from microstructural images of TBC obtained using Scanning Electron Microscopy. Appropriate randomness of certain features such as the distribution of pores is taken into account in the model.
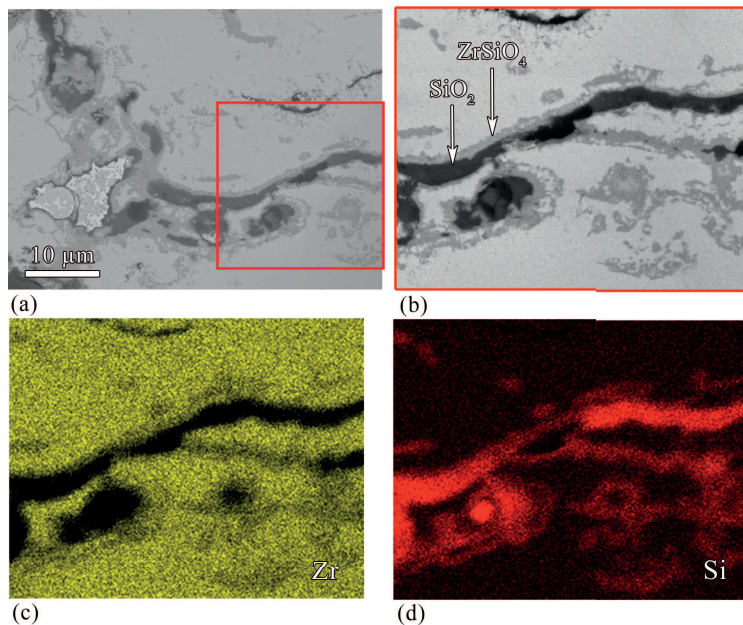
Figure 1.5: Crack Healing in YSZ TC with embedded Mo-Si healing particles after exposure at 1100$^o$C for 20 hours in air. (a) Backscattered electron image of the cross section. (b) Enlarged view of the region of interest. (c) X-ray maps of Zr distribution and (d) Si distribution. [Pon18]

## INTERACTION OF CRACK AND HEALING PARTICLES

For the successful realisation of self-healing TBC system, a key requirement is that the healing particles should attract cracks in order to trigger the healing mechanism. In the context of the TBC system under thermomechanical loading, such triggering depends upon the mismatch between the thermomechanical properties of the healing particles and the surrounding matrix. Further, it is also important to understand how introducing healing particles, which otherwise would be foreign, affects the mechanical integrity of the original TBC system without healing particles. From these perspectives, the present thesis aims to investigate the influence of the addition of healing particles and their mismatch in properties on the crack evolution.

## DEVELOPMENT OF CRACK HEALING MODEL FRAMEWORK

The next key ingredient for realising the computational tool for analysing self-healing TBC is the capability of simulating healing events and the recovery of mechanical properties upon healing. A crack healing model based on cohesive zone approach is implemented in the TBC modelling framework. The model behaviour is driven by the local crack opening displacement (COD) obtained from the simulations and activation of healing depends on availability of the healing agent, which in turn is

stimulated through appropriate COD jumps in the healed cohesive elements. The model is constructed and implemented such that multiple events of cracking and healing are automatically accounted for, wherever necessary.

### LIFETIME PREDICTIONS
The ultimate objective of lifetime prediction tool for self-healing TBC systems is achieved by integrating the above model ingredients in the multiscale framework. In addition, another key aspect, namely TGO growth, is incorporated into the framework, where the increase in the TGO thickness and the associated growth strains are modelled with growth kinetics obtained from experimental studies elsewhere. With the fully-developed modelling tool, direct numerical simulations are conducted in the TBC systems with dispersed healing particles to obtain the lifetime in terms of the number of thermal cycles to failure. Complete failure of the TBC, in the current context, is defined by the total separation of the TC (numerically 90% in the simulations), which is called spallation. Such direct full-scale simulations (in terms of explicit thermal cycles) are often more accurate as they do not rely on assumptions such as the ones required in fatigue-like models.

## 1.6. THESIS ORGANIZATION
The thesis is divided into the following chapters. Chapter 1 introduces the concept of a TBC and the associated failure mechanisms followed by proposing a new self-healing TBC system. In Chapter 2, detailed finite element simulations are conducted to investigate the effect of microstructural pores on the fracture evolution in TBC systems. This is then followed by explicit modelling of the effect of another microstructural feature, namely the splats as dealt with in Chapter 3. Chapter 4 encompasses a simulation study on evaluating the effect of mismatch in thermo-mechanical properties between healing particles and the TBC layers on the resulting fracture mechanisms. Having the above modelling capabilities, Chapter 5 focusses on development and implementation of a crack healing model with capabilities such as simulating multiple cracking, (partial or full) healing and recracking events. In the end, the final chapter (Chapter 6) summarises the results of the lifetime simulations of self-healing TBC systems, whereby life time extension offered by healing mechanisms is numerically quantified.

# 2

# COMPUTATIONAL INVESTIGATION OF POROSITY EFFECTS ON FRACTURE BEHAVIOR OF THERMAL BARRIER COATINGS

The influence of microstructural pore defects on fracture behaviour of Thermal Barrier Coatings (TBC) is analysed using finite element analysis involving cohesive elements. A concurrent multiscale approach is utilised whereby the microstructural features of the TBC are explicitly resolved within a unit cell embedded in a larger domain. Within the unit cell, a random distribution of pores is modelled along with three different layers in a TBC system, namely, the Top Coat (TC), the Bond Coat (BC) and the Thermally Grown Oxide (TGO). The TC/TGO and the TGO/BC interfaces are assumed to be sinusoidal of specified amplitude and frequency extracted from experimental observations reported in the literature. To simulate fracture in the TBC, cohesive elements are inserted throughout the inter-element boundaries in order to enable arbitrary crack initiation and propagation. A bilinear traction-separation relation with specified fracture properties for each layer is used to model the constitutive behaviour of the cohesive elements. Parametric studies are conducted for various pore geometrical features, porosity, fracture properties of Top Coat layer and Thermally Grown Oxide layer thicknesses. The results are quantified in terms of crack initiation and evolution. It is found that the presence of pores has a beneficial effect on the fracture behavior up to a certain value of porosity after which the pores become detrimental to the overall performance. Insights derived from the numerical results can help in understanding the failure behavior of practical TBC systems and

further aid in engineering the TBC microstructure for a desired fracture behavior.

## 2.1. INTRODUCTION

The failure mechanisms of the TBCs are primarily influenced by the its microstructural features [SWQ+18, LZC+17, SPJG03, ZKS+01] which are governed by processing and spraying parameters [Now14, KL09, GVS04, KVG+03, STH+98]. In air plasma sprayed TBC, the microstructure is characterized by the presence of splats, pores and pre-existing microcracks, in addition to the presence of irregular and rough interface between the layers. Various measurement techniques have been used to quantify the microstructural features, in particular pores and interface morphology of the plasma sprayed TBC [KECK18, ZBT+18, QWW+18, CGB+13, ZD05, SSW04, AIL+01]. These quantification can be further used to correlate the microstructure of the TBC with its material properties and lifetime. From an experimental viewpoint, there has been a significant interest in understanding the influence of microstructure on the thermo-mechanical properties and the lifetime of TBC [BBP+19, XRH+18, Now14, GVS04, KWN+03, WWS+11, SPK01, SK01, NQB00]. Numerical studies of defects in TBCs such as pores and pre-existing cracks, have been focussed primarily on evaluating their influence on thermal conductivity [CAVM04, GLHW01], thermo-elastic properties [GNW13, WKD+03] or stress distribution [YZW+17] using analytical and/or numerical methods

Regarding the analysis of failure in TBC systems, earlier research has been focussed on studying the relation between interface irregularities and interface crack nucleation and propagation [RfAMS11, HTS11, Bia08a]. A detailed review on finite element studies to model the thermal and the failure properties of TBC systems can be found in [WLY+16]. However, most of the existing studies do not explicitly account for the presence of the microstructural defects, in particular pores. The effect of pores on the failure of ceramics have been studied in [OAO+18]. Their analysis, however focusses on the bulk material under mechanical loading and does not include a coating system under thermo-mechanical loading. In [WFL+15], a numerical sample generated from micrographs of a real air plasma sprayed (APS) TBC, which included pores, was used to simulate its failure. However, the analysis was limited to a single sample under purely mechanical loading and therefore could not establish a systematic relation between porosity and fracture properties during thermal cycling.

It is the objective of the present research to systematically analyze the effect of pores in the TC ceramic layer on the fracture mechanisms of TBC systems in particular for the case of thermal cycling. The effect of porosity is investigated in detail using two sets of simulation. The first set refers to microstructures with controlled characteristics such as porosity, pore size distribution, pore aspect ratio and pore orientation. The goal is to study the influence of each of those features on the failure behavior of TBCs. The second set of simulations is used to study the interaction between the porosity, the fracture properties of the TC layer and the

thickness of the TGO. To minimize the influence of a specific microstructural feature, the pore size, pore orientation and pore aspect ratio are randomly distributed in the second set of simulations. The concurrent multiscale finite element setup is used for this study in order to also include free edge effect in the TBC system.

## 2.2. CONCURRENT MULTISCALE FINITE ELEMENT MODEL OF TBC

The modelling setup considered in this work is based on disk-shaped APS TBC samples used to experimentally characterize the microstructure of APS TBC coatings and to determine their lifetime upon thermal cycling [Slo] see Fig. 2.1.a. Most of the modelling approaches in the literature [KPTvdZ18, HTS11, MBF+06] utilize a computational cell where the individual layers of the TBC are modelled in detail without considering the substrate. The effect of the substrate is included through enforcing appropriate boundary conditions derived from the substrate deformation under thermal loading. In contrast, a concurrent multiscale approach is adopted in the current work which enables the effect of substrate to be accounted for directly. This modelling involves a two-scale approach in which an explicitly resolved TBC computational cell is embedded in a much larger domain of the TBC, as shown in Fig. 2.1. The explicitly modelled pores allow to perform a detailed study of their effect on TBC failure mechanisms. For simplicity, a plane strain formulation is used in the simulations. In this approach, the boundary conditions of the embedded computational cell are automatically applied by the surrounding large domain of the TBC. Furthermore, it has been experimentally observed that damage often initiates at the free edge of the sample [JEY+17, HE02, VKS01]. In order to include the free edge effect the explicitly resolved TBC computational cell is embedded at the edge of the sample, as shown in Fig.2.1.b and Fig.2.1.C.

The thickness of the TC, BC and substrate are given by $h_{TC} = 500 \ \mu m$, $h_{BC} = 200 \ \mu m$ and $h_{sub} = 5.3$ mm respectively. The radius of the disk-shaped sample is given by W = 15 mm. The width of the computational cell is w= 480 $\mu m$ which is based on the domain convergence analysis carried out in [KPTvdZ18]. The thickness of the TGO layer is taken as zero for the first set of simulations and it is varied for the second set of simulations.

In the concurrent multiscale finite element model, the microstructural features related to pores and interface roughness are considered, as highlighted in Fig.2.1. An idealized sinusoidal curve is used to model the interface morphology between the TC and the BC. The specified wavelength and amplitude for the sinusoidal interface is 60 $\mu m$ and 10 $\mu m$ respectively [KPTvdZ18]. In the outer region of the TC layer the pores are included through effective elastic properties to reduce the computational time by using a coarser mesh. The pores are modelled as ellipses randomly distributed in the TC layer of the embedded computational cell for a given volume fraction (i.e., porosity). The fracture behavior of the TBC is incorporated in the analysis using a

a.) Schematic - TBC (disk shape)

b.) Complete computational domain for concurrent multiscale TBC model

d.) FE mesh TBC detail

e.) Elliptical pore details

c.) Detailed microscale computational region
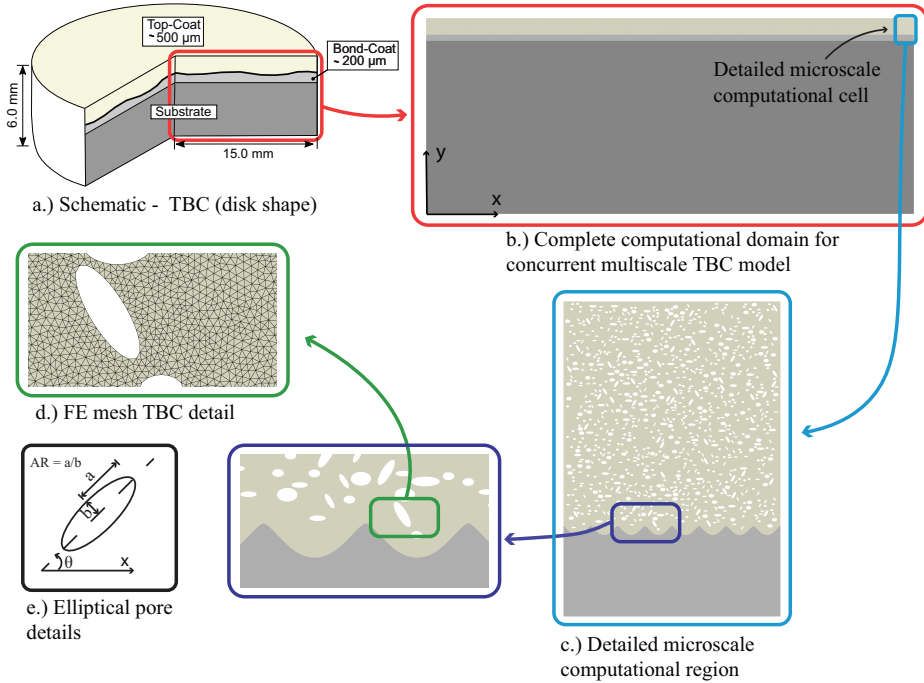
Figure 2.1: A schematic of disk-shaped TBC system and the corresponding finite element geometry

cohesive zone model that simulates fracture as a gradual phenomenon of formation of two new surfaces. It replaces the traditional crack tip stress singularity with a process zone (i.e cohesive zone) which is bounded by the cohesive strength of the material. The typical constitutive behavior of the cohesive zone model is governed by the fracture properties of the material. In the finite element framework the cohesive zone model is implemented by using a zero-thickness cohesive element. It is also important to note the fracture process is modelled in the embedded computational cell only and the outer regions of the TBC exhibits only an elastic response. The bi-linear cohesive law [HMP76] used in this work to describe the effective traction-separation behavior of the cohesive surface is shown in Fig. 2.2. The values for the maximum effective traction and area under the curve in Fig. 2.2 correspond to the fracture strength and fracture energy of the material, respectively. The initial response of the cohesive surface before damage initiation is governed by the cohesive stiffness (K). The artificial compliance introduced by the cohesive stiffness is alleviated by choosing sufficiently higher values for K. The elastic bulk response of the material is modelled using two-dimensional three-noded plane strain triangular elements. The modelling and the meshing of the finite element model is carried out using the open source software GMSH [GR09]. The cohesive elements are inserted at all the bulk
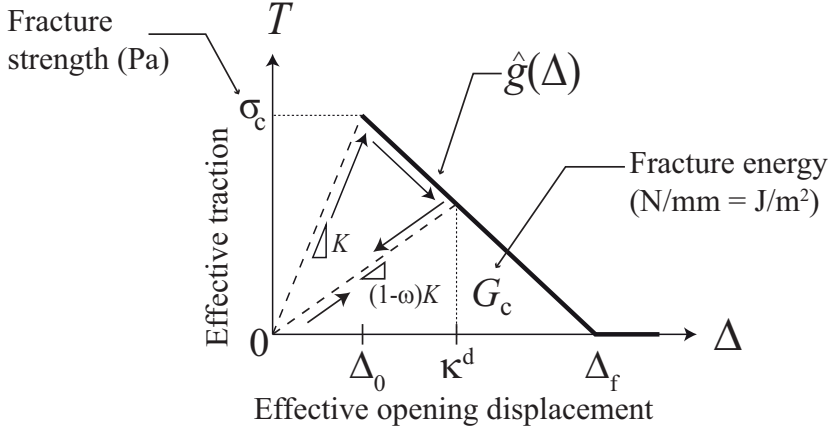
Figure 2.2: A bilinear traction-separation law to simulate the fracture process in TBC. The arrow shows the loading, damage, unloading and reloading constitutive behavior

element interfaces of the computational cell by modifying the initial finite element mesh through a MATLAB script. The process of inserting the cohesive element through out the mesh enables the arbitrary crack initiation and propagation in the computational cell which is a necessary condition to predict the failure behavior of such complex system. A fine mesh size of 1 $\mu$m is used in the computational cell region to obtain the converged fracture pattern and to resolve the extent of the cohesive zone properly. As discussed above, the elastic region of the TBC domain is coarsely meshed with a size of 150 $\mu$m to reduce the computational costs.

### 2.2.1. LOADING AND BOUNDARY CONDITIONS

A typical thermal cycle of a TBC consist of three phases namely a heating phase, a dwell phase and the cooling phase. In the heating phase, the temperature of the TBC is increased from room temperature to the operating temperature and, in the dwell phase, the temperature remains constant at the operating value. Finally, in the cooling phase, the temperature is decreased to the room temperature. The TBC is assumed to be stress-free in the dwell phase as such coatings are deposited at a temperature similar to the operating temperature. Hence, the loading condition considered is a thermal contraction (cooling phase) where the cracks are likely to initiate and grow due to thermal mismatch stresses. For the finite element simulation, temperature is gradually decreased from a typical TBC operating temperature of $1100^{o}$ C to $30^{o}$ C. In addition, the symmetry of the geometry shown in Fig. 2.1.a is utilized in the TBC finite element setup. The simulations are conducted in software

Table 2.1: Material parameters of the TBC components.

| Layers | $E$ (GPa) | $\nu$ | $\alpha$ ($10^{-6}$ 1/°C) | $\sigma_n$ (MPa) | $G_{IC}$ (N/mm) | $\gamma$ |
|--------|-----------|-------|---------------------------|------------------|-----------------|----------|
| TC | 200 | 0.15 | 12.5 | 200 | 0.008 | 4 |
| BC | 130 | 0.3 | 14.5 | 500 | 0.3 | 1 |
| TGO | 380 | 0.15 | 6 | 380 | 0.06 | 4 |
| Substrate | 200 | 0.28 | 16 | - | - | - |

package Abaqus using an implicit Newton-Raphson iterative solver. The cooling rate doesn't play a role as the simulations are based on quasi-static analysis.

### 2.2.2. CONSTITUTIVE MODELS AND MATERIAL PROPERTIES

The constitutive material behavior of the different layers of the TBC is assumed to be linear elastic and isotropic. The elastic, thermal and fracture properties used for individual layers are summarized Table 2.1. The material properties summarized in Table 2.1 corresponds to an air plasma sprayed Yttria Stabilised Zirconia (YSZ)-based TBC system. While the TC layer is composed of YSZ, the BC layer is made of NiCrAlY alloy. The TGO layer, formed during operation, is composed of alumina ($Al_2O_3$) and the substrate is a nickel alloy typically used in a aircraft gas turbine blades. The material properties of BC and the substrate are similar to the values used in earlier work [KPTvdZ18]. The elastic and fracture properties of the TC and the TGO layer are in accordance with [CB05]. Different values of normal strength $\sigma_n$ and shear strength $\sigma_s$ are used for the TC and TGO layer, defined by the parameter $\gamma$, the shear strength to the normal strength ratio. A value of $\gamma = 4$ is assumed to prevent the shear failure of TBC. This assumption is based on experimental observations of TBC failure which shows that TBC predominantly fails in mode I. The fracture toughness in mode I and mode II are also varied with same parameter $\gamma$ in the current study. The pore defects in the outer (elastic) TC layer are accounted through an effective (reduced) elastic modulus of 80 GPa. The interface between TC with BC or TGO layer is assumed to have the same fracture properties as the TGO layer.

### 2.3. RESULTS AND DISCUSSIONS

As discussed in the Sec. 2.1, two sets of analyses were conducted and the resulting fracture characteristics are discussed. The first set aims to study the effect of various microstructural features governing the TBC behavior through parametric simulations. The second set considers a TBC computational cell with randomly generated microstructural features which is used to study the interaction between the porosity, the fracture properties of the TC layer and the thickness of the TGO. The results are summarized in terms of crack initiation temperature and crack length at the end of the considered thermal cycle for each parametric case. The crack initiation

temperature is defined based on a predefined crack length (sum of the length of all failed cohesive elements) to avoid mesh dependency. Three different lengths of 1, 2 and 3 $\mu$m are considered to predict the influence of predefined crack length on crack initiation temperature. The percentage of error for the length of 2 and 3 $\mu$m is less than 5 %. Hence, the predefined total crack length of 3 $\mu$m is considered as a representative value for all the parametric simulations to define the crack initiation temperature. The cohesive element is said to be failed when it dissipated 95 % of the fracture energy. The TC layer is said to be completely failed if it becomes disconnected from the BC and/or TGO layers in the computational cell.

### 2.3.1. TBC WITH PARAMETRICALLY VARIED PORE FEATURES

In this set of analyses, various pore characteristics are varied, including size, aspect ratio, orientation and overall volume fraction (porosity) as listed in Table Table 2.2. Like any parametric analysis, while studying the influence of a given pore feature, the other features are kept constant. Five realizations, each with a distinct spatially

Table 2.2: Summary of pore geometric parameters used.

| Pore features | Geometrical Parameters |
|---|---|
| Porosity($V_f$) | 0, 10, 15, 20, 30 |
| Aspect ratio(AR) | 1.5, 3, 4.5 |
| Orientation($\theta$) | 0, 45, 90, 135 deg |
| Size | 25, 50, 100 $\mu$m$^2$ |

random pore distribution, are considered for each parametric case and the results are plotted in terms of the average along with the scatter. The results corresponding to the applied single thermal cycle are reported in terms of crack initiation temperature and total crack length.

#### EFFECT OF POROSITY

In this section, the volume fraction of the pores is varied and its influence on crack initiation temperature and total crack length are reported in Fig. 2.3. Five different pore volume fractions given by $V_f$ = 0, 10, 15, 20 and 30 % are considered. The crack initiation temperature remains almost constant for the range of porosity analyzed. In terms of crack length, the results indicate that there is an initial decrease in damage and subsequently an increase until complete failure for a porosity of 30%. The porosity of 15% appears as an optimal value in terms of crack length (less damaged configuration). Note that the fully dense TC layer shows a higher crack length compared to the porous TBC up to 20%. This is due to the fact that the presence of pores increases the TBC compliance which reduces the strain energy contribution to the crack driving force [ZYW10]. Experimental studies in the literature also revealed

a positive influence of pores, whereby it was observed that presence of the pores improved the lifetime of the TBC [KVS11].
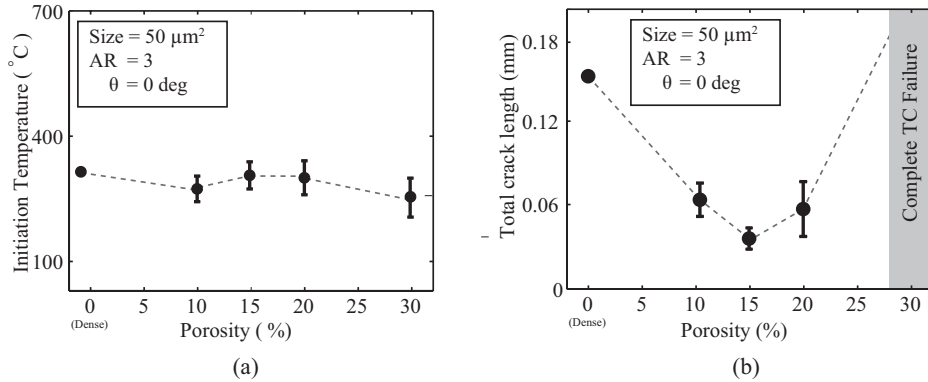


Figure 2.3: Variation of (a) crack initiation temperature and (b) total crack length for different pore volume fraction 0 (dense), 10, 15, 20 and 30 % with the fixed pore size of 50 $\mu m^2$, aspect ratio of 1.5 and orientation of 0 deg

**2**

### EFFECT OF PORE SIZE

Three different pore sizes defined by a cross-sectional pore area of 25, 50 and 100 $\mu m^2$ are considered in this analysis. The pores are assumed to be elliptical with an aspect ratio of 1.5 and an orientation angle of 0 deg. The pore volume fraction is also fixed and equal to 15%. The simulation results are presented in terms of crack initiation temperature and total crack length as shown in Fig. 2.4. For comparison purposes, the results of a fully dense TBC (defined as a zero pore size) are also plotted in Fig. 2.4. From Fig. 2.4.a, it can be observed that the crack initiation temperature increases gradually with increasing pore size, thus resulting in earlier crack initiation. When compared with a fully dense TBC (no pores),the TBC with 15 percent pore volume fraction and a pore size of 100 $\mu m$ leads to an early crack onset, i.e., the crack initiation temperature is increased from $300^o$ C to $400^o$ C. Such a trend in the crack initiation behavior can be attributed to the amplified stress concentration effects as the pore size is increased. In terms of the crack length, increasing the pore size leads to a larger crack length at the end of the cooling cycle as shown in Fig.2.4.b. It is worth noting that the crack initiation temperature increases linearly with respect to the pore size. Similar observations are also reported in [Liu97, SGD15] based on experiment study on ceramics with different pore sizes. Similarly, the crack length increases approximately linearly with increasing pore size, as seen in Fig.2.4.b. Thus, in general, it can be concluded that an increase in the pore size is generally detrimental to the TBC integrity. Nonetheless, the crack length with pores remains smaller than the fully-dense case. Hence, a 15% porosity with small pores appears to be optimal.
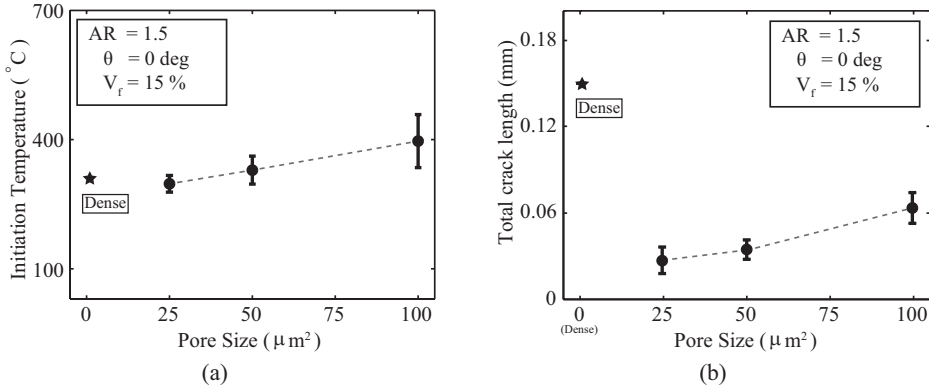
Figure 2.4: Variation of (a) crack initiation temperature and (b) total crack length for different pore size 0 (dense), 25, 50 and 100 $\mu m^2$ with the fixed pore aspect ratio of 1.5, orientation of 0 deg and volume fraction of 15%.

EFFECT OF PORE ASPECT RATIO

To investigate the effect of pore aspect ratio, three different aspect ratios are analyzed, namely 1.5, 3 and 4.5. The values for pore size, orientation and volume fractions are fixed and are given by 50 $\mu m^2$, 0 deg and 15 %, respectively. The results of the simulations are summarized in Fig. 2.5 along with the results of fully dense TBC (referred to as zero aspect ratio). A similar trend as with the effect of pore size is observed whereby the crack initiation temperature and the crack length increase with increasing pore aspect ratio. Although no experimental results for this specific parameter seem to be available in the literature, it is worth noting that, a similar type of behavior is reported for SiC ceramic materials in [LJY+18] using discrete element simulations under uni-axial compression. This observation is due to the fact that as the pore aspect ratio is increased, the stress concentration around the pores is increased leading to earlier crack initiation and increased total crack length. In other words, as the aspect ratio is increased, the pores tend to act more like a crack, resulting in easier crack initiation and propagation. Further, the stress concentrations arise due to the interaction of multiple pores in their vicinity, leading to the overall reduced integrity of the TBC.

EFFECT OF PORE ORIENTATION

Another parameter of interest is the pore orientation for elliptical pores. To study the effect of pore orientation, three different values are considered given by 0, 45, 90 and 135 degrees with 0 deg corresponding to an elliptical pore with the semi-axis oriented parallel to the TGO (see Fig. 2.1.e). The volume fraction and the aspect ratio of the pores are kept constant at 15% and 1.5 respectively.

The results obtained from the analysis from five different realizations for each
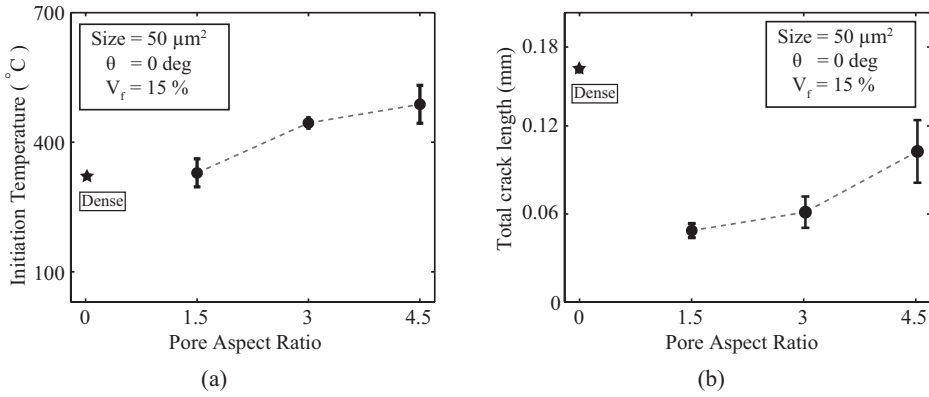
Figure 2.5: Variation of (a) crack initiation temperature and (b) total crack length for different pore aspect ratio 0 (dense), 1.5, 3 and 4.5 with the fixed pore size of 50 $\mu m^2$, orientation of 0 deg and volume fraction of 15%.
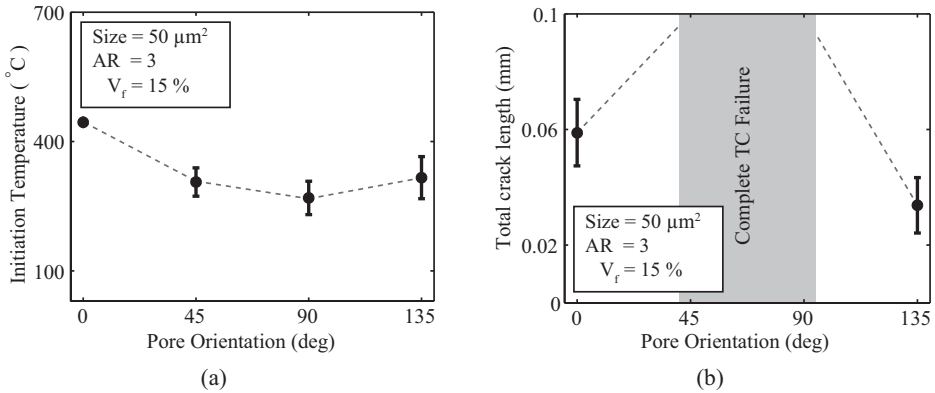


Figure 2.6: Variation of (a) crack initiation temperature and (b) total crack length for different pore orientation 0, 45, 90 and 135 deg with the fixed pore size of 50 $\mu m^2$, aspect ratio of 3 and volume fraction of 15%.

case are summarized in Fig. 2.6. Unlike in the case of pore size variations, the crack initiation temperature and in particular in crack length does not vary monotonically with the orientation angle. Increasing the pore orientation from 0 deg (horizontally oriented pores) delays the crack initiation as can be observed from Fig. 2.6.a. This is expected as the horizontally oriented pores offers a more favorable configuration for the micro cracks to originate and coalesce as compared to the more vertically aligned pores. The initiation temperature is symmetric with respect to 90 deg as expected. However, the total crack length is not symmetric, which is due to the influence of the free edge, either promoting crack extension or reducing it.

### 2.3.2. TBC WITH RANDOM MICROSTRUCTURAL PORES

In this section, a TBC computational cell is considered with random pore features that are representative of actual TBC microstructures [Slo]. The values of the pore features used in the modelling for four different porosity are given in Table 2.3. Similar to the parametric case, the pores are approximated as ellipsoidal entities with their aspect ratio, orientation and size (pore area). The pores are distributed randomly within the TBC computational cell. Five different realizations are considered for the same set of pore features given in Table 2.3 in order to study the effect of such spatially random distribution on the TBC fracture characteristics.

Table 2.3: Modelling parameters generated for random features

| Geometrical features | Modelling parameters (%) | | | |
|---|---|---|---|---|
| Porosity ($V_f$) | 10 | 15 | 20 | 30 |
| Micro-porosity [SP] (Size = 25 $\mu m^2$) | 5 | 7.5 | 5 | 15 |
| Macro-porosity [LP] (Size = 75 $\mu m^2$) | 5 | 7.5 | 15 | 15 |
| Round shaped porosity (AR = 1.5) [LP , SP] | 5 [2.5 , 2.5] | 8 [4 , 4] | 11 [8.5 , 2.5] | 16 [8 , 8] |
| Lamellar shaped porosity (AR = 3) | 5 | 7 | 9 | 4 |
| Horizontal lamellar porosity ($\theta$ =0 deg) [LP , SP] | 2.5 [1.25 , 1.25] | 3.5 [1.75 , 1.75] | 5 [1.5 , 3.5] | 7 [3.5 , 3.5] |
| Inclined lamellar porosity ($\theta$ = ±45 deg) [LP , SP] | 2.5 [1.25 , 1.25] | 3.5 [1.75 , 1.75 ] | 4 [1 , 3 ] | 7 [3.5 , 3.5] |

For each realization, the TBC system is subjected to the thermal contraction load as the temperature is decreased from 1100°C to 30°C . Stress distribution plots along with the crack evolutions at the end of the thermal loading step for one of the realizations are shown in Fig. 2.7. The insets in the figure correspond to the stress contours for the concurrent multiscale model. In particular, the figure illustrates the cracking that occurs at the TC/BC interface due to their mismatch in CTE as well as the free edge effect whereby cracking initiates at the free surface (see Fig. 2.7.c and Fig. 2.7.d). The presence of microstructural pores in the TC layer leads to a complex
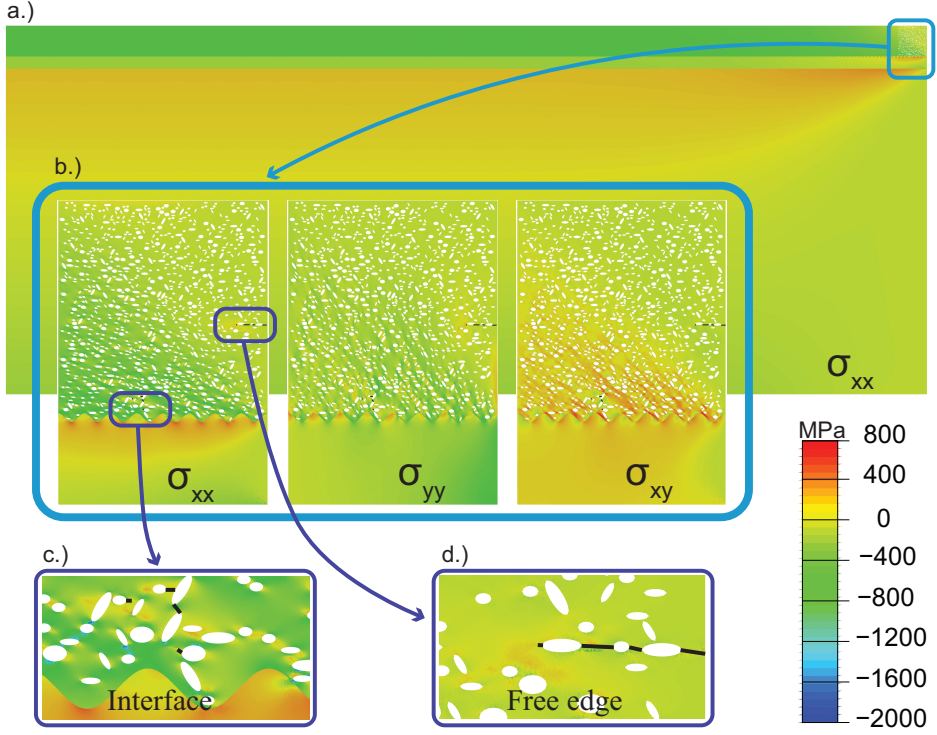
Figure 2.7: Stress distribution in TBC with realistically represented microstructural pores at T =30°C. a.) Stress variations ($\sigma_{xx}$) in the concurrent multiscale TBC model b.) Stress distribution in the TBC computational cell with explicitly modelled pores. c.) Mixed mode Cracking of interior TC layer close to BC due to pores and thermal mismatch stress. d.) Mode I cracking at the edge of the TC layer due to free edge effect.

variation in stress fields [LZC+17, YZW+17] as expected. As shown in Fig. 2.7.a and Fig. 2.7.b, the BC region close to the free edge and near the TC/BC interface is under a tensile stress in $x$ direction ($\sigma_{xx}$). On the other hand, the tensile stress in the vertical direction ($\sigma_{yy}$) arising out of the free edge and the stress concentration due to pores induces the mode I edge cracking of the TC layer [TBH+08] away from the TC/BC interface as observed in Fig. 2.7.d. The shear stress distribution ($\sigma_{xy}$) for the embedded computational cell is shown in Fig. 2.7.b which may appear to be critical especially in the lower part of the TC layer. However, as discussed in Sec. 2.2.2, higher fracture values are used for mode II, in order to prevent the shear failure of the TBC. The interior regions of the TC layer experience the formation of microcracks close to the TC/BC interface under mixed mode conditions and are shown in Fig. 2.7.c. The variation of crack initiation temperature and the total crack length with the
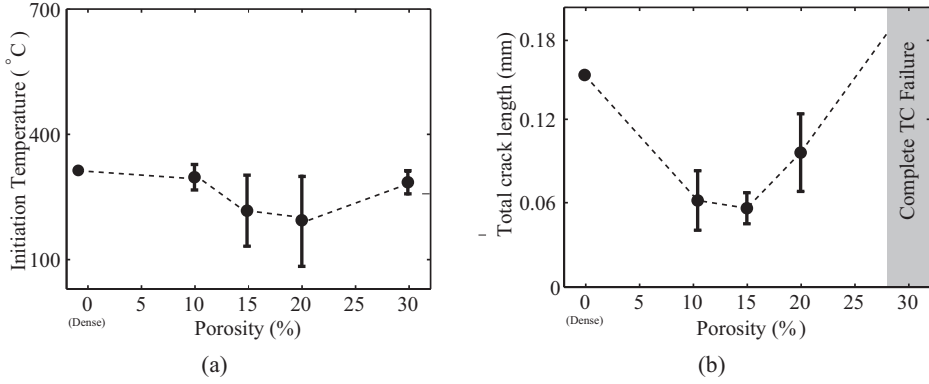
Figure 2.8: Variation of crack length with respect to loading temperature for five different realizations of TBC with the the same set of randomly represented microstructural pores.

porosity is presented in Fig. 2.8. Comparing the results shown in Fig. 2.8.a and Fig. 2.8.b with the corresponding data in Fig. 2.3.a and Fig. 2.3.b (porosity), it can be concluded that the random microstructure predicts similar values as the controlled microstructure but the scatter in the latter is higher. This may be ascribed to the fact that the random microstructure contains a mix of factors that may increase but also decrease the initiation temperature and the total crack length (i.e., the random microstructure contains pores with large but also small aspect ratios, pore sizes and various orientations).

### 2.3.3. EFFECT OF TC FRACTURE PROPERTIES

The relative fracture properties of the TC layer with respect to the other layers of the TBC system influences the fracture behavior in terms of the location and pattern of crack evolution. The effect of this parameter is studied by considering two distinct parametric sets where the fracture ratio ($f$) is varied. The fracture ratio ($f$) is defined as

$$
\begin{aligned}
\sigma^{TC} &= f\sigma_0^{TC}, \\
G^{TC} &= fG_0^{TC}
\end{aligned}
\tag{2.1}
$$

where $f$ is the fracture ratio and $\sigma_0^{TC}$ and $G_0^{TC}$ are the fracture properties of the benchmark material. Note that both properties are varied using the same fracture ratio $f$ and special attention is given to weaker materials ($f < 1$) as stronger material show limited damage.

In the first set, the normal fracture ratio ($f_n$) of the TC layer is varied with values of 0.625, 0.75, 0.875 and 1 while the shear fracture ratio ($f_s$) of the TC layer is fixed at 0.8. In the second set, the shear fracture ratio ($f_s$) is varied with values given by 0.625, 0.75, 0.875 and 1 for the normal fracture ratio ($f_n$) of 0.8. The range of TC fracture

properties considered is based on the limits of TC strength values used for porous and dense TC layer [KPTvdZ18].
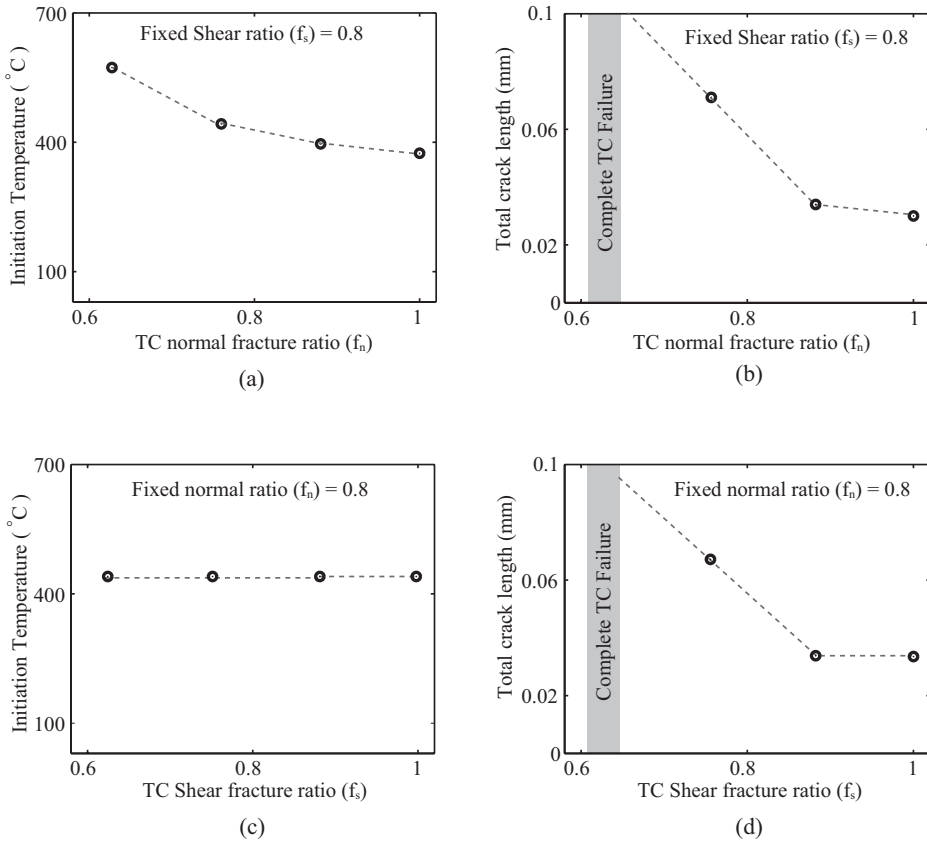


Figure 2.9: Variation of total crack length of TBC with random microstructural pores for different (a) Normal strength and (b) Shear strength values.

The results of the study are summarized in terms of crack initiation temperature and total crack length in Fig. 2.9. The results corresponding to the normal fracture ratio variation are shown in Fig. 2.9.a and Fig. 2.9.b, and those corresponding to the variation of shear fracture are shown in Fig. 2.9.c. and Fig. 2.9.d. In general, it can be observed that the increase in normal fracture ratio delays the crack initiation in the TC layer as shown in Fig. Fig. 2.9.a. In case of shear fracture ratio, the effect on crack initiation is nil (refer Fig. 2.9.c.). This is because the normal strength, being always less than the shear strength for the TC layer, dominates the crack initiation behavior. In terms of crack length, the results shown in Fig. 2.9.b and Fig. 2.9.d are sensitive to the strength ratio provided the ratio is smaller than 0.9. For instance, complete failure of
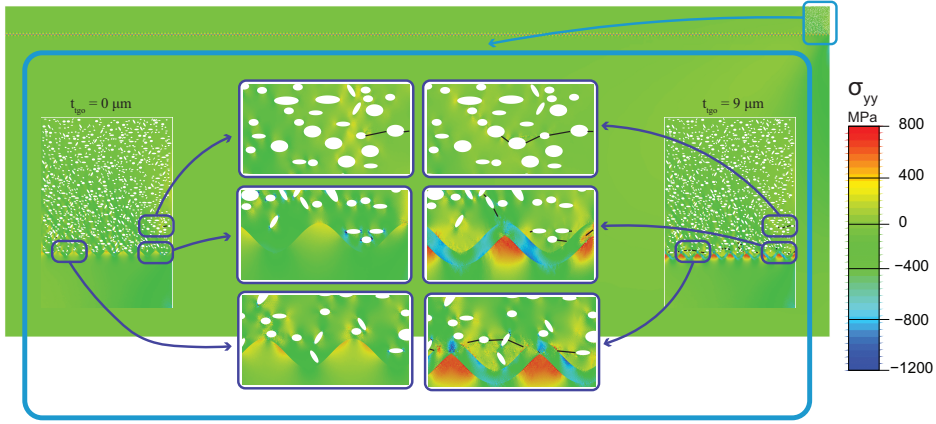
Figure 2.10: Stress distribution in TBC with random microstructural pores at T =30°C for TGO thickness of 0 $\mu$m and 9 $\mu$m

the TBC occurs when the fracture ratio is decreased below a value of 0.75 for both the cases. In terms of the crack pattern, it is observed that with a decrease in the strength, micro-cracks appear early in the TC layer. Upon the thermal loading process, the emanated micro-cracks near the TGO/TC interface tend to coalesce in the presence of stress concentrations due to the interface. Such a coalescence ultimately leads to the formation of a larger horizontal macro-crack, resulting in complete failure of the TBC. The critical fracture properties for the complete TBC failure is governed by the value of the fracture ratio with which the coalescence is favored.

### 2.3.4. EFFECT OF TGO THICKNESS

In the simulations reported above, the thickness of the TGO layer is considered to be zero which corresponds to the initial thermal cycle of a TBC system. However, during cyclic operation, the TGO layer grows to a value in the range of 8 to 12 $\mu$m before onset of delamination failure [DYL$^+$14, TBH$^+$08]. The presence of the TGO introduces additional thermal stresses due to its strong CTE mismatch with the underlying BC and TC layers, which in turn affects the crack evolution. Thus, in this section, the effect of TGO thickness on the TBC fracture behavior is investigated by considering different thickness values of the TGO, given by $t_{TGO}$= 0, 3, 6 and 9 $\mu$m. The simulations are carried out for the random pore features given in Table 2.3. Due to computational limitations, the TGO thickness values are increased based on the assumption that no cracking did occur till the thickness of the TGO increased to the specified value.

The effect of TGO thickness on the stress field and cracking behavior of the TBC is shown in Fig. 2.10 in terms of the normal stress distribution ($\sigma_{yy}$) corresponding to the TGO thickness of $t_{TGO}$= 0 $\mu$m (left inset) and 9 $\mu$m (right inset). Upon

Figure 2.11: Variation of total crack length for different TGO thickness 0, 3, 6 and 9 $\mu m$ with 15% random microstructural pores.
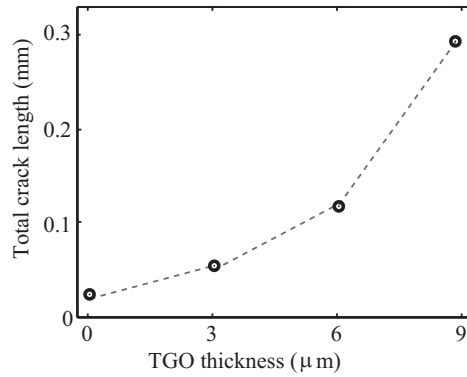
**2**

examining the stress distributions in the TBC without TGO (left inset in the figure), it can be seen that two different stress concentrations occur in the TBC, one arising due to the pores as discussed before and the other due to the presence of dissimilar layers (TC and BC). Introduction of the TGO layer amplifies the stress concentration significantly around the interface as seen in Fig. 2.10 (right inset) which is attributed to the severe CTE mismatch between the TGO and the other two layers. This, in turn, alters the crack pattern as compared to the TBC system with no TGO layer. By comparing the results with and without the TGO, several distinctive observations can be made. The first key difference is that a higher TGO thickness leads to cracking in the TGO in addition to the cracking in the TC layer. This is not only because of the additional stress concentration effects as discussed above, but also due to the altered stress distribution in the proximity of the pores near the TGO layer. Upon closer observation, it can be seen that the stress fields near the pores are largely tensile in the presence of TGO as opposed to the compressive stress state of the pores in the case with zero TGO thickness. It is interesting to note that not only the presence of TGO layer leads to micro-cracks in and around it, but also it aggravates/accelerates the crack growth in the TC region which is relatively far away from the TGO layer. However, it is also worth mentioning that the stress distributions in the TC layer sufficiently far away from the TGO layer will be largely unaffected by the presence of TGO. In situations where there are edge cracks in the TC regions far from the TGO, it can be anticipated that the crack evolution will be least affected by the presence of the TGO layer.

The results of the simulations conducted for different values of the TGO thickness are summarized in the Fig. 2.11. The total crack length is plotted as a function of the TGO thickness. From the results, it can be observed that increasing the TGO thickness decreases the integrity of the TBC system [DYL+14]. Indeed the total crack

length at the end of the thermal loading step increases approximately quadratically as a function of TGO thickness.

## **2.4.** CONCLUSIONS

The effect of microstructural porosity on the fracture behavior of the TBC is analyzed using cohesive elements-based finite element method. Geometric and material parameters such as TGO thickness, pore characteristics (such as aspect ratio, size, volume fraction and orientation), and TC fracture properties are studied through parametric analyses. Two simulation sets are considered: one with a controlled pore characteristics and one with random pore characteristics. For the controlled microstructure, the results of the parametric studies are reported in terms of the crack initiation temperature and total crack length, whereby several pore features were found to exhibit a significant influence on the failure behavior. The following conclusions are drawn from the parametric finite element investigations.

1. Porosity plays a significant role in improving the fracture resistance of the TBC. However, porosity above a critical value leads to early failure of the TBC.

2. Increasing the pore size decreases the TBC integrity where the crack initiation temperature and the crack length increase with increase in pore size. Both the crack initiation temperature and the total crack length showed a linear variation with respect to pore size

3. Pore aspect ratio exhibited a similar influence as that of the pore size, where the initiation temperature and the crack length increases with pore aspect ratio

4. The crack initiation temperature decreases with increase in pore orientation angle. In terms of the crack length, complete failure occurs for pore orientations that lie between 45 and 90 deg.

For the microstructure with random pore characteristics, the simulations indicate the following:

1. The porosity is the main parameter that predicts the total crack length compared to other pore characteristics. Nonetheless, the random distribution of pore size, pore area and pore orientation results in a large scatter in data.

2. On the effect of the material parameter, namely the TC fracture properties, the crack initiation temperature is slightly influenced. However, in terms of crack length, complete TBC failure is observed when both the normal and shear fracture are reduced to a value below a critical level.

3. The TGO thickness showed a significant effect on the failure behavior. The crack initiation temperature linearly increases with increasing TGO thickness, whereas the crack length increased quadratically.

The results and the insights could serve for understanding the effect of pore defects on failure behavior, which in turn can aid in engineering or designing the microstructure for improved performance/lifetime. To summarize the major findings to help in optimizing the TBC behavior, a porous TBC system with smaller pore size, circular pores (or if the pores are elliptical, it should have small aspect ratio), close to zero degree orientation and higher TC fracture properties would result in an optimal TBC system with enhanced thermal cycling integrity.

**2**

# 3

# NUMERICAL INVESTIGATION INTO THE EFFECT OF SPLATS AND PORES ON THE THERMAL FRACTURE OF AIR PLASMA SPRAYED THERMAL BARRIER COATINGS

The effect of splat boundaries on the fracture behavior of Air Plasma Sprayed Thermal Barrier Coatings (APS-TBC) is analyzed using finite element modelling involving cohesive elements. A concurrent multiscale approach is utilized whereby the microstructural features such as splats and pores are explicitly resolved within a computational cell embedded in a larger domain. Within the computational cell, splats are modelled as being located on a sinusoidal interface in combination with a random distribution of pores. To simulate fracture in the TBC, cohesive elements are inserted throughout the inter-element boundaries in order to enable arbitrary crack initiation and propagation. Parametric studies are conducted for different splat planarity, spacing, pore volume fraction and fracture properties of the splats. The results are quantified in terms of crack nucleation temperature and total microcrack length evolution. It is found that the presence of pores result in an improved TBC fracture behavior upto a critical volume fraction whereas the presence of splats is detrimental to the TBC performance. Splat boundaries with high planarity and spacing results in an improved fracture behavior compared to the splat boundaries with low planarity and spacing. The crack initiation temperature was found to be linearly dependent on normal fracture strength and less dependent on shear fracture

properties of the splats. However, complete failure of the TC occurs when the shear fracture properties of the splats are reduced below a critical value. Insights derived from the numerical results aid in engineering the microstructure of practical TBC systems for an improved thermal fracture behaviour.

## 3.1. INTRODUCTION

Conventional TBCs are predominantly manufactured either by an Electron Beam Physical Vapor Deposition (EB-PVD) process or the Air Plasma spray (APS) technique [FKT+08]. In EB-PVD technique, the coatings are deposited on the substrate in vacuum using a high energy electron beam [GW11]. This technique produces a uniform coating with a fine columnar grain structure. These coatings offer superior strain tolerance, thermal shock and oxidation resistance which ultimately leads to prolonged service life. In the APS method, ceramic particles are melted and sprayed onto the substrate at atmospheric pressure using plasma jet [XK11]. APS TBCs have a shorter lifetime compared to EB-PVD TBCs due to its defected and layered microstructure. However, APS remains the preferred manufacturing method in the fields of aerospace and power generation gas turbines because of its low cost and high production efficiency [AA18].

The distinctive microstructural features of APS TBCs are splats in addition to other features such as pores, microcracks and interface roughness. Splats are formed during the solidification process of the sprayed ceramic particles [WKG02]. The TC regions between the successive splats are called lamellae, the building blocks of the APS TBCs. Splats are usually weak interfaces/boundaries. The characteristics of the splats are determined by the spraying parameters [LYLL18, LDP15, LN03]. Literature studies on TBC microstructure show that the presence of splats along with microstructural pores significantly influences the material properties and failure behavior of TBC [MMM+17, WKD+03, MS12, WMS04, LYC+18].

Multiple efforts have also been undertaken in the literature to model and predict the influence of splat boundaries on thermo-elastic properties of TBCs [KWN+03, MB06, LWMF13, GZZ+19]. In [KWN+03], real microstructural images are used to predict the effective thermal conductivity and stiffness using finite element analysis. The stiffness reduction due to splats is obtained indirectly by calculating the difference between the stiffness values of finite element prediction of as-sprayed (with splats) and experimental measurements of thermal cycled (no splats) samples, respectively. Similar type of work is also carried out in [MB06] using image based extended finite element modelling. In addition, the evolution of the stress intensity factor and the quenching stress as a function of intra-splat cracks and substrate temperature is also analyzed in their study. Thermal conductivity of splat interfaces is obtained in [LWMF13] through iterative finite element computations and by mapping the calculated effective thermal conductivity with the experimental measurements. A finite element model is generated using real splat interface distribution obtained from fracture image analysis. Finite element analysis on idealized YSZ model system

to analyze the effect of splat interfaces on thermal conductivity of TBC is carried out in [GZZ$^+$19].

Literature studies to predict the influence of TBC microstructure on its failure behavior are limited. These studies are focussed only on the effect on TC/BC interface and microstructural pores [KPTvdZ19, Bia08a]. There are no numerical studies available in the literature that explicitly account for the presence of splat boundaries. However, the experimental observations by [MS12, HWLL18, LZC$^+$17] show that the failure behavior of the TBC is significantly influenced by the splats. For instance, in addition to the microstructural pores, the morphology of the splats and the adhesion between the splats is important for the cracking resistance of coatings. Besides the pore structure, the stacking morphology of the splats and adhesion between the splats are also important factors for the cracking resistance of coatings. It is, therefore, the objective of this research to carry out a systematic numerical study to investigate the effect of splat topology and its fracture strength on TBC fracture behavior in the presence of microstructural pores. Furthermore, concurrent multiscale modelling setup is adopted to include the free edge effect. The effect of splats is investigated using a parametric TBC model with realistic pore distribution corresponding to various splat features, namely, splat planarity, spacing, and also the strength. The scope of this research is relevant to the TBC community for TBC microstructure optimization by choosing the right set of processing and spraying parameters to get the desired splat characteristics.

## 3.2. Multiscale model of TBC microstructure

### 3.2.1. Overall geometry

The modelling of the TBC is carried out in a two-dimensional domain under plane strain assumptions. A two-scale concurrent multiscale modeling approach is adopted in which the explicitly resolved TC micro-structural features are embedded in a much larger domain of the TBC with an homogenized TC layer, as shown in Fig.3.1. TBC microstructural features such as pores, interface roughness and splats are modelled explicitly in the TC layer of the embedded computational cell as depicted in Fig.3.1.b. More details about the geometry and the modelling setup can be found in [KPTvdZ19].

TBC computational cell is enriched with random pore features that are representative of actual TBC microstructures [Slo]. The pores are modelled as an ellipsoidal quantity with an aspect ratio, orientation and size given in Table 3.1 for modelling convenience. The pores are distributed randomly within the TBC computational cell.

For simplicity, the interface planarity between TC and BC and also the horizontal splats are represented as a sinusoidal curve and it is given by (3.1).

$$Y_i = y_i + A_i \times cos(X \times 2\pi/\lambda) \quad [y_i = y_i + y_s; \quad A_i = A_i \times C] \tag{3.1}$$

where $A_i$ & $\lambda$ corresponds to the amplitude and wavelength of the sinusoidal curve, respectively. The subscript $i$ refers to the types of interfaces in the TC layer (i=0

Table 3.1: Experimental porosity measurements and the corresponding modelling parameters

| Geometrical features | Modelling parameters(%) |
|---|---|
| Volume fraction | 10 |
| Micro-porosity [SP] | 5 (Size = 25 $\mu$m$^2$) |
| Macro-porosity [LP] | 5 (Size = 75 $\mu$m$^2$) |
| Rounded shape porosity | 5 (AR = 1.5)[4 LP, 4 SP] |
| Lamellar shaped porosity | 5 (AR = 3) |
| Horizontally oriented lamellar porosity | 2.5 (0 deg) [1.75 LP, 1.75 SP] |
| Inclined lamellar porosity | 2.5 ($\pm$45 deg) [1.75 LP, 1.75 SP] |

corresponds to TC/BC interface and i>0 corresponds to the splat boundaries). $y_s$ and
$c$ denotes the spacing between the two adjacent interface and interface planarity, re-
spectively. The wavelength($\lambda$) and initial amplitude (A$_0$) of the interface are assumed
to be constant with a specified value of 60 $\mu$m and 10 $\mu$m, respectively [KPTvdZ18].
The vertical splats are modelled as straight lines, and they are distributed randomly
between the horizontal splats as shown in Fig. 3.1.c. The number of vertical splats
between any two successive horizontal interfaces is set to a value of 10 over the length
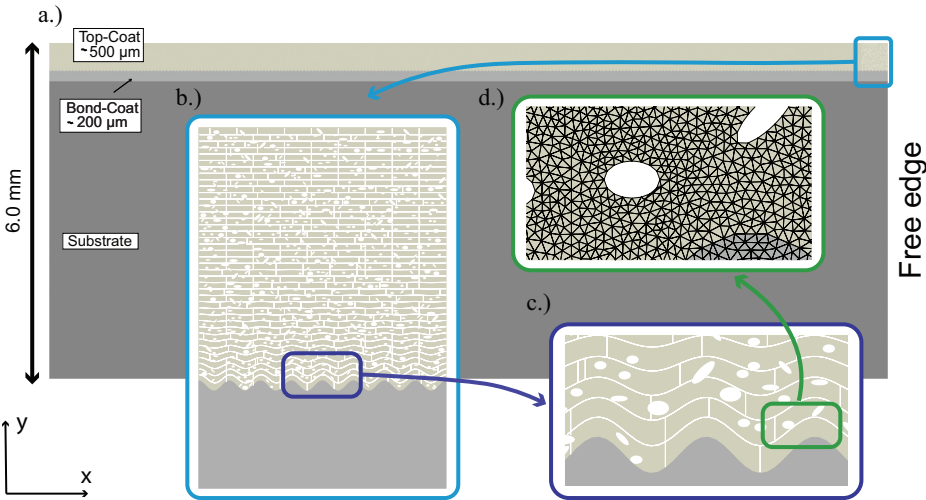of the explicitly modelled domain.



Figure 3.1: A schematic of TBC system with detailed microstructure

### 3.2.2. SIMULATION SET-UP

The microstructure is meshed with three noded plane strain triangular elements (CPE3) using GMSH to model the bulk response of the individual TBC layers. The fracture behavior of the TBC is modelled using a cohesive zone model which is implemented in the finite element framework using the zero thickness four noded cohesive element (COH2D4). It is also important to mention that the fracture process is modelled only in the computational cell and the outer regions of the TBC only can respond as a homogenized featureless elastic medium. Also, the elastic response of the splats themselves are not considered in the analysis since the splats are very thin compared to the thickness of the lamellae. In other words, the constitutive behavior of the splats is governed only by its fracture properties, defined through zero thickness cohesive element. The cohesive elements are inserted at every bulk element interface of the TBC computational cell using a MATLAB script. The insertion of cohesive element throughout the mesh enables the arbitrary crack initiation and propagation which is a prerequisite to predict the fracture behavior of such a complex system. However, the cracks are allowed to propagate only along inter element boundaries which lead to a mesh dependency effect. Hence, to obtain a converged fracture pattern a fine mesh size of 1 $\mu$m is used in the computational cell region. The outer elastic regions of the TBC is coarsely meshed with an average element size of 150 $\mu$m to reduce the computational time. The loading condition considered in this work corresponds to a single thermal cycle of as-deposited TBC system. A typical thermal cycle of a TBC consists of three phases namely the heating, dwell and cooling phase. In the heating and dwell phase of the thermal cycle, TBC is assumed to be stress free as these coatings are deposited at high temperature. Hence, only thermal contraction (cooling) phase of the thermal cycle is considered in the analysis, where the temperature is decreased from its typical operating value of 1100° to 30° C. The cooling rate does not play a role as the simulations are based on a quasi-static analysis. The non-linear fracture simulations are carried out in a commercial FEA package Abaqus using implicit Newton-Raphson solver.

### 3.2.3. ELASTIC AND FRACTURE PROPERTIES FOR CONSTITUENT PHASES

The bulk response of the different layers of TBC is assumed to be linearly elastic and isotropic. The fracture behavior of the TBC is modeled using a bi-linear cohesive law [HMP76] which is governed by fracture strength and fracture energy. Elastic, thermal and fracture parameters used for individual TBC layers are summarized in Table 3.2. Material properties of TC, BC and the substrate are chosen similar to the values given in [KPTvdZ18]. As indicated in Table 3.2, only the fracture property is considered to model the constitutive behavior of splats. The ratio of shear strength to normal strength ($\gamma$) for the TC layer and splats is assumed arbitrarily to have a value of 4 to suppress the shear failure of TBC given the fact that the experimental observations show that the TBC fails in tension (Mode I) rather than in shear (Mode II). The mode I fracture energies $G_{IC}$ reported in Table 3.2 is calculated from the fracture toughness

3. NUMERICAL INVESTIGATION INTO THE EFFECT OF SPLATS AND PORES ON THE
THERMAL FRACTURE OF AIR PLASMA SPRAYED THERMAL BARRIER COATINGS

32

values under plane strain and small plastic zone assumption. For convenience, the same value of $\gamma$ is also used to define the ratio between mode II and mode I fracture toughness. The microstructural defects in the outer (elastic) TC layer is accounted for

Table 3.2: Elastic and fracture parameters of the TBC components.

| Layers | $E$ (GPa) | $v$ | $\alpha$ ($10^{-6}$ 1/°C) | $\sigma_n$ (MPa) | $G_{IC}$ (N/mm) | $\gamma$ |
|---|---|---|---|---|---|---|
| Top coat | 200 | 0.15 | 12.5 | 200 | 0.01 | 4 |
| Bond coat | 130 | 0.3 | 14.5 | 500 | 0.3 | 1 |
| Splats | - | - | - | 75 | 0.002 | 4 |
| Substrate | 200 | 0.28 | 16 | - | - | - |

through the effective (reduced) elastic modulus of 80 GPa. The interface between TC and BC layer is assumed to have the same fracture properties as the BC layer.

## 3.3. RESULTS AND DISCUSSIONS

Parametric simulations are carried out to analyze the influence of the TBC microstructure such as splats and pores on TBC failure behavior. In addition, the effect of splat fracture properties is also considered in this study. The results are discussed in terms of crack initiation temperature and total length of all microcracks formed in the computational domain at the end of the cooling cycle for each parametric case. The crack initiation temperature is defined based on a predefined initiation length to avoid the mesh dependency effect. Predefined initiation length is defined as the minimum total length of consecutively failed cohesive elements required to form a measurable micro-crack. Based on the convergence analysis carried out in [KPTvdZ18, KPTvdZ19], a predefined length of 3 $\mu$m is used to define the crack initiation temperature for all the parametric simulations. The failure of the cohesive element is defined based on energy dissipation and the element is considered to have failed when it dissipates 95% of its total fracture energy. The TC layer is assumed to have completely failed if it becomes detached from the BC layer.

### 3.3.1. EFFECT OF TBC MICROSTRUCTURAL FEATURES

In this section, the effect of individual microstructural features on fracture behavior of the TBC is investigated. Three different TBC models with explicitly represented microstructures: (i) only pores, (ii) only splats and (iii) combined splats and pores are considered for this analysis along with the dense (defect free) TBC. The pores are distributed randomly in the TC layer with features given in Table 3.1 to model the pores in the TC layer. As discussed in Sec. 3.2.1, the horizontal splats are modelled using (3.1) with the splat planarity and spacing of 0.8 and 12.5 $\mu$m, respectively. To include the effect of randomness of the pore distribution and vertical splats in the analysis, five different realizations are considered. To illustrate the effect of

splats in the TBC failure process, stress distributions ($\sigma_{yy}$) along with the crack pattern at the end of the thermal loading step for two different microstructural configurations (namely TC layer with pores and combined splats & pores) are shown in Fig. 3.2. The overall stress distribution ($\sigma_{yy}$) is in correspondence with the studies carried out in the literature [VKS01, Bia08b]. As observed in Fig. 3.2, the peaks and valleys of the TC/BC interface lead to tensile and compressive states of stress ($\sigma_{yy}$), respectively. The CTE mismatch between the layers and the presence of pores result in a complex stress field especially at the vicinity of pores as shown in Fig. 3.2. Also, for both configurations, the cracks tend to nucleate and propagate from the edge due to tensile stress ($\sigma_{yy}$) generated out of the free edge accompanied by local stress concentration near the pores. However, as shown in Fig. 3.2.a and b, the presence of splats has a significant effect on the TBC cracking behaviour both in terms of crack nucleation and propagation. For the TBC with combined splats and pores, the cracks propagate mostly along the splat boundaries. In case of TBC with only pores, the crack propagation is governed by the direction of local stress concentration generated by the pores. It is also important to note that the stress distribution in TC sufficiently far away from the cracked regions remains identical for both configurations since the elastic response of splats is not considered for the analysis.
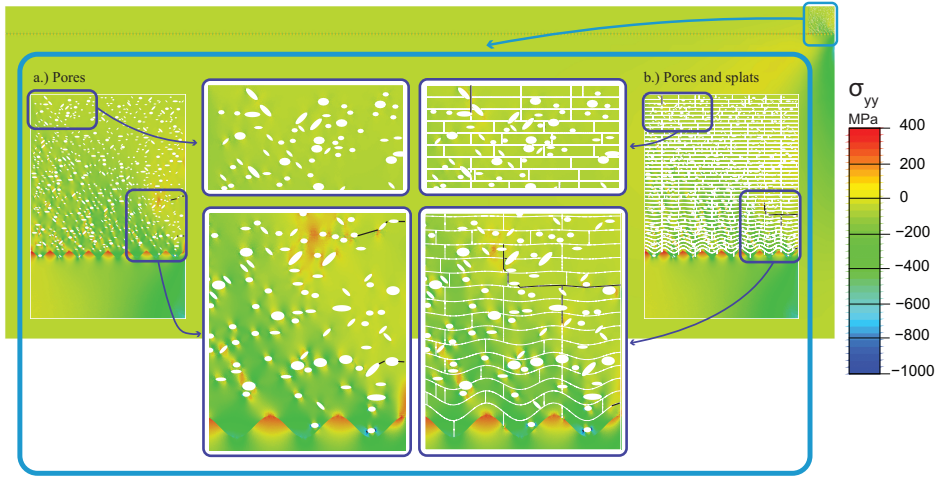


Figure 3.2: Stress distribution ($\sigma_{yy}$) and failure behavior of TBC at T = 30°C for two distinct microstructural configurations (a) Splats and (b) Combined splats and pores

The results are presented in terms of crack initiation temperature and total crack length in Table 3.3 for the four distinct TBC microstructural configurations as discussed.

It can be observed from Table 3.3 that the variations in TBC microstructural configuration have a significant influence on its failure behavior. For the microstructural

Table 3.3: Effect of TBC microstructural features.

| Microstructural features | Crack initiation temperature (°C) | Total crack length (mm) |
|---|---|---|
| Dense (No Defects) | 330 | 0.16 |
| Pores | 310±50 | 0.07±0.01 |
| Splats | 800±5 | 0.28±0.03 |
| Splats & Pores | 680±16 | 0.22±0.05 |

configurations without splats, the presence of pores did not have a substantial effect on crack initiation temperature whereas a positive influence of pores is observed for the configurations with splats. In terms of the total crack length, the presence of pores has a positive effect for both the configurations (with and without splats). However, this effect is more pronounced for the microstructure without splats. For instance, the total crack length of the dense TBC is approximately two times higher than the TBC with pores. This is due to the fact that the presence of pores increases the TBC compliance which reduces the strain energy contribution to the crack driving force[KVS11]. The positive influence of the pores on TBC lifetime is reported in the literature through experimental measurements[AVSL04, CMÖ+13]. On the other hand, a TBC with splats leads to early crack initiation and also larger crack length, which is expected because of weak interface. From Table 3.3, it can be concluded that the presence of pores result in an improved TBC fracture behavior whereas the presence of splats is detrimental to the TBC. To understand the effect of splats on TBC failure behavior, parametric simulations are carried out in the next section for different geometries and fracture properties of the splats.

### 3.3.2. PARAMETRIC SIMULATION
The parametric studies are carried out for three different parameters such as splat planarity, spacing and porosity and the variations are listed in Table 3.4. The simulation results are discussed in terms of crack initiation temperature and total crack length. Similar to Sec. 3.3.1, five different realizations are utilized for each parametric case to obtain the statistical variation due to the random distribution of pores and vertical splats.

Table 3.4: Summary of splat and pore geometrical parameter used.

| Micorstructural features | Geometrical Parameters |
|---|---|
| Splat planarity | 0, 0.4, 0.8, 1 |
| Splat spacing | 6.25, 12.5, 25 ($\mu$m) |
| Porosity($V_f$) | 0, 10, 15, 20 (%) |

EFFECT OF SPLAT PLANARITY

To investigate the effect of splat planarity, four different planarity values 0, 0.4, 0.8 and 1 are analyzed. The splat spacing and porosity are fixed with a value of 12.5 $\mu$m and 10 %, respectively. The planarity value of 0 results in flat interfaces in the computational domain whereas the planarity of 1 corresponds to the cosine curve with specified amplitude of 10 $\mu$m for all the splat boundaries (refer (3.1)). For other planarity values, the amplitude of the splats (cosine curve) are scaled linearly with the increase in number of interfaces/splat boundaries. The results of the simulations are summarized in Fig. 3.3 to show the influence of splat planarity on initiation temperature and total crack length. From Fig. 3.3.a, it can be observed that the crack initiation temperature shows a weak dependence on splat planarity. This is due to the fact that the crack initiation is governed mostly by the free edge stress which is maximum at a region away from the TC/BC interface. In this region, the change in splat amplitude for planarity values less than 1 is minimal because, with increase in number of interface/splat boundaries there is a decrease in amplitude. For a planarity value of 1, the amplitude of the splats boundaries remains unaffected which results in a trend towards delay in crack initiation as shown in Fig. 3.3.a. In terms of total crack length, the splat planarity shows a significant influence especially for the planarity of 0 and 1 as shown in Fig. 3.3.b. The crack length for the TBC with flat splat boundaries (planarity =0) is sensitive to the distribution of pores. Two out of five realization shows complete failure of the TC with major cracking close to the TC/BC interface. Hence, the statistical variation of total crack length for zero planarity is represented as inconclusive in Fig. 3.3.b. This behavior is due to the presence of flat interface which favors the linking and propagation of microcracks. In addition, the formation of microcracks is influenced by the distribution of different pore features. Complete failure of the TC occurs if these microcracks reaches a critical length. For the splat interfaces with planarity of 0.4 and 0.8, the total crack length remains almost same and it decreases by a factor of 2 for the planarity of 1. Thus, in general, it can be concluded that an increase in splat planarity improves the thermal fracture behavior of TBC. Indentation tests on APS TBC samples [HWLL18] show that the fracture resistance is improved significantly for TBCs with rough splat interfaces. Similarly, thermal cycling studies [Now14, ESB+13] on TBC also conclude that the bond coat roughness has a significant effect on TBC lifetime with higher roughness leading to an increase in TBC lifetime.

EFFECT OF SPLAT SPACING

Another parameter of interest is the splat spacing which is a direct measure of the TC lamellae thickness. In the current TBC modelling set up, splat spacing affects both the interface planarity and the number of weak interfaces within the TC layer (refer (3.1)). Hence, the variations in splat spacing may have a significant effect on the TBC fracture characteristics. In order to study this effect, four different splat spacing given by 6.25, 12.5, 25 and 50 $\mu$m are considered. The values for splat planarity and volume fractions are kept constant at 0.8 and 10 %, respectively. The results obtained
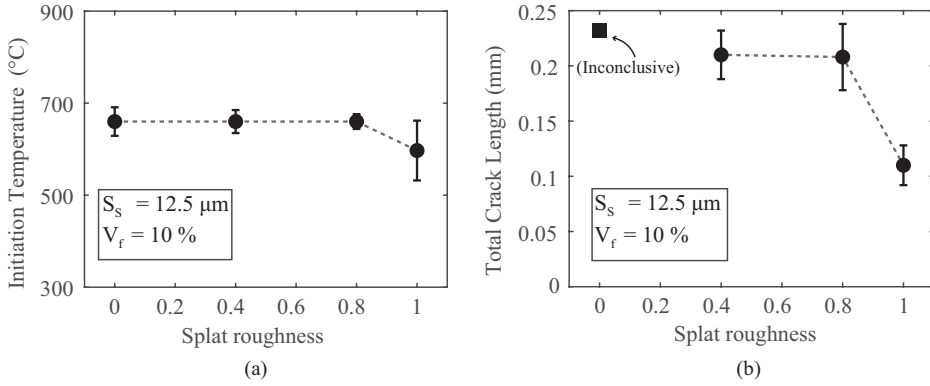
Figure 3.3: Variation of (a) crack initiation temperature and (b) total crack length for different splat planarity of 0 (flat), 0.4, 0.8 and 1 with the fixed splat spacing of 12.5 $\mu$m and volume fraction of 10%.

from the analysis are summarized in terms of crack initiation temperature and total crack length and are shown in Fig. 3.4. As observed in Fig. 3.4.a, the crack initiation temperature remains almost constant for the range of splat spacings considered. Nevertheless, for the reference configuration with only pores (no splats) given in Table 3.3 crack initiation temperature is significantly lower than the initiation values reported in Fig. 3.4.a. In terms of total crack length, the results indicate that the total crack length decreases non-linearly with the increase in splat spacing as shown in Fig. 3.4.b. For a spacing of 6 $\mu$m the final crack length is highly sensitive to the distribution of pores with three realizations predicting complete TC failure. This inconclusive behavior is governed by the stress distribution close to TC/BC interface and the local stress concentration generated by the pores. The decrease in total crack length with the splat spacing is attributed to the reduced number of weak interfaces and the increase in splat planarity.

EFFECT OF PORE VOLUME FRACTION

In this section, the volume fraction of the pores is varied with a constant splat planarity of 0.8 and a spacing value of 12.5 $\mu$m. Four different pore volume fractions given by $V_f$ = 0, 10, 15 and 20 % are considered. To illustrate the effect of splats on the failure behavior of TBC along with porosity two distinct microstructure configurations are considered: one with pores and one with combined splats and pores. The crack initiation temperature and total crack length for both configurations are reported in Fig. 3.5.

For all porosity values considered the presence of splats significantly influences the failure characteristics of TBC as observed in Fig. 3.5. Presence of splats leads to early crack initiation when compared to the TC layer with pores as shown in Fig. 3.5.a. The crack initiation temperature remains approximately constant for the TC layer with pores whereas the crack initiation temperature decreases non-linearly
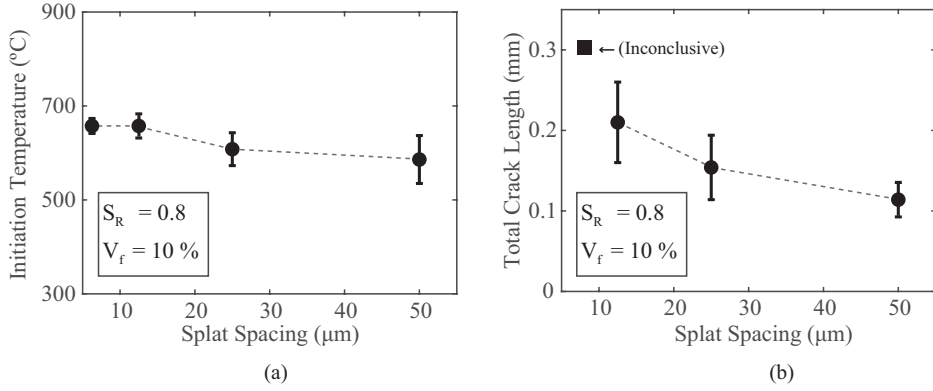
Figure 3.4: Variation of (a) crack initiation temperature and (b) total crack length for different splat spacing of 6.25, 12.5, 25 and 50 $\mu$m with the fixed splat planarity of 0 and volume fraction of 10%.
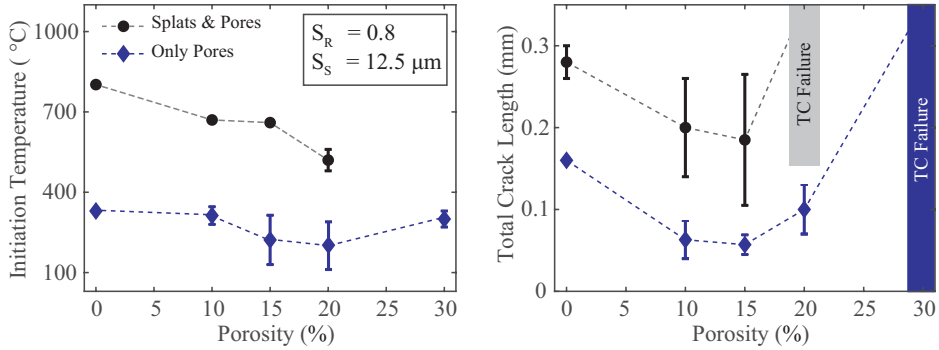


Figure 3.5: Variation of (a) crack initiation temperature and (b) total crack length for different volume fraction of 0(dense), 10, 15, 20, 30%. with the fixed splat planarity of 0 and splat spacing of 12.5 $\mu$m.

with increase in porosity for the microstructure with combined splats and pores. For the TC layer with combined splats and pores, the crack initiation temperature of 10% porosity decreases from 800 to 700 °C when compared with zero porosity case. Upon further increase in porosity, the crack initiation temperature remains almost constant up to $V_f$ = 15% after which it decreases for $V_f$ = 20 %. In terms of total crack length, it can be seen that for both the cases the trend remains almost the same. The presence of pores improves the fracture resistance of the TC compared to the dense TBC (refer Fig.3.5.b). This is due to the decrease in strain energy contribution to the crack driving force with porosity as explained in Sec.3.3.1. The scatter in total crack length values between individual simulations for a nominally identical sets of input parameters especially for the configuration with combined splats and pores is attributed to the complex interaction of different pore features and also its interaction with the splat

boundaries. Also, it is important to note that complete failure of TBC occurs for a critical value of the porosity is $V_f$ = 30% for TC with pores and $V_f$ = 20% for TC with combined splat and pores. The optimal porosity value remains constant at $V_f$ = 15% for both microstructural configurations.

### 3.3.3. EFFECT OF FRACTURE PROPERTIES

As discussed in Sec. 3.2.2, the constitutive behavior of the splats are governed by its fracture parameters. Hence, the variation of these parameters significantly influences the fracture behavior of the TBC system. To study this effect, the fracture ratio defined in (3.2) is varied with fixed splat planarity of 0.8, splat spacing of 12.5 $\mu$m and porosity of 10 %. Two distinct normal ($f_n$) and shear fracture ($f_s$) ratios are considered to analyze the influence of normal and shear fracture properties of the splats. For each fracture ratio, the simulations were carried out for five different values given by 0.5, 0.75, 1, 1.5 and 2. While studying the influence of one fracture ratio the other fracture ratio is fixed at the value of 1. In otherwords, to study the effect of splat normal fracture properties, the normal fracture ratio ($f_n$) is varied with values given by 0.5, 0.75, 1, 1.5 and 2 for a fixed shear ratio ($f_s$) of 1 and vice-versa.

$$
\begin{aligned}
\sigma^{TC} &= f\sigma_0^{TC}, \\
G^{TC} &= fG_0^{TC}
\end{aligned}
\tag{3.2}
$$

where $f$ is the fracture ratio and $\sigma_0^{TC}$ and $G_0^{TC}$ are the fracture properties of the benchmark material. Note that both properties are varied using the same fracture ratio ($f$).

Crack initiation temperature and total crack length for both normal and shear fracture ratios are shown in Fig. 3.6. From the Fig. 3.6.a, it can be observed that both the crack initiation temperature decreases almost linearly with increase in normal fracture ratio. For the variations in shear fracture ratio ($f_s$), the crack initiation temperature remains unaffected as shown in Fig. 3.6.c. This is because the normal fracture properties, being always less than the shear fracture properties for the splat boundaries, dominates the crack initiation behavior. In terms of crack length, the results indicate that variation of total crack length with the normal fracture ratio is not monotonic as shown in Fig. 3.6.b. In particular, a drastic increase in damage is observed in the TC layer when the normal fracture ratio is decreased to a value of 1 (i.e. total crack length increases abruptly by a factor of 2.5 when compared to the fracture ratio ($f_n$) of 1.5). Similarly, the results shown in Fig. 3.6.d are sensitive particularly, when the shear fracture ratio is decreased below a certain critical value. For instance, the complete failure of the TBC occurs when the shear fracture ratio is decreased below the value of 1. The critical value for the complete TBC failure is decided by the value of the fracture parameters for which the coalescence is favoured.
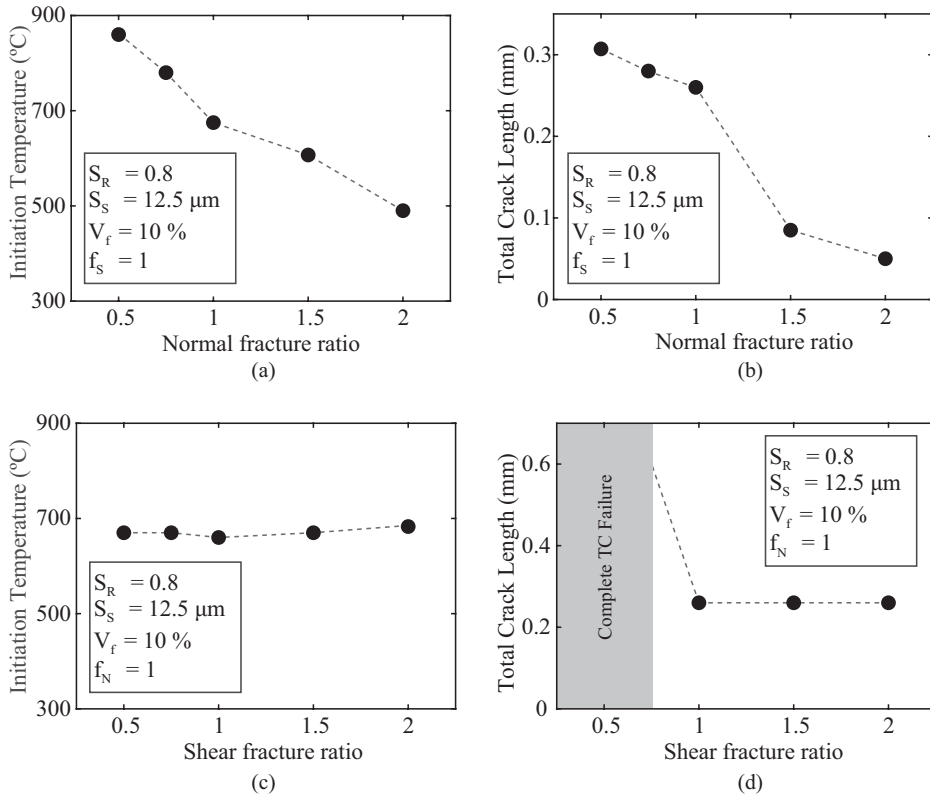
Figure 3.6: Variation of (a)&(c) crack initiation temperature and (b)&(d) total crack length of TBC with random representation of pores for different splat normal and shear strength values.

## 3.4. CONCLUSIONS

Thermal fracture behavior of the APS TBC with explicitly modelled splat boundaries and pores is analyzed using cohesive elements based finite element method. The influence of splat geometric characteristics (such as the roughness of the planes in which the splats are located and their spacing), porosity and splat material parameter (fracture properties) on TBC fracture behavior are studied through parametric simulations. The results of the parametric studies are reported in terms of the crack initiation temperature and total micro crack length in the computational domain upon cooling down from the peak temperature of 1100 ° C to room temperature (30° C), whereby both the splat boundaries and pores are found to exhibit a significant influence on the fracture behavior. The following conclusions are drawn from the parametric finite element investigations.

1. Microstructural features of the TBCs play a significant role in determining

its failure characteristics. With reference to the fully dense TBC system, the presence of pores improves the fracture resistance whereas the presence of splat boundaries leads to early and more extensive failure of the TBC.

2. The influence of splat planarity on crack initiation temperature is limited. The crack length for the flat splat boundaries is sensitive to the distribution of pores. In general, the increase in splat planarity improves the TBC fracture resistance.

3. Splat spacing did not have a significant influence on the initiation temperature whereas the total crack length decreases with an increase in splat spacing.

4. The presence of pores improves the fracture behavior for both microstructural configurations considered. However, porosity beyond a critical value leads to early failure. The optimal porosity is estimated as 15 %.

5. On the effect of splat fracture properties, the crack initiation temperature scales more or less linearly with normal tensile strength of the splats. In terms of crack length, the results are sensitive when the fracture ratio are reduced to a value below a critical level. Complete failure of TBC occurs when shear fracture ratio is decreased below a value of 1.

The results and insights aim to clarify understanding the effect of TBC microstructure especially splats and pores on failure behaviour, which in turn can aid in optimizing the processing and spraying parameters for improved performance/lifetime. Based on the current simulations, TBC systems containing up to 15% pores, having the splats arranged in non-planar configuration, having a large splat spacing and a high splat tensile strength perpendicular to the splat plane, should give the best thermal cracking resistance.

# 4

# MODELLING THE FRACTURE BEHAVIOR OF THERMAL BARRIER COATINGS CONTAINING HEALING PARTICLES

The performance of a self-healing Thermal Barrier Coating (TBC) containing dispersed healing particles depends crucially on the mismatch in thermomechanical properties between the healing particles and the TBC matrix. The present work systematically investigates this phenomenon based on numerical simulations using cohesive element-based finite element analysis. The effect of the mismatch in Coefficient of Thermal Expansion (CTE) and fracture strength between the healing particles and the matrix on the fracture characteristics is quantified in detail. Unit cell-based analyses are conducted on a representative self-healing TBC system under a thermal loading step typically experienced by TBC systems in jet turbines. Two different simulation setups are considered within the TBC unit cell namely (i) a single pair of healing particles and (ii) a randomly distributed array of healing particles. The results of the simulations are reported in terms of the fracture pattern, crack initiation temperature and crack length for various CTE mismatch ratios. Correlations are established between the results obtained from the two simulation setups essentially revealing the effect of spatial distribution and proximity of healing particles on the fracture pattern. The results obtained from the analyses can be utilised to achieve a robust design of a self-healing TBC system.

## 4.1. INTRODUCTION

Several efforts have been made to increase the lifetime of the TBC system, mainly in the directions of varying the deposition process and coating compositions in order to delay the initiation of micro-cracks [VSS09, Dar13, KK16]. Incorporating self-healing mechanisms in TBC systems is a novel approach to improve the lifetime of these coatings [STD⁺15, DCS⁺15, NEC⁺18, OFZ⁺16, OWY⁺16]. The principle of the self-healing mechanism in a TBC system is demonstrated in [DCS⁺15]. The self-healing TBC is based on alumina coated Mo-Si particles embedded in the TC layer close to the TC/BC coat interface where the micro-cracks are likely to initiate. Upon cracking in the TBC, the micro-cracks interact with the healing particles, resulting in fracture of the particles. Subsequently, the healing agent within the particles oxidises and diffuses into the crack to form a glassy phase which in turn reacts with the surrounding matrix to form a load-bearing crystalline ceramic (zircon). The resulting healing of the micro-cracks delays the formation of a macro-crack by preventing crack coalescence which, in turn, extends the life time of the TBC system. Further details of the above-discussed self-healing TBC system such as detailed description of the healing mechanism, type of healing particle, fabrication routes and associated challenges can be found in the following works [vdZB15, STD⁺15, NEC⁺18, NME16, CMB⁺18].

Numerous computational studies have been conducted to investigate the failure mechanisms in the TBC system. In the context of fracture analysis in TBC systems, different approaches have been used, including, classical fracture mechanics-based methods (e.g. VCCT, energy release rate) [BBB⁺10, FJL⁺14], cohesive zone element based methods [BMHM05, ZYG⁺15] and the extended finite element method (XFEM) [HTS11, YWD⁺13]. Classical fracture mechanics approaches are suitable for crack propagation studies, whereas cohesive element-based approach enables modelling of crack initiation as well as crack propagation. XFEM is an enriched version of the classical finite element method which embeds discontinuities in the shape functions of a classical 2-D or 3-D finite element. This method serves as a tool to represent initial and evolving crack geometry independent of the finite element mesh and the crack evolution can be modelled either using classical fracture mechanics parameters or cohesive traction-separation laws. One of the current shortcomings of XFEM is its limited capability in dealing with multiple cracking and coalescence, which are crucial in the current study. Cohesive elements were utilised successfully for such multiple cracking and coalescence problems albeit with higher computational costs to achieve 'mesh-independent' solutions. A detailed review on various modelling methodologies and failure mechanisms in TBC systems addressed through computational modelling can be found in [WLY⁺16]. A second review on the influence of modelling choices in terms of interface morphology, boundary conditions, dimensionality and material models on the TBC response is presented in [BS17]. They provided guidelines and strategies for effectively modelling the stress evolution and the crack propagation in TBC systems. All the investigations in the

literature have contributed to a detailed understanding of the failure mechanisms in TBC systems.

From the perspective of modelling the behavior of a self-healing TBC system, additional aspects need to be accounted for in the analysis as compared to the conventional TBC systems. Specifically, the effect of the presence of healing particles on the TBC fracture behaviour has to be analysed from two different perspectives. Firstly, to successfully trigger healing mechanism, the microcracks initiated in the TBC have to interact with healing particles leading to the opening of the particles for healing activation. This, in turn, depends on the geometric and the material properties of the healing particles in relation to the TBC layers. Secondly, it is essential to study how the healing particles influence the thermomechanical behaviour of the self-healing TBC in comparison with the baseline TBC without healing particles, in other words, introducing healing particles should not significantly deteriorate the mechanical integrity of the original TBC system. Several modelling studies have been conducted in the literature to address the above two aspects [GGvP17, GvTT+17, QZR15, LJYY16, OON16, GGvP15]. For instance, the influence of mechanical properties of the healing particles on the fracture mechanism in a self-healing material have been analysed in detail in [PTvdZ15, GGvP15]. In [GGvP17], crack propagation studies were conducted in an idealized healing capsule(s)-matrix system and the effects of geometric and material parameters were analysed using cohesive and extended finite element method (XFEM). Within the context of self-healing TBC systems, few modelling studies have addressed the effect of the healing particles on the TBC properties and the thermomechanical response [KMZC+16, WSZ+18]. The effect of the healing particles on the fracture mechanisms and the mechanical properties of a particulate composite representing a self-healing TBC microstructure were studied using cohesive element-based finite element analysis in [PTvdZ15, PKTvdZ19, PKTvdZ17]. However, one critical aspect that has not been analysed in detail pertains to the mismatch in thermo-elastic properties coupled to a mismatch in fracture properties.

In order to design a self-healing TBC system with dispersed healing particles, an important issue that needs detailed understanding is the effect of mismatch in CTE between the particles and the TBC layers, in addition to the elastic and fracture property mismatch. An ideal self-healing TBC should have healing particles with similar CTE in relation to the surrounding TC layer. Such a combination would prevent generation of additional thermal stresses in the TBC which would otherwise lead to microcrack formation. On a different context, specific prerequisites on the mechanical properties of the healing particles and the particle/matrix interface are necessary for a successful activation of the healing mechanism [PTvdZ15]. With this motivation, a detailed finite element analysis is conducted to quantify the effect of mismatch in thermomechanical properties on the fracture evolution in the self-healing TBC system. The effect of CTE mismatch is investigated in detail using two simulation setups, one with a TBC containing two healing particles and the other

with a TBC consisting of a randomly distributed array of particles. Further, the effects of the relative strength of the particle and the interface with respect to the TC layer are analysed using the finite element simulations on the multiple particles setup. The present work is connected to the optimal design of self healing TBCs from two distinct aspects: (1) It serves as an analysis tool to decide the best combination of thermomechanical properties of the healing particles and the matrix to achieve a robust self-healing system and (2) It allows to choose the best spatial arrangement of healing particles to control the crack and healing patterns.

## 4.2. FINITE ELEMENT MODEL OF TBC

### 4.2.1. MODEL GEOMETRY

A 2D multiscale approach is adopted for the finite element analysis of fracture evolution in a self-healing TBC system. The system considered is composed of two different layers of the TBC system, namely the TC and the BC. The TBC unit cell is periodic in the horizontal direction, while in the vertical direction, the layers are modelled with their respective thicknesses. The interface between the TC and the TGO layers is modelled as an idealised sinusoidal curve [VGS09], whose wavelength and amplitude are assigned values of 60 $\mu$m and 10 $\mu$m respectively. These values are representative of a typical interface morphology in the air plasma sprayed TBC systems [ESB$^+$13]. The thickness of the TC and the BC layers are taken as $h_{TC}$ = 500 $\mu$m and $h_{BC}$ = 200 $\mu$m respectively. The TGO layer is usually a thin layer whose thickness increases during operation (as a function of thermal cycles/time). The evolution of the TGO thickness is not modelled since only a single thermal cycle is analysed during which the growth of the TGO is negligible. Since the objective is to investigate the role of the healing particles and the property mismatch on the cracking pattern the TGO layer is not considered in the present analysis. Correspondingly, the loading condition considered in this work represents a typical (single) thermal cycle of an as-deposited TBC system.

As discussed earlier, the healing particles made of MoSi$_2$ are dispersed in the TC layer closer to the TGO layer representing the self-healing TBC architecture reported in [STD$^+$15]. Dispersing healing particles close to the TGO layer would be an effective approach as the microcracks are expected in such regions [NEC$^+$18]. Fig. 4.1 shows one of the configurations considered in the study in which a pair of healing particles is dispersed in the TC layer, whose location is characterised by the interparticle distance ($D_p$) and the orientation ($\theta$). The modelling approach is then extended to a system containing randomly distributed healing particles, whose details will be discussed in corresponding sections. The unit cell is meshed with two-dimensional three-noded plane strain triangular elements using the open source software GMSH [GR09]. To model fracture, cohesive elements are embedded throughout the finite element mesh regions in the unit cell using a Matlab script. Finite element analysis is carried out using the commercial software Abaqus. The
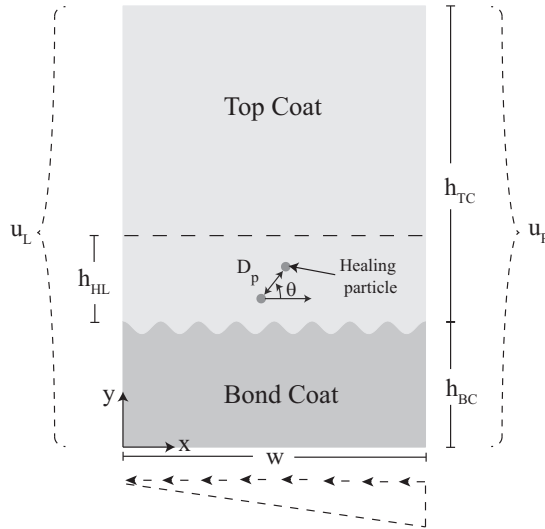
Figure 4.1: Finite Element Geometry showing two healing particles.

insertion of cohesive elements throughout the finite element mesh enables arbitrary crack initiation and propagation, an important requirement in a complex system such as a TBC containing healing particles. One important consideration while using cohesive elements everywhere is the mesh dependency effect. A random and sufficiently fine mesh is a prerequisite in order to obtain a converged fracture pattern [PTvdZ15]. The element size is also chosen carefully to fulfill the requirements of properly resolving the cohesive zone. The region where the cracks are likely to nucleate and grow is finely meshed with an element size of 1 $\mu$m. The remaining regions of the TBC unit cell are meshed with an element size of 2 $\mu$m. The domain convergence analysis is carried out to find an appropriate width (W) of the periodic unit cell based on the convergence of critical temperature (onset of unstable crack growth). For W = 480 $\mu$m and W = 960 $\mu$m the percentage error in critical temperature is around 5 %. Hence, W of 480 $\mu$m is chosen for modelling the periodic unit cell. The finite element model is two-dimensional which poses limitations on the scope as actual three-dimensionality of the TBC microstructure is lost. However, a two-dimensional approach can be used effectively to unveil the failure mechanisms in TBC as it captures the most of the important features of the microstructure. Further, considering the size of the unit cell and the level of microstructural details of the considered self-healing TBC system, a three-dimensional analysis is not feasible to investigate in detail the effect of geometric and material parameters on fracture evolution.

### 4.2.2. LOADING AND BOUNDARY CONDITIONS

The substrate of the TBC, whose dimension is orders of magnitude larger than the individual layers of the TBC, is not modelled explicitly. Rather, its effect is accounted for through enforcement of boundary conditions derived using the thermal deformations induced by the substrate during a thermal cycle [HST09]. Due to its dimensions, the thermal deformation of the substrate can be assumed to be unaffected by the TBC layer. With this assumption, the induced thermal deformations can be obtained, and these displacements are then enforced as periodic conditions in the TBC unit cell as given in Eq.((4.1)) for the left (L) and right (R) edges of the unit cell,i.e.,

$$
\begin{aligned}
u_x^R - u_x^L &= (1 + \nu_s)\alpha_s\Delta TW, \\
u_y^R - u_y^L &= 0,
\end{aligned}
\tag{4.1}
$$

where $\nu_s$ and $\alpha_s$ correspond to Poisson's ratio and the coefficient of thermal expansion, respectively and the subscript $s$ refers to the substrate. The bottom (B) edge of the unit cell is subjected to the following displacement field:

$$
\begin{aligned}
u_x^B &= (1 + \nu_s)\alpha_s\Delta Tx, \\
u_y^B &= 0,
\end{aligned}
\tag{4.2}
$$

whereas the top surface of the TBC is modelled as traction-free.

A typical thermal cycle that a TBC undergoes during operation consists of an ascending branch where the temperature rises more or less linearly from room temperature to operating high temperature, followed by a constant temperature operating period and finally cooling down phase back to the room temperature. In the literature, it is assumed that the TBC is stress-free at operating temperature ($1100^o$C) as the coating is deposited at around similar temperature range [HST09, HE02]. The third phase of the cycle corresponds to a cooling phase in which thermal mismatch stresses develop and cracks are expected to initiate. Hence, this cooling down phase of the cycle is considered as the loading case whereby the temperature in the TBC model is gradually decreased from $1100^o$C to $30^o$C. As the crack formation is based on an quasi-static analysis, the cooling rate does not play a role and the system is assumed to be in thermal equilibrium at all times.

### 4.2.3. CONSTITUTIVE PROPERTIES

The behaviour of the TBC system is strongly governed by the mismatch in the thermomechanical properties of the individual layers of the TBC system. The constitutive material behaviour of the different layers is assumed to be linear elastic and isotropic. A bilinear traction-separation law is used as the constitutive relation for the cohesive elements with different cohesive properties assigned for each layer and the interface in the TBC system. With cohesive elements embedded everywhere, another important aspect to be addressed is the way the periodic boundary conditions are applied on the edges where at a given nodal location, there is usually more than one

Table 4.1: Constitutive properties of the TBCs.

| Layers | $E$ (GPa) | $v$ | $\alpha$ ($10^{-6}$ 1/°C) | $\sigma^n$ (MPa) | $G^{IC}$ (N/mm) | $\gamma$ |
|---|---|---|---|---|---|---|
| Top coat | 80 | 0.15 | 12.5 | 100 | 0.002 | 4 |
| Bond coat | 130 | 0.3 | 14.5 | 500 | 0.3 | 1 |
| Healing particle | 250 | 0.22 | varied | varied | 0.02 | varied |
| Substrate | 200 | 0.28 | 16 | - | - | - |

node. Appropriate pairs of nodes are identified on the left and the right edges, which upon the enforcement of the boundary conditions does not prevent any crack to pass through and open the edges when required by the process, i.e., the artificial arrest of cracking in the edges is prevented.

The Youngs modulus $E$, Poisson's ratio $v$ and coefficient of thermal expansion $\alpha$ for the distinct phases are summarised in Table 4.1. The elastic and thermal properties of the TC are chosen similar to the values reported in [RE00, KBK17]. The elastic properties and the thermal expansion coefficient of the BC are chosen close to the values given in [LW03]. The stiffness of the healing particles is assumed to be 3 times larger than the stiffness of the TC [PTvdZ15]. The mode I (normal) fracture strength $\sigma^n$ and the mode I fracture energy $G^{IC}$ of the TC, the BC and the healing particles are considered in accordance with [TSBA00, HST09, YL97], where the values of the fracture energies reported in Table 4.1 have been calculated from the fracture toughness $K^{IC}$ under plane strain and small plastic zone assumptions, i.e.,

$$G^{IC} = \frac{(K^{IC})^2(1-v)}{E}. \tag{4.3}$$

The ratio of the shear strength to the normal strength for the TC is taken as $\gamma_{TC} = 4$. This value is in-line with the experimental observations that the ceramic TBC fails in tension (Mode I) rather than in shear (Mode II). For simplicity, the same value of $\gamma_{TC}$ is also used for the ratio between the mode I and mode II fracture toughness. For the BC, which is a metallic layer, the ratio is taken as $\gamma_{BC} = 1$. As indicated in Table Table 4.1 distinct values for the properties of the healing particles are considered. The BC/TC interface is chosen to have the fracture properties of the BC. Unless explicitly specified, the normal fracture strength, $(\sigma^n_P, \sigma^n_{i_{P/TC}})$ and the mixed-mode strength ratio, $(\gamma_P, \gamma_{i_{P/TC}})$ of the healing particles and the healing particle/TC interface are assumed to be equal and are taken as 300 MPa and 4, respectively. The influence of the fracture properties of the particles and the interface are analysed separately in Sec. 4.3.3 and Sec. 4.3.4 by considering different values for the strength of the particle and the interface.

## 4.3. Results and discussions

Three thermo-mechanical material parameters are considered for the analyses, namely (a) the CTE mismatch between the healing particles and the TC matrix, (b) the relative strength of the healing particle with respect to the TC layer and (c) the strength of the interface between the TC matrix and the particle. Finite element analyses on the TBC unit cell with boundary and loading conditions as described in Sec. 4.2.2 are conducted for a range of the above three material parameters, and the results are summarised in terms of the fracture pattern and the crack evolution kinetics in the TBC layers in the following sections.

In the context of cohesive element approach, crack initiation occurs when the traction in the element exceeds the material strength, and the crack is said to be fully formed when the amount of energy per unit area dissipated in the element is equal to the fracture energy of the material phase. In a system containing different phases with significantly different fracture energy values between the phases, it is not straightforward to define a failed state of the element in the different material phases. For instance, in the present situation, the fracture energy of the TC layer is 10 times lower than that of the healing particles. This would mean that the complete failure of a particle cohesive element is reached only when the energy dissipated in the crack opening is 10 times as compared to that of the complete failure of the TC cohesive element. Nonetheless, in both cases, the cohesive crack initiation would have started already. Thus, in order to have a useful interpretation of a failed state in the cohesive element, it is assumed that the cohesive element in the TC is completely failed when the energy dissipated within the element (per unit area) is equal to 95% of the fracture energy of the TC. For the cohesive elements in the healing particles, an element is assumed to be failed (or the crack is said to be formed) when the dissipated energy in the element is equal to 10% of the fracture energy of the healing particles.

The results of the simulations are reported in terms of crack initiation temperature. In order to have a mesh-independent definition of crack initiation, a study was performed whereby the crack is said to be formed or initiated in terms of a predefined crack length (sum of the length of the failed cohesive elements). Three different crack lengths are considered for this purpose given by 1, 2 and 3 $\mu$m. It was observed that the choice of the above crack lengths did not have a significant influence on the crack initiation temperature (error being less than 5%). To this end, the crack initiation temperature is assumed to be reached when the cumulative crack length reaches a value of 3 $\mu$m.

### 4.3.1. Effect of CTE mismatch

For the CTE mismatch study, two different simulation setups are considered, denoted as a two-particle system and a multiple particles system. The simulation set up for the two-particle system is shown in Fig. 4.1. The objective is to first study the effect of the CTE mismatch on the local crack evolution in the presence of two idealised healing particles whose topology/distribution is fully defined by the inter-particle distance

and the orientation. Subsequently, the second setup containing a more realistic random distribution of multiple particles are modelled in the TC layer, and the crack evolution is investigated. Finally, the results obtained from the two simulation setups are compared in order to provide an explanation of failure in the multiple-systems setup based on the two-particle set up.

TWO-PARTICLE SIMULATION SETUP

Two healing particles each of radius $R_P$=7.5 $\mu$m are dispersed in the TC layer. The interparticle distance and the orientation between the particles are varied to study the effect of these topological/spatial parameters on the crack pattern. Five different values are assigned for the interparticle distance given by $D_P/R_P$ = 0.25, 0.5, 1, 1.5 and 2, where $D_P/R_P$ is the ratio of the normal distance between the edges of the particles to the radius of the particle. The orientation characterised by the angle $\theta$ between the line connecting the centre of the particles and the positive $x$-axis is assigned four values given by $\theta = 0^0, 30^0, 60^0$ and $90^0$.

Two different CTE mismatch ratios, given by $\alpha_P/\alpha_{TC}$ = 1.5 and 0.5 are considered for the simulations. The stress fields in and around two adjacent particles are shown in Fig. 4.2 at $T = 30^0$C for $D_P/R_P$ = 0.5 and $\theta = 30^0$. As shown in Fig. 4.2a, the crack initiates between the particles when $\alpha_P/\alpha_{TC}$ = 1.5 and subsequently appears on the top and the bottom of the particles (as observed with respect to the TGO interface). In contrast, the crack initiates in the periphery of the particles (i.e., "outside") when $\alpha_P/\alpha_{TC}$ = 0.5 as may be observed in Fig. 4.2b. This example illustrates that the nucleation of cracks depends strongly on the CTE mismatch. The results of all the cases considered are summarised in Fig. 4.3 in terms of the crack initiation temperature in the TC layer as a function of the topological/spatial parameters. From the figure corresponding to $\alpha_P/\alpha_{TC}$ = 1.5, it can be observed that the spatial parameters have, in general, a considerable influence on the crack initiation temperature. In particular, the interparticle orientation has a more significant influence on the crack initiation temperature than the interparticle distance. The crack initiation occurs earlier in the case when the particle is located one below the other as opposed to the case where they are located side by side. The following explanation holds for such observation. For the considered thermal mismatch and the loading condition (cooling), when the particles are located one below the other, given by $\theta = 90^0$, tensile stresses are generated on the top and the bottom interface regions of both the particles. This, in turn, leads to further amplification of the driving force for the crack initiation and evolution due to the interaction between the stress fields associated with each particle. On the other hand, when $\theta = 0^0$, such tensile-tensile stress field interaction does not occur, rather a compressive-compressive stress field interaction results from such a spatial positioning of the particles. Thus, naturally, for the considered thermal mismatch ratio, the temperature drop (during the cooling process) required for crack initiation increases as the angle between the particles is decreased from 90 to 0 degrees. In terms of the interparticle distance, as highlighted above, the influence is rather less than that of the orientation as can be observed from Fig. 4.3. For the
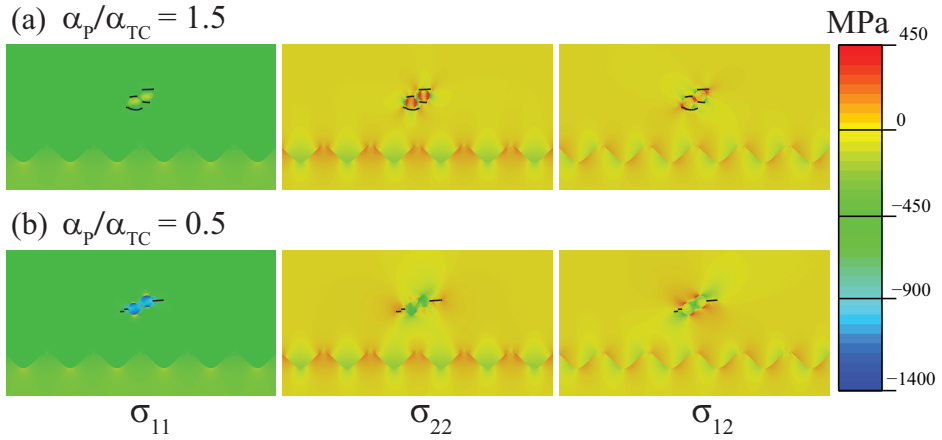
Figure 4.2: Stress distribution at $T = 30^0$C with $D_P/R_P = 0.5$ and $\theta = 30^0$ for two different CTE mismatch ratios: (a) $\alpha_P/\alpha_{TC} = 1.5$ and (b) $\alpha_P/\alpha_{TC} = 0.5$.
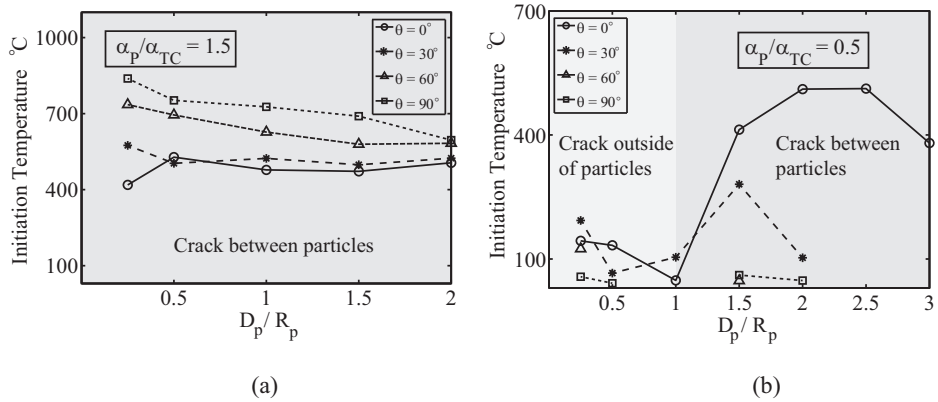


Figure 4.3: Crack initiation temperature vs interparticle distance for different particle orientations and for two different CTE mismatch ratios: (a) $\alpha_P/\alpha_{TC} = 1.5$ and (b) $\alpha_P/\alpha_{TC} = 0.5$. For $\alpha_P/\alpha_{TC} = 0.5$, the two shaded regions marks the location of crack initiation. In the dark grey region ($D_P/R_P > 1$) the cracks are initiated between the particles while in the light grey region ($D_P/R_P < 1$) the cracks are initiated outside of the particles.

orientations, $\theta = 60^0$ and $90^0$ there is a general tendency that the crack initiation is delayed as the interparticle distance is increased. On the other hand, for $\theta = 30^0$ and $0^0$, the trend is not monotonic, and it can be said that the interparticle distance does not play an influencing role on the crack evolution on an average sense.

The results corresponding to the case of the thermal mismatch ratio $\alpha_P/\alpha_{TC} = 0.5$ are shown in Fig.4.3, where the thermal expansion coefficient of the particle is lower

than that of the TC matrix. In this case, the trend is in general reversed as compared
to the previous case albeit with a distinct behaviour observed until the interparticle
distance reaches a value of 1. When the interparticle distance reaches the value equal
to 1, the temperature drop required for the crack initiation is significantly larger. The
trend in the variation of the crack initiation temperature is not monotonic, which can
be attributed to the following observation of crack patterns: Until the interparticle
distance reaches the value of 1, the microcracks are initiated in a region outside of the
particle pair, whereas when the interparticle distance is increased beyond the value
of 1, cracking occurs in the region between the two particles.

### MULTIPLE PARTICLES SIMULATION SETUP

In this subsection, the results for the second simulation set up where a random
distribution of healing particles is considered are presented. The volume fraction
of the MoSi$_2$ particles is approximately 15% chosen in accordance with the self-
healing TBC systems considered in [NEC$^+$18, KMZC$^+$16]. All healing particles have
the same radius $R_P$=7.5 $\mu$m as used in the two-particle simulation set up. To evaluate
the effect of the thermal mismatch parameter, five different values are considered
in the analysis given by $\alpha_P/\alpha_{TC}$ = 1.5, 1.25, 1, 0.75 and 0.5. The results of the
simulations are reported in terms of the fracture pattern as shown in Fig. 4.4. Upon
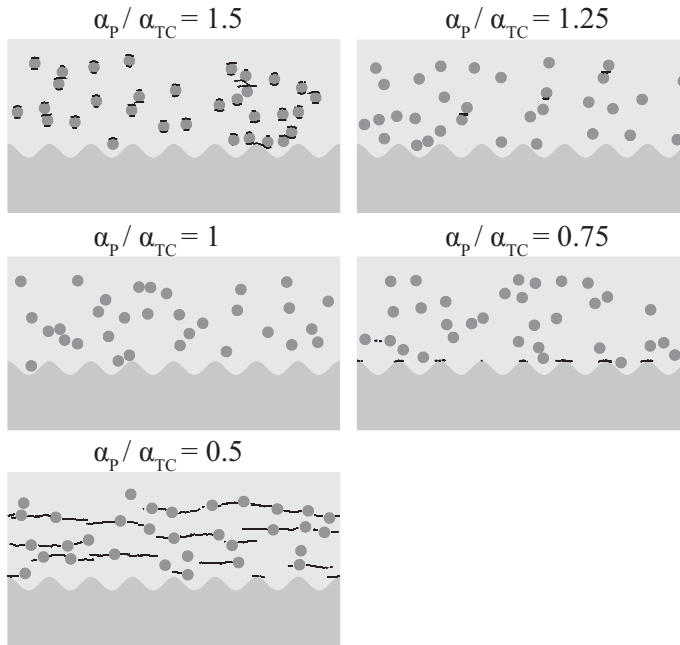


Figure 4.4: Self-healing TBC system showing the degree of microcracking for various CTE mismatch ratios.

observing the cracking patterns, it can be inferred that the thermal mismatch ratio has a significant influence on the crack initiation and evolution. In particular, the fracture patterns are distinctly different for different mismatch values. In general, for a mismatch ratio larger than 1, microcracks initiate at the top and bottom edges of the healing particles, whereas for mismatch ratios lower than one, the tendency is that the cracking occurs at the left and right sides of the particles. As expected, no cracking is observed for the mismatch ratio equal to 1, i.e., the particle and the TC layer having identical values of thermal expansion coefficients. Any deviation from this value generates thermal mismatch stresses, which in turn leads to crack initiation, the severity of which depends upon the magnitude of the CTE mismatch. One interesting observation is that for the case of $\alpha_P/\alpha_{TC} = 0.75$, micro-cracks are also initiated near the TC/BC interface as observed from the figure, revealing the complex effect that the CTE mismatch has on the failure behaviour of the TBC systems. Further detailed quantification in terms of the crack initiation temperature and total crack length can reveal the fracture characteristics in the TBC as a function of CTE mismatch. The results of such quantification are summarized in Fig. 4.5 whereby the crack initiation temperature and the total crack length are plotted against the thermal mismatch ratio.
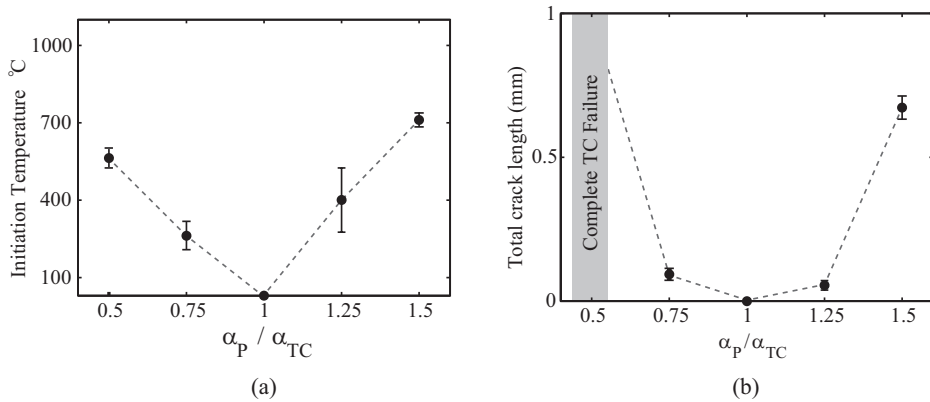
**4**



(a)

(b)

Figure 4.5: Variation of (a) crack initiation temperature and (b) total crack length for different CTE mismatch ratios $\alpha_P/\alpha_{TC}$ = 1.5, 1.25, 1, 0.75 and 0.5. For the CTE mismatch ratio of 0.5, there is a complete failure of the TC before reaching the final temperature ($30^o$C) as indicated by a grey shade.

As discussed before, five realisations are considered for each case of thermal mismatch ratio. Hence an average value is plotted along with the discrete standard deviations. The crack initiation occurs earlier in the TC layer with the increase or decrease in the CTE mismatch ratio from the value of 1 as shown in Fig. 4.5. The crack intiation behavior due to the CTE mismatch is qualitatively similar to the reported trend [LYS+91] quantified through a nondimensional mismatch parameter in ceramic composites. From the total crack length vs CTE mismatch plot, it

can observed that for the case of thermal mismatch ratio of $\alpha_P/\alpha_{TC} = 0.5$, the matrix failed completely, which is attributed to the fact that the crack initiates on the left and right edges of each particle, making it far easier to grow further. In other words, once the microcracks are formed on the left and right edges of each healing particle, the stress fields associated with the microcracks corresponding to each particle synergistically interacts with the stress fields of the neighbouring microcracks (of the neighbouring particle). This, in turn, results in the interaction and further amplification of the stress fields and thus ultimately resulting in failure of the matrix. On the other hand, for the mismatch ratio $\alpha_P/\alpha_{TC} = 1.5$, such interactions do not occur due to the crack initiation locations, thus resulting in a relatively lower total crack length. It is generally observed that any CTE mismatch between the particles and the matrix would lead to thermal stresses and in turn result in possible microcracking, thus potentially weakening the self-healing material. In the research on extrinsic self-healing ceramics reported in [BKvdZS16, BBvdZS18], the CTE mismatch between the healing particles and the ceramic matrix is considered as one of the important criteria for the selection of the healing agent. In contrast, for metal matrix particulate composites [THKY90, CS01] the CTE mismatch between the particle and the metal matrix is found to improve the strength and toughness of the composite material owing to the induced plastic deformation of the matrix.

### 4.3.2. MODEL INTEGRATION

In this subsection, a correlation is made between the results obtained from the random distribution of multiple particles with the two-particle case. The crack initiation temperature is used for the correlation using the results corresponding to two thermal mismatch coefficients namely $\alpha_P/\alpha_{TC}$ equal to 0.5 and 1.5. In the TBC system with a random particle distribution, the spatial metrics of the particles are quantified in terms of the distance and the orientation between the adjacent pair of particles, which is then used to correlate with the two-particle TBC case. The results of the comparison are shown in Fig. 4.6, in which the crack initiation temperature is plotted for both TBC configurations as a function of the spatial metrics. The results corresponding to the two-particle case are plotted as lines and those of the multiple particle cases are plotted as dark dots superimposed onto the two-particle plots. From the results, it can be observed that the two-particle case correlates very well with the results corresponding to the TBC system with a random distribution of multiple particles. For instance, in Fig. 4.6 corresponding to the case of $\alpha_P/\alpha_{TC}$ = 1.5, the crack initiation occurs in the vicinity of the particles whose normalised interparticle distance is between 0 and 1 and the angular orientation is between 60 to 90 degrees. In the other case for a lower thermal expansion coefficient for the particles, the crack initiation occurs in the vicinity of the particles whose interparticle distance is between 2 and 3 and the orientation is between 0 and 15 degrees. In both cases, the results from the two-particle and multiple particle cases correlate well. This indicates that a two-particle simulation is sufficient to study the interaction between
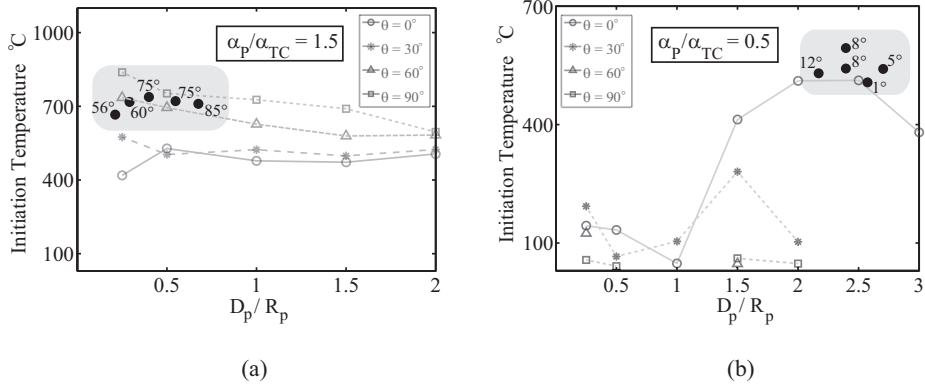
(a)                                                              (b)

Figure 4.6: Correlation of crack initiation temperature of multiparticle simulation with two particle simulation case for $\alpha_P/\alpha_{TC}$ = 0.5 and 1.5. This figure is analogous to Fig. 4.3, but the new data points marks the crack intiation temperature of multiparticle simulations (five different realisations) along with the angular dependence.

the healing particles and the TBC layers in terms of crack initiation characteristics.

### 4.3.3. EFFECT OF PARTICLE STRENGTH

The second material parameter considered in this study is the effect of the relative fracture strength of the particle with respect to the TC layer, defined by the ratio ($\sigma_P/\sigma_{TC}$). To investigate the effect of the strength mismatch parameter, analyses are conducted for three different values of particle strength ratio, 0.5, 1 and 3. Two subsets of analyses are conducted, one with varying the ratio of normal (tensile) strength of the particle relative to the TC matrix by keeping the shear strength ratio fixed and equal to 1. In the second subset, the ratio of the shear strength of the particle to that of the TC matrix is varied, while the normal strength ratio is kept equal to 1. Two CTE mismatch ratios $\alpha_P/\alpha_{TC}$ = 0.5 and 1.5 are considered. The resulting fracture patterns obtained from the simulations are reported in Fig. 4.7.

The results corresponding to the thermal mismatch, $\alpha_P/\alpha_{TC}$ = 1.5 is shown in the upper part of the figure. From the results, it is evident that the shear strength ratio has no influence on the fracture pattern, whereas the ratio of the normal strength affects the fracture pattern noticeably. This is due to the fact that for the chosen thermal mismatch, tensile stresses are generated within the particles, making the particle cracking prone to tensile fracture properties, rather than shear. In the case of tensile strength ratio, distinct fracture mechanisms are observed when comparing the crack patterns for the normal strength ratios, 0.5 and 3. In particular, particle shattering occurs when the normal strength ratio is less than or equal to 1. The same type of failure mode (particle shattering) is also reported experimentally in [MTL91] when the particles in a metallic matrix are subjected to tensile stresses. In the present case,
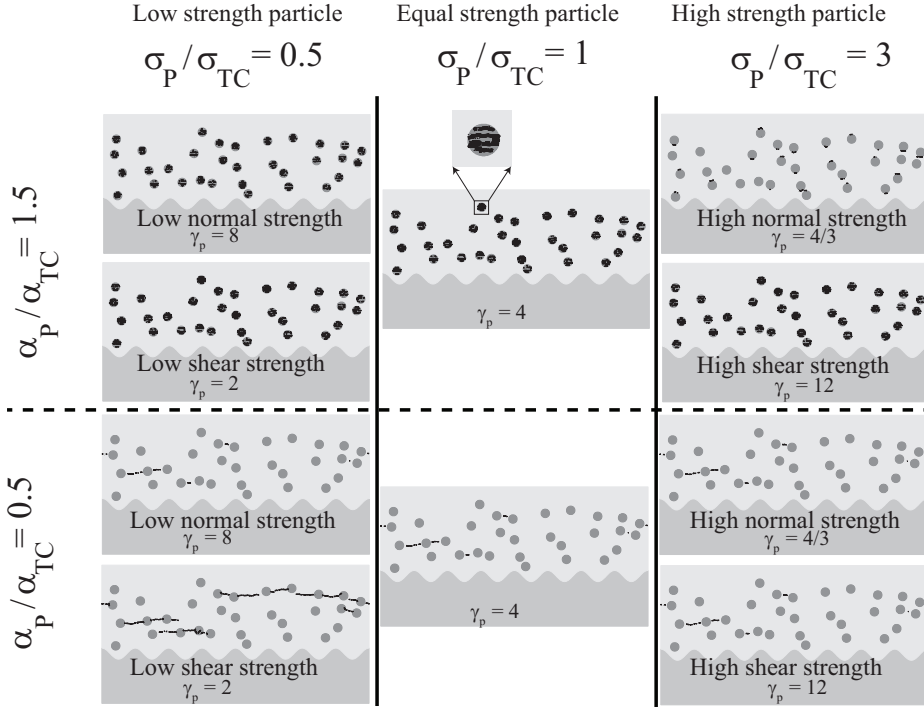
Figure 4.7: Fracture pattern corresponding to different particle strengths and two CTE mismatch ratios, $\alpha_P/\alpha_{TC}$ = 0.5 and 1.5. In this figure, low or high normal strength corresponds to the variation of particle normal strength for a fixed shear strength ratio of 1 and vice-versa. For $\alpha_P/\alpha_{TC}$ = 1.5 and the normal strength ratio ($\sigma_P/\sigma_{TC}$) <=1, the particle shattering is observed with multiple micro-cracks inside the particle. For $\alpha_P/\alpha_{TC}$ = 0.5, complete failure of the TBC occurs. The fracture pattern for this case is shown at T = 450$^o$C which shows particle fracture before the complete failure of the TBC.

the cracks in the particles do not grow into the TC matrix owing to the compressive stress fields in the TC layer under cooling. On the other hand, for the normal strength ratio of 3, microcracks form in the TC layer close to the top and bottom proximities of the particles but leave the particles uncracked. In the case of the shear strength ratio, as explained above, no influence is observed, leaving similar fracture patterns for all the three cases given by shear strength ratio = 0.5, 1 and 3.

The fracture patterns corresponding to the thermal mismatch ratio equal to 0.5 are shown in the lower part of Fig. 4.7. One important difference between the results corresponding to the CTE mismatch 0.5 and 1.5 is that complete failure of the TBC occurs when the CTE mismatch is equal to 0.5. This can be attributed to the fact the stress field in the TC layer adjacent to the particles (to the left and the right) is tensile in nature leading to microcrack initiation in the vicinity of the particles. Further, the favourable orientations of these microcracks lead to their coalescence resulting in a

large macrocrack, hence the complete failure of the TBC before reaching the room temperature. To illustrate the effect of the strength mismatch the fracture pattern shown in Fig. 4.7 for $\alpha_P/\alpha_{TC} = 0.5$ corresponds to the temperature $450^oC$ (i.e., before complete failure). Corresponding to this point of the loading history and for this CTE mismatch ratio, the role of the normal and shear strength ratios are shown in terms of the resulting fracture patterns. In principle, the influence of the strength ratios for the CTE mismatch equal to 0.5 reverses as compared with the CTE mismatch ratio equal to 1.5, see Fig. 4.7. Specifically, the ratio of the normal strength does not influence the fracture pattern, whereas the shear strength ratio has an effect on the fracture pattern. This is primarily because compressive stresses result in the particles due to the lower CTE of the particle with respect to the TC matrix. Thus, the shear mode of failure is dominant, and the normal stress-induced cracking is prevented due to the presence of such compressive stress field within the particles.

### 4.3.4. EFFECT OF INTERFACE STRENGTH

The third material parameter of interest is the strength of the interface between the healing particles and the matrix. For instance, the numerical study presented in [IRC+91] reveals the influence of thermomechanical stresses induced by the CTE mismatch on interface failure of the particulate composite. In the present study, the effect of variation of the interface strength with respect to the strength of TC layer ($\sigma_{i_{P/TC}}/\sigma_{TC}$) on the fracture pattern of the TBC is considered. To explore this effect, again two subsets of simulations are carried out for the two sets of CTE mismatch values, $\alpha_P/\alpha_{TC} = 1.5$ and 0.5 as conducted in the particle strength case. In the first subset, the interface normal strength is varied for a fixed interface shear strength ratio equal to 1. In the second case, the interface shear strength is varied by fixing the interface normal strength with a value equal to 1. The results of the simulations for the different interface strength ratios, $\sigma_{i_{P/TC}}/\sigma_{TC} = 0.5$, 1 and 3 are shown in Fig. 4.8. The figure resembles to Fig. 4.7 to a high degree for the CTE mismatch ratio of 0.5 but instead of particle cracking, interface debonding is observed.

The fracture patterns corresponding to the CTE mismatch, $\alpha_P/\alpha_{TC} = 1.5$ are summarized in the upper part of the figure for various normal and shear strength ratios. From the results, it can be observed that the normal strength ratio has a noticeable influence on the fracture pattern, whereas the shear strength ratio does not affect the fracture pattern as can be seen from the figure. This is again due to the effect of tensile stress fields in and around the particles for the considered thermal mismatch. Such an effect of the normal strength is visible from the fracture pattern corresponding to the higher and the lower values of the normal strength ratios, in which the interface debonding becomes less severe when the normal strength ratio of the interface is increased to the value 3. The fracture patterns corresponding to the variation in the shear strength ratios are not altered.

For the CTE mismatch, $\alpha_P/\alpha_{TC} = 0.5$, the fracture patterns are shown in the bottom portion of Fig. 4.8. It is worth mentioning that for this CTE mismatch case,
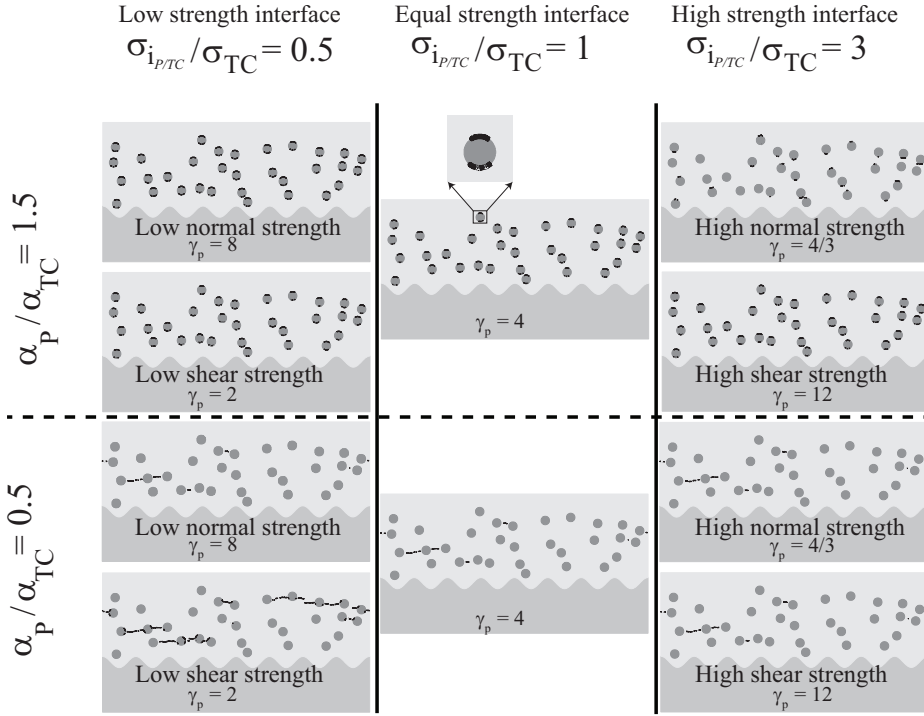
Figure 4.8: Fracture pattern corresponding to different interface strengths and two CTE mismatch ratios $\alpha_P/\alpha_{TC}$ = 0.5 and 1.5. In this figure, low or high normal strength corresponds to the variation of interface normal strength for a fixed interface shear strength ratio of 1 and vice-versa. For $\alpha_P/\alpha_{TC}$ = 1.5 and the normal strength ratio ($\sigma_{i_{P/TC}}/\sigma_{TC}$) <=1, the interface debonding occurs at the top and bottom sides of the particles. For $\alpha_P/\alpha_{TC}$ = 0.5, complete failure of the TBC occurs. The fracture pattern for this case is shown at at T = $450^o$C which shows interface debonding between the particle and the TC before the complete failure.

complete failure of the TBC occurs, as was the case in the particle strength study. Nonetheless, to reveal the effect of the interface strength mismatch, the fracture patterns before the complete failure are reported, i.e., at a temperature $450^o$C. Upon comparison of the fracture patterns for the two CTE mismatch values, the effects of the normal and the shear strength ratios are reversed. A similar observation was made in the particle strength study. The resulting fracture patterns reveal that changes in normal strength ratio of the interface do not influence the fracture pattern. On the other hand, a decrease in the shear strength leads to more microcracks resulting from the interface debonding, as in the particle strength study. The primary difference between the particle strength and the interface strength studies is that the interface debonding occurs in a stress field which is severely inhomogeneous along the interface, whereas the stress field within the particle (whether tensile or

compressive) is largely homogeneous until crack initiation sets in.

In general, a weak interface can degrade the TBC mechanical properties, but would possibly offer the potential of exposing the TBC microcracks to the healing agent contained within the particle.

## 4.4. CONCLUSIONS

Finite element simulations of fracture evolution in TBC systems with embedded solid healing particles were conducted to investigate the effect of geometric and material properties of the healing particles on the crack pattern. Two different configurations of the unit-cell based TBC were analysed, one with a single pair of healing particles and the other with a random distribution of healing particles. The effects of CTE and strength mismatch between the particles and the TC layer were studied using parametric simulations. The following conclusions are drawn from the study.

- In addition to the CTE mismatch, the two-particle setup also captures the effect of topological distribution of the healing particles, characterised by the interparticle distance ($D_P/R_P$) and the particle orientation ($\theta$) on the important fracture determining parameter (crack initiation temperature) quite well.

- In the two-particle case, for the higher CTE mismatch ratio ($\alpha_P/\alpha_{TC}$ = 1.5), the particle orientation has a more significant effect on the crack initiation temperature than the interparticle distance whereas for the lower CTE mismatch ratio ($\alpha_P/\alpha_{TC}$ = 0.5), both the orientation and the interparticle distance has a substantial effect on the crack initiation temperature.

- From the results of the multiple-particle simulations, it can be inferred that introducing the healing particles in a TBC can significantly alter the fracture pattern as compared to that of a conventional TBC system. The resulting fracture pattern is strongly determined by the CTE mismatch between the healing particles and the TC layer. In the present study, significant cracking is induced when $\alpha_P/\alpha_{TC}$ > 1.25 or $\alpha_P/\alpha_{TC}$ < 0.75. It is worth mentioning that for $\alpha_P/\alpha_{TC}$ < 1, microcracks appear to the left and the right of the healing particles, whereas for $\alpha_P/\alpha_{TC}$ > 1, the cracks appear on the top and the bottom of the healing particles.

- Very good correlations between the dual particle TBC setup and the TBC set up with a randomly distributed array of particles were observed in terms of the crack initiation temperature.

- The fracture strengths of the particle and the particle/matrix interface have a strong influence on the fracture mechanism in the TBC. Further, for the higher CTE mismatch ratio, the normal strengths of the particle and that of the interface have a prominent effect on the crack pattern as compared to the shear strengths ratios and for the lower CTE mismatch ratio, the shear strengths of the

particle and that of the interface have a prominent effect on the crack pattern as compared to the normal strengths ratios.

From the perspective of a successful self-healing TBC design, it can be suggested that $\alpha_P/\alpha_{TC} < 1$ along with lower relative fracture strength of the healing particles are desirable. Under such conditions, healing activation is favored as the observed fracture patterns reveal that the particles are open for the crack to heal in the TC layer. However, significantly lower values of $\alpha_P/\alpha_{TC}$ ($\leq 0.5$) will lead to deterioration of the integrity of the TBC system resulting in premature failure. If the coefficient of thermal expansion of the particle is greater than the CTE of the TC ($\alpha_P/\alpha_{TC} > 1$), the simulation suggest to avoid multiple layers of particles.

**4**

# 5

# COHESIVE ZONE-BASED CRACK HEALING MODEL

[1]A cohesive zone-based constitutive model, originally developed to model fracture, is extended to include a healing variable to simulate crack healing processes and thus recovery of mechanical properties. The proposed cohesive relation is a composite-type material model that accounts for the properties of both the original and the healing material, which are typically different. The constitutive model is designed to capture multiple healing events, which is relevant for self-healing materials that are capable of generating repeated healing. The model can be implemented in a finite element framework through the use of cohesive elements or the extended finite element method (XFEM). The resulting numerical framework is capable of modelling both extrinsic and intrinsic self-healing materials. Salient features of the model are demonstrated through various homogeneous deformations and healing processes followed by applications of the model to a self-healing material system based on embedded healing particles under non-homogeneous deformations. It is shown that the model is suitable for analyzing and optimizing existing self-healing materials or for designing new self-healing materials with improved lifetime characteristics based on multiple healing events.

## 5.1. INTRODUCTION

Though extensive research has been conducted in realizing self-healing material systems experimentally, efforts to develop computational models that could simulate fracture and healing have been scarce. Simulation-based design guidelines can be

---

[1]This chapter also appears in the doctoral thesis of Sathiskumar A. Ponnusami entitled "Modelling fracture and healing in particulate composite systems"

used to optimize self-healing systems. Consequently, the goal of the present work is to develop a computational framework to model the effect of crack healing behavior on the mechanical performance of the material or the structure under consideration. The modelling and computational framework is kept sufficiently general such that it is capable of analyzing both extrinsic and intrinsic self-healing materials.

In the context of a capsule (or fiber)-based extrinsic self-healing system, there are two critical aspects that need to be addressed in order to achieve a robust self-healing system. Firstly, a crack initiated in the host (or matrix) material should be attracted towards the healing particle (or fiber) and further should break the particle for healing to occur. Crack-particle interaction, which is a crucial aspect to successfully trigger the healing mechanism, has been analyzed parametrically in [PTvdZ15, PTZX15] to generate design guidelines for the selection of the healing particles in terms of their mechanical properties. Other studies in the literature have utilized analytical and numerical techniques to investigate the interaction between the crack and the healing particles or capsules [ZJV11, GGvP17, ŠFA+16]. The second critical aspect in a self-healing system, relevant for both extrinsic and intrinsic mechanisms, is centered on how the material recovers its mechanical properties once the healing mechanism is activated in or near the fracture surfaces. In particular, the recovery of load-carrying capability as a function of healing parameters, crack length and capsule properties is a subject of importance but has not received adequate attention in the literature yet. Consequently, one main focus of the present chapter is to simulate the recovery of mechanical properties of the self-healing system.

Research efforts have been made in the literature to model the mechanical behavior of materials taking both fracture and healing into account. Most of the existing models adopt a continuum damage mechanics-based approach whereby cracking and healing are interpreted as a degradation or recovery of material stiffness and strength [BGL05, VSLK12, VSL11, MS13, DARL12, XSKZ14, OON16]. The common feature of these models is that the internal variables describing the continuum degradation and healing of the material refer to the effective behavior of (unresolved) cracking and healing events. Correspondingly, details at the level of individual cracks are not explicitly taken into account. However, a direct description at the level of individual cracks and healing particles is desirable in view of designing or fine-tuning a self-healing material.

Cohesive zone-based approaches have also been proposed for modelling crack healing. Unlike continuum damage models, the advantage of the above cohesive zone approaches is that the material damage is treated in a discrete manner as cohesive cracks, which allows for explicit modelling of crack evolution and its healing. In [MG06], crack healing is simulated through an artificial crack closure technique by introducing a wedge into the crack. The methodology is implemented in a finite element framework using cohesive elements for simulating fracture and a contact law that enforces the conditions for crack healing or retardation. In [SR06] a Mode I exponential cohesive zone model is proposed to simulate crack healing by

introducing a jump in crack opening displacement. After model verification, they applied the framework to simulate delamination crack healing in a slender beam specimen to show the capability of the model. Some limitations of the model are with regard to the multiple healing events and their one-dimensionality. In [UKP09], a cohesive zone model for fatigue crack growth is developed, which also considers crack retardation during unloading regimes. In [AAR15] a thermodynamics-based cohesive zone methodology is used to model crack healing behavior by extending previous work on continuum damage-healing mechanics [DARL12]. The model takes into account the effect of various parameters such as temperature, resting time and crack closure on the healing behavior. However, the fracture properties of the healed zone, upon complete healing, assume the values of the original material, which is often not the case even for intrinsic self-healing materials. Furthermore, the capability of simulating multiple healing events is not demonstrated in many of the above-mentioned studies, which is of direct relevance for intrinsic self-healing materials or extrinsic systems with a continuous supply of healing agent. Other modelling approaches explored in the literature to simulate crack healing behavior are based on the theory of porous media [BSS15] or the discrete element method [LS08, HL08].

To overcome the limitations in the existing models in the literature, a generalized cohesive-zone based crack healing model is developed here, which can be applied to both extrinsic and intrinsic self-healing materials. The model is capable of simulating property recovery after multiple healing events and is also able to handle different fracture properties for the healing material as compared to that of the original material. An additional feature of the model is that the properties of the healing material may be specified separately for different healing instances. This is particularly important as the recovery of the fracture properties in the healed zone is not always complete, resulting in varying fracture properties for each healing instance that depend, among others, on healing time, diffusion-reaction characteristics and temperature. It is noted that the model developed here does not explicitly aim to capture the actual healing kinetics, but to simulate the recovery of the overall load bearing capacity as a function of crack filling and fracture properties of the filling material. Nonetheless, detailed healing kinetics of a material can be coupled to the present model through fracture properties and crack filling behavior to simulate specific materials.

## 5.2. MODELLING OF FRACTURE AND HEALING

The cohesive zone-based fracture mechanics model presented in [CSVdB10] is extended to model both the fracture and the healing in a unified constitutive relation. In the present fracture-healing framework, the following modelling considerations are made. Firstly, the crack healing model does not include healing kinetics explicitly, rather the focus is to develop a methodology to simulate cracking and the recovery of mechanical integrity upon healing. Consequently, whenever the healing process is

activated at a location within the cohesive crack, the resting period is assumed to be sufficiently long such that complete healing occurs. This assumption is not necessary per se, but enforced in order to have a specific focus on recovery of mechanical properties using a modified cohesive constitutive relation. Nonetheless, depending upon the type of healing process involved in a specific healing material system, appropriate healing kinetics can be treated separately and coupled with the present framework. This, in turn, can govern the effect of parameters such as resting time and temperature on the degree of healing, which can then be fed as an input to the present framework through appropriately defined fracture properties of the healed material phases.

### 5.2.1. COHESIVE CRACK MODEL WITHOUT HEALING

The cohesive zone model employed in this work corresponds to a bilinear relation given by $T$, which is a scalar measure of the traction $t$ transmitted across the cohesive surface, as a function of $\Delta$, which is a scalar measure of the cohesive surface opening displacement vector $\delta$. Though several other cohesive relations have been proposed in the literature, a bilinear relation captures the essential ingredients of most cohesive relations, namely the cohesive strength $\sigma_c$ and the fracture energy $G_c$, which are viewed as variable material properties in the present healing model. The traction $T$ increases with increasing cohesive surface opening displacement $\Delta$ up to a maximum value given by the strength, $\sigma_c$, and eventually decreases to zero, at which point the cohesive zone is fully-separated in the sense that no (positive) traction can be transmitted across the surface. The initial (increasing) part of the cohesive response is useful in conjunction with cohesive elements but may be omitted for XFEM implementations where the cohesive relation is only activated when the critical value $\sigma_c$ is reached. The area under the traction-separation curve, which represents the total work per unit area expended in creating a fully-separated crack, corresponds to the fracture energy $G_c$ of the material.

An effective crack opening displacement variable is introduced as follows:

$$\Delta := \sqrt{\langle \delta_n \rangle^2 + \gamma^2 (\delta_s)^2}, \tag{5.1}$$

where $\delta_n$ and $\delta_s$ are, respectively, the normal and tangential components of the crack opening displacement vector $\delta$ resolved in a coordinate system aligned with the local normal and tangential directions of a crack surface. In (5.1), $\langle \cdot \rangle := (\cdot + |\cdot|)/2$ refers to the Macaulay bracket and $\gamma$ is a non-dimensional weighting factor for the normal and tangential contributions given by

$$\gamma := \frac{\delta_{n,0}}{\delta_{s,0}},$$

where $\delta_{n,0}$ and $\delta_{s,0}$ denote, respectively, the crack opening at the onset of failure for a pure normal and a pure tangential opening with respect to the crack surface.

In order to determine whether the crack opening is increasing or decreasing due to the external loading process, the following loading function $f$ is used:

$$f = \hat{f}(\Delta, \kappa) := \Delta - \kappa, \tag{5.2}$$

where $\kappa$ is a damage history variable that, at a given time $t$, corresponds to the maximum value attained by the equivalent crack opening during a process up to that time, i.e.,

$$\kappa(t) := \max_{\bar{t} \in [0,t]} \Delta(\bar{t}) .$$

The Karush–Kuhn–Tucker relations for the loading and unloading conditions can be expressed as follows:

$$f\dot{\kappa} = 0, \qquad f \leq 0, \qquad \dot{\kappa} \geq 0, \tag{5.3}$$

where $\dot{\kappa}$ indicates the (time) rate of change of the damage history variable with $\dot{\kappa} > 0$ corresponding to an active damage step and $\dot{\kappa} = 0$ to an "elastic" step.

The equivalent crack opening is used to compute the equivalent traction $T$ as

$$T = \hat{T}(\Delta, \kappa) = \begin{cases} \hat{g}(\Delta) & \text{if} \quad f = 0 \text{ and } \dot{\kappa} > 0, \\[2mm] \hat{g}(\kappa)\dfrac{\Delta}{\kappa} & \text{otherwise,} \end{cases} \tag{5.4}$$

where $\hat{g}$ is the effective traction-separation law. The upper and lower expressions in (5.4) provide the equivalent traction during, respectively, crack growth and unloading/reloading.

The specific form of the effective traction-separation law used in the present work is a linear softening relation, which corresponds to

$$g = \hat{g}(\Delta) = \sigma_c \frac{\langle \Delta_f - \Delta \rangle}{\Delta_f - \Delta_i} . \tag{5.5}$$

In the above expression, the parameters $\Delta_i$ and $\Delta_f$ are, respectively, the equivalent crack opening at the onset of softening and the maximum equivalent crack opening. These parameters may be chosen such that, for a given fracture strength $\sigma_c$, fracture toughness $G_c$ and an initial cohesive stiffness $K$,

$$\Delta_i = \frac{\sigma_c}{K} , \qquad \Delta_f = \frac{2G_c}{\sigma_c} ,$$

where the initially linearly "elastic" loading up to the fracture strength in a bi-linear law can be reproduced in (5.4) by assigning an initial damage $\kappa(0) = \kappa_0 = \Delta_i$. The parameters $\Delta_i$ and $\Delta_f$ are chosen such that the maximum of the function $\hat{T}$ in (5.4) equals the fracture strength $\sigma_c$ and the integral of $\hat{T}$ from $\Delta = 0$ to $\Delta = \Delta_f$ equals the material fracture energy (toughness) $G_c$.

After evaluating (5.4), the normal and shear tractions can be computed as

$$
t_\text{n} =
\begin{cases}
\dfrac{\delta_\text{n}}{\Delta} T & \text{if} \quad \delta_\text{n} > 0, \\[2ex]
K\delta_\text{n} & \text{if} \quad \delta_\text{n} < 0,
\end{cases}
\tag{5.6}
$$

$$
t_\text{s} = \quad \gamma^2 \frac{\delta_\text{s}}{\Delta} T,
$$

i.e., for $\delta_\text{n} \geq 0$, one has that $\boldsymbol{t} \cdot \boldsymbol{\delta} = T\Delta$.

### 5.2.2. CRACK HEALING MODEL

The cohesive relation summarized in the previous section can be extended to formulate a cohesive crack-healing model. The single healing case is discussed first, which is then followed by a generalized model capable of multiple healing events.

#### SINGLE HEALING EVENT

The proposed crack healing model is a composite-based constitutive model for simulating the recovery of fracture properties upon activation of crack healing. The traction components of the composite response, $\tilde{t}_\text{n}$ and $\tilde{t}_\text{s}$, are expressed as a weighted sum of the traction contributions from the original material, $t_\text{n}^{(0)}$ and $t_\text{s}^{(0)}$, and the healing material $t_\text{n}^{(1)}$ and $t_\text{s}^{(1)}$, as follows:

$$
\tilde{t}_\text{n} = w^{(0)} t_\text{n}^{(0)} + w^{(1)} t_\text{n}^{(1)} \qquad \tilde{t}_\text{s} = w^{(0)} t_\text{s}^{(0)} + w^{(1)} t_\text{s}^{(1)}
\tag{5.7}
$$

where the superscripts (0) and (1) represent the original and healing materials, respectively. The weighting factors $w^{(0)}$ and $w^{(1)}$ introduced in (5.7), which can take values between 0 and 1, are the primary parameters in the model and can be interpreted as the surface-based volume fractions of the original and healing material respectively at the instance of healing activation. The meaning of "volume fraction" in this context refers to the fraction of the crack area occupied by a material per unit crack opening displacement. In a two-dimensional setting, the crack area fraction refers to the crack length fraction per unit depth. As indicated in (5.7), it is assumed that a partially damaged area that has been healed contains contributions from both the original material and the healing material. Correspondingly, the weighting factors $w^{(0)}$ and $w^{(1)}$ are related to fractions of a partially damaged surface where the original material is still capable of transmitting a force (in the sense of a cohesive relation) while the healing material has occupied the complementary region. Observe that this assumption implies that the model is essentially based on an "equal strain" distribution among the phases (Voigt model), in this case with the crack opening playing the role of a strain-like variable. Consequently, the tractions in each phase may be overpredicted compared to a model based on an "equal stress" assumption (Reuss model), however the current Voigt-like model preserves kinematic compatibility whereas a Reuss-like model does not.

In order to develop the constitutive model, define an energy-based damage parameter $D^{(0)}$ as follows:

$$D^{(0)}(t) := \frac{G_{\mathrm{d}}^{(0)}(t)}{G_{\mathrm{c}}^{(0)}} \tag{5.8}$$

which represents the ratio between the energy dissipated $G_{\mathrm{d}}^{(0)}(t)$ during decohesion of the original material up to time $t$ and the fracture energy $G_{\mathrm{c}}^{(0)}$ (work required for complete decohesion of the original material). In a bilinear cohesive relation, as presented in Sec. 5.2.1, this parameter may be approximated as

$$D^{(0)}(t) \approx \frac{\kappa^{(0)}(t)}{\Delta_{\mathrm{f}}^{(0)}}$$

where the initial, undamaged "elastic" response has been neglected (namely it is assumed in (5.5) that $\Delta_{\mathrm{f}}^{(0)} \gg \Delta_{\mathrm{i}}^{(0)}$).

Prior to healing, the cohesive response is characterized by the cohesive relation of the original material, i.e., with $w^{(1)} = 0$ in (5.7). If a single healing event occurs at a time $t = t^*$, the proposed constitutive model assumes that the factor $w^{(1)}$ is given by the value of the energy-based damage parameter at the instance of healing activation, $D^{(0)*}$, i.e.,

$$w^{(1)} = D^{(0)*} := \frac{G_{\mathrm{d}}^{(0)*}}{G_{\mathrm{c}}^{(0)}} \ . \tag{5.9}$$

Correspondingly, a value $w^{(1)} = 0$ upon healing activation represents zero equivalent damaged area fraction of the original material at a given material point (i.e., the original material is fully intact) while $w^{(1)} = 1$ represents a fully-damaged original material at a given material point (i.e., the healing material would occupy the fully damaged material point upon healing). The interpretation of (5.9) is that the volume fraction $w^{(1)}$ available for the healing material in order to fill and heal can be determined from the value of the energy-based damage parameter of the original material, defined in (5.8) at the instance of the healing activation. Upon healing of the available volume fraction $w^{(1)}$, the volume fraction of the original material, $w^{(0)}$, assumes a value equal to $1 - w^{(1)}$, which is equal to the equivalent undamaged area of the original material. Conversely, the energy-based damage parameter can be interpreted as an equivalent damaged area fraction at a given material point in the context of the cohesive zone framework. A schematic of the traction-separation relations for a material point under damage and healing is shown in Fig. 5.1 depicting the features of the model.

In accordance with (5.7) and (5.9), the effective fracture energy $\tilde{G}_{\mathrm{c}}$ of the composite material after healing becomes the weighted sum of the fracture energies of the original and healing materials, given as

$$\tilde{G}_{\mathrm{c}} = w^{(0)} G_{\mathrm{c}}^{(0)} + w^{(1)} G_{\mathrm{c}}^{(1)} \ . \tag{5.10}$$
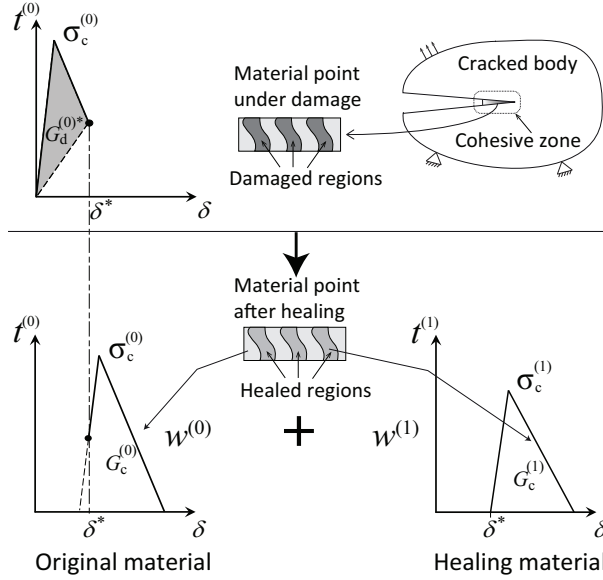
Figure 5.1: Traction-separation laws of original and healing material, which upon weighted addition, results in a composite cohesive relation for the crack-healing model.

### TRACTION-CRACK OPENING RELATIONS: ORIGINAL MATERIAL

The traction-separation relation corresponding to the original material *after healing* is governed by a modified effective displacement-based cohesive crack model explained as follows: The effective displacement for the original material defined in the conventional cohesive zone model is modified by introducing shifts in normal and tangential crack opening displacements to take into account the effect of healing. These shifts in the crack opening displacements lead to a modified effective displacement for the original material, $\Delta^{(0)}$, given as

$$\Delta^{(0)} := \sqrt{\left\langle \delta_n - \delta_n^{(0)*} \right\rangle^2 + \gamma^2 (\delta_s - \delta_s^{(0)*})^2}, \quad t \geq t^* . \tag{5.11}$$

The reason for introducing the shift is as follows: On activation of a healing process, the healing agent diffuses/flows through the crack and crack filling occurs thereby (fully or partially) reducing the crack opening. As a result, the crack opening displacements after complete healing should be considered nominally zero. To simulate this process, displacement shifts are introduced into the crack opening displacements, which make the nominal opening displacement zero upon complete healing. Further, a shift is also applied in the crack opening history variable, $\kappa$, which is reset to its initial value. This is done to simulate the intact portion of the original material point, whereas the damaged portion of the considered material point is

assumed to be healed by the healing material.

In a cohesive-zone model, a partially-damaged material has a non-zero crack opening displacement but it may still be capable of transmitting a force. In the present model, if healing is activated in a partially damaged surface, it is assumed that the process occurs at constant stress provided there is no change in the external loading.

The shifts introduced in the normal and the tangential crack opening displacements for the original material are given as follows:

$$
\begin{aligned}
\delta_n^{(0)*} &= \delta_n^* - t_n^*/(w^{(0)}K) \,, \\
\delta_s^{(0)*} &= \delta_s^* - t_s^*/(w^{(0)}K) \,.
\end{aligned}
\tag{5.12}
$$

In the above expressions, $\delta_n^*$ and $\delta_s^*$ are the actual crack opening displacements in the original material at the instant of crack healing activation. As shifts in crack opening displacements are introduced along with restoration of the crack opening history variable $\kappa$, the shifts in crack opening displacements are constructed in such a way that the tractions across the cohesive surface maintain their continuity. Consequently, the traction components $t_n^*$ and $t_s^*$ across the partially damaged surface remain the same before and after healing activation.

The normal and shear tractions corresponding to the original material during subsequent loading after healing are then obtained from the corresponding traction-separation relations (5.4) and (5.6) using the aforementioned equivalent opening $\Delta^{(0)}$, i.e.,

$$
t_n^{(0)} = 
\begin{cases}
\dfrac{(\delta_n - \delta_n^{(0)*})}{\Delta^{(0)}} T^{(0)} & \text{if} \quad \delta_n > \delta_n^{(0)*}, \\[2ex]
K(\delta_n - \delta_n^{(0)*}) & \text{if} \quad \delta_n < \delta_n^{(0)*},
\end{cases}
\tag{5.13}
$$

$$
t_s^{(0)} = \gamma^2 \frac{(\delta_s - \delta_s^{(0)*})}{\Delta^{(0)}} T^{(0)} \,.
$$

TRACTION-CRACK OPENING RELATIONS: HEALING MATERIAL

Similar to the original material, the traction-separation relations corresponding to the healing material are governed by a modified equivalent displacement variable, $\Delta^{(1)}$ defined as

$$
\Delta^{(1)} := \sqrt{\left\langle \delta_n - \delta_n^{(1)*} \right\rangle^2 + \gamma^2 (\delta_s - \delta_s^{(1)*})^2} \,,
\tag{5.14}
$$

where $\delta_n^{(1)*}$ and $\delta_s^{(1)*}$ are shifts applied to the traction-separation relation of the healing material. The shifts are introduced into the crack opening displacements of the healing material following the same approach as for the original material. The main difference is that the healing material is assumed to transmit zero load at the instant of healing activation. Thus, the shifts in crack opening displacements for the

healing material are the actual crack opening displacements at the instant of healing activation, i.e.,

$$\begin{aligned} \delta_{\mathrm{n}}^{(1)*} &= \delta_{\mathrm{n}}^* \\ \delta_{\mathrm{s}}^{(1)*} &= \delta_{\mathrm{s}}^*. \end{aligned} \tag{5.15}$$

Similar to the approach adopted for the original material after healing, the normal and tangential traction components corresponding to the healing material are obtained from an equivalent traction $T^{(1)}$ of the corresponding traction-separation relations (5.4) and (5.6) using the equivalent opening $\Delta^{(1)}$, i.e.,

$$t_{\mathrm{n}}^{(1)} = \begin{cases} \dfrac{(\delta_{\mathrm{n}} - \delta_{\mathrm{n}}^{(1)*})}{\Delta^{(1)}} \, T^{(1)} & \text{if} \quad \delta_{\mathrm{n}} > \delta_{\mathrm{n}}^{(1)*}, \\[3mm] K(\delta_{\mathrm{n}} - \delta_{\mathrm{n}}^{(1)*}) & \text{if} \quad \delta_{\mathrm{n}} < \delta_{\mathrm{n}}^{(1)*}, \end{cases} \tag{5.16}$$

$$t_{\mathrm{s}}^{(1)} = \gamma^2 \dfrac{(\delta_{\mathrm{s}} - \delta_{\mathrm{s}}^{(1)*})}{\Delta^{(1)}} \, T^{(1)}.$$

It is worth noticing that, in both the original and healing material phases, the shifts in the crack opening displacements are applied at the component level, i.e., individually on the normal and tangential components. The composite tractions $\tilde{t}_{\mathrm{n}}$ and $\tilde{t}_{\mathrm{s}}$, given in (5.7), are obtained through a rule-of-mixtures approach analogous to an equal strain assumption used for composite materials (in this case an equal crack opening assumption) with material-specific responses given by (5.13) and (5.16). This approach provides sufficient flexibility to specify separate material properties and fracture behavior for the original and healing materials.

### MULTIPLE HEALING EVENTS

The approach presented in the previous section can be extended to account for multiple healing events. This generalization is capable of dealing with a complex history of (partial) crackings and healings. In the sequel, the index $p$ refers to the number of healing events, ranging from 0 to $m$, with the convention that $p = 0$ represents the undamaged original state. The index $p$ may also be used to represent the healing material phase that is formed during the $p^{\text{th}}$ healing event, again with the convention that $p = 0$ corresponds to the original material. At the end of the $m^{\text{th}}$ healing event, the composite-like traction components $\tilde{t}_{\mathrm{n}}^{[m]}$ and $\tilde{t}_{\mathrm{s}}^{[m]}$ of the multiply-healed material are given by

$$\tilde{t}_{\mathrm{n}}^{[m]} = \sum_{p=0}^{m} w^{[m](p)} \, t_{\mathrm{n}}^{(p)} \qquad \tilde{t}_{\mathrm{s}}^{[m]} = \sum_{p=0}^{m} w^{[m](p)} \, t_{\mathrm{s}}^{(p)} \tag{5.17}$$

where $t_{\mathrm{n}}^{(p)}$ and $t_{\mathrm{s}}^{(p)}$ are the normal and tangential traction components of the $p^{\text{th}}$ material phase and $w^{[m](p)}$ is the volume fraction of the $p^{\text{th}}$ material phase (index in parentheses) present or created at the $m^{\text{th}}$ healing event (index in square brackets).

The relation given in (5.17) is a generalization of (5.7) for the case $m > 1$. For modelling purposes, a separate index is assigned to each new healing material created at the $p^{\text{th}}$ healing event even though the actual materials (chemical composition) may be physically the same. The purpose is to keep track of their individual evolutions throughout a complex loading and healing process starting at possibly different states (i.e., every healing instance is recorded separately). In accordance with the proposed constitutive model for the single healing event, it is assumed that the volume fraction $w^{[m](p)}$ of the $p^{\text{th}}$ material phase is related to the energy-based damage parameter of that phase prior to the $m^{\text{th}}$ healing event, which can be expressed recursively as

$$
w^{[m](p)} = \begin{cases}
1 & \text{for } p = m = 0, \\[2mm]
w^{[m-1](p)}(1 - D^{[m](p)}) & \text{for } 1 \leq p < m, \\[2mm]
\displaystyle\sum_{p=0}^{m-1} w^{[m-1](p)} D^{[m](p)} & \text{for } 1 \leq p = m.
\end{cases}
\tag{5.18}
$$

In the above expression, $D^{[m](p)}$ is the value of energy-based damage parameter $D^{(p)}$ corresponding to the $p^{\text{th}}$ healing phase at the $m^{\text{th}}$ healing event. With this notation, the term $D^{(0)^*}$ in (5.9) can alternatively be expressed as $D^{[1](0)}$ to indicate the value of the energy-based damage parameter evaluated at the instant at which the first healing event is activated. It is also to be noted that the sum of all $w^{[m](p)}$ is equal to 1, where $p$ ranges from 0 to $m$.

The fracture energy $\tilde{G}_{\text{c}}^{[m]}$ of a multiply-healed composite-like crack, which is a generalization of (5.10) for $m > 1$, corresponds to the weighted sum of the fracture energies of the phases $p = 0, \dots m - 1$ available before healing activation and the fracture energy of the latest formed healing material $p = m$, i.e.,

$$
\tilde{G}_{\text{c}}^{[m]} = \sum_{p=0}^{m} w^{[m](p)} G_{\text{c}}^{(p)}.
\tag{5.19}
$$

At the $m^{\text{th}}$ healing event, there are $m + 1$ material phases at a material point within the cohesive zone for which the tractions in each phase are governed by the corresponding cohesive relations. The shifts in the crack opening displacements are obtained for each phase such that the continuity of the tractions is maintained within each phase, similar to the equations for the shifts given by (5.12) and (5.15).

For subsequent use, the expressions for the volume fractions $w^{[m](p)}$ in the case of two healing events are obtained explicitly from (5.18) with $m = 2$, i.e.,

$$
\begin{aligned}
w^{[2](0)} &= w^{[1](0)}(1 - D^{[2](0)}) = (1 - D^{[1](0)})(1 - D^{[2](0)}), \\
w^{[2](1)} &= w^{[1](1)}(1 - D^{[2](1)}) = D^{[1](0)}(1 - D^{[2](1)}), \\
w^{[2](2)} &= w^{[1](0)} D^{[2](0)} + w^{[1](1)} D^{[2](1)} = (1 - D^{[1](0)}) D^{[2](0)} + D^{[1](0)} D^{[2](1)}.
\end{aligned}
\tag{5.20}
$$

**5**

The damage in the original material up to the first healing event is reflected in the value $D^{[1](0)}$ whereas the subsequent damage in the original material and the first healing material is accounted for, respectively, through the values $D^{[2](0)}$ and $D^{[2](1)}$. The corresponding composite traction and fracture energy after the second healing event can be computed from (5.17) and (5.19).

### 5.2.3. NUMERICAL IMPLEMENTATION

The cohesive crack healing model described above can be implemented in a finite element framework using cohesive elements (or using an XFEM approach). In the context of a finite element solution procedure performed using a Newton-Raphson iterative approach, the contribution of the cohesive elements to the global stiffness matrix is provided by their element-wise consistent tangent matrix, which corresponds to the derivative of the traction vector with respect to the crack opening displacement. With respect to a local coordinate system normal (n) and tangential (s) to the crack, the components of the tangent matrix are, in view of (5.17), given by the weighted constitutive (material) tangents of each phase $p$, i.e.,

$$\frac{\partial \tilde{t}_i^{[m]}}{\partial \delta_j} = \sum_{p=0}^{m} w^{[m](p)} \frac{\partial t_i^{(p)}}{\partial \delta_j}, \quad i = \text{n, s}, \quad j = \text{n, s}. \tag{5.21}$$

Correspondingly, the tangent matrix of the composite-like model requires the individual contributions from the phases. The expressions for the constitutive stiffness tangents depend on the loading-unloading conditions, as indicated in (5.3), applied separately for each phase $p$.

UNDER SOFTENING CONDITION:

For $f^{(p)} = 0$ and $\dot{\kappa}^{(p)} > 0$, the components of the consistent tangent matrix for the phase $p$ are obtained, assuming that $\Delta_i^{(p)} \ll \Delta_f^{(p)}$, from (5.4), (5.5), (5.11) and (5.13), as follows:

$$\frac{\partial t_n^{(p)}}{\partial \delta_n} = \sigma_c^{(p)} \left[ \frac{1}{\Delta^{(p)}} - \frac{1}{\Delta_f^{(p)}} - \frac{\left\langle \delta_n - \delta_n^{(p)*} \right\rangle^2}{(\Delta^{(p)})^3} \right],$$

$$\frac{\partial t_s^{(p)}}{\partial \delta_s} = \gamma^2 \sigma_c^{(p)} \left[ \frac{1}{\Delta^{(p)}} - \frac{1}{\Delta_f^{(p)}} - \frac{\gamma^2 \left( \delta_s - \delta_s^{(p)*} \right)^2}{(\Delta^{(p)})^3} \right],$$

$$\frac{\partial t_n^{(p)}}{\partial \delta_s} = \frac{\partial t_s^{(p)}}{\partial \delta_n} = -\frac{\gamma^2 \sigma_c^{(p)} \left\langle \delta_n - \delta_n^{(p)*} \right\rangle \left( \delta_s - \delta_s^{(p)*} \right)}{(\Delta^{(p)})^3}.$$

UNDER UNLOADING/RELOADING CONDITIONS

For $f^{(p)} < 0$ and $\dot{\kappa}^{(p)} = 0$, the components of the consistent tangent matrix are, assuming that $\Delta_\mathrm{i}^{(p)} \ll \Delta_\mathrm{f}^{(p)}$, given as

$$\frac{\partial t_\mathrm{n}^{(p)}}{\partial \delta_\mathrm{n}} = \sigma_\mathrm{c}^{(p)} \left[ \frac{1}{\kappa^{(p)}} - \frac{1}{\Delta_\mathrm{f}^{(p)}} \right] \, ,$$

$$\frac{\partial t_\mathrm{s}^{(p)}}{\partial \delta_\mathrm{s}} = \gamma^2 \sigma_\mathrm{c}^{(p)} \left[ \frac{1}{\kappa^{(p)}} - \frac{1}{\Delta_\mathrm{f}^{(p)}} \right] \, ,$$

$$\frac{\partial t_\mathrm{n}^{(p)}}{\partial \delta_\mathrm{s}} = \frac{\partial t_\mathrm{s}^{(p)}}{\partial \delta_\mathrm{n}} = 0 \, .$$

The case of the initial "elastic" behavior can in principle be treated formally as a reloading case by assigning an initial damage $\kappa_0^{(p)} = \Delta_\mathrm{i}^{(p)}$. However, since in the previous formulas the term $\Delta_\mathrm{i}^{(p)}$ has been neglected, the tangent matrix can be separately specified as

$$\frac{\partial t_\mathrm{n}^{(p)}}{\partial \delta_\mathrm{n}} = \frac{1}{\gamma^2} \frac{\partial t_\mathrm{s}^{(p)}}{\partial \delta_\mathrm{s}} = K \, ,$$

$$\frac{\partial t_\mathrm{n}^{(p)}}{\partial \delta_\mathrm{s}} = \frac{\partial t_\mathrm{s}^{(p)}}{\partial \delta_\mathrm{n}} = 0 \, ,$$

where $K$ is the cohesive stiffness, assumed in this case to be the same for all phases.

## 5.3. APPLICATION TO AN EXTRINSIC SELF-HEALING MATE-RIAL

In this section, the cohesive healing model is applied to a unit cell of an extrinsic self-healing material in which a single healing particle is embedded within a matrix material as shown in Fig. 5.2. In extrinsic systems, the particle contains a healing agent (i.e., the material contained inside the particle) that is normally protected by an encapsulation system to prevent premature activation of the healing process. The working principle of this system is that the healing mechanism is activated when a crack that propagates through the matrix interacts with the particle, usually breaking the encapsulation and allowing transport of the healing agent through the crack. Some self-healing system may involve auxiliary materials that are necessary for triggering and/or participating in a subsequent chemical reaction to create the final form of the healing material. The present simulation assumes that any additional substance required for the process is readily available in the matrix material (e.g., free oxygen transported by diffusion required for oxidation as found in self-healing thermal barrier coatings [STD+15]). Distinct cohesive relations can be used at different spatial locations (matrix, particle, matrix-particle interface), hence phase-specific fracture properties can be specified for the healing agent inside the particle
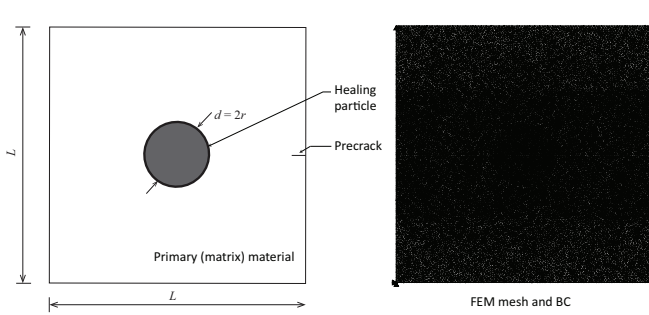
Figure 5.2: Geometry and finite element model of a unit cell of an extrinsic self-healing material. The unit cell is subjected to a nominal mode I loading. A small precrack is used to guide a matrix crack towards the particle. A layer of cohesive elements is placed to allow for crack propagation in a predefined direction given by the initial precrack.

and the healing material that appears in the cracks after activation of the healing mechanism.

As shown in Fig. 5.2, the unit cell used in the simulations is an $L \times L$ domain with a circular particle of a diameter $d = 2r$. For simplicity a two-dimensional computational domain under plane strain conditions is chosen, meaning that the particle should be interpreted as prismatic (fiber in the out-of-plane direction). Despite this interpretation, the model is assumed to be qualitatively representative of a spherical particle albeit with a different volume fraction. In the simulations the length is chosen as $L = 75\mu$m and the diameter as $d = 10\mu$m, which corresponds to a nominal (in-plane) particle volume fraction of 10%. In the finite element mesh, cohesive elements are inserted along a horizontal plane in the mid-height of the model, by which the crack is allowed to propagate along the pre-defined path. In principle, arbitrary crack growth can be modelled by inserting cohesive elements along all bulk elements in mesh, although that approach is not required for purposes of the present study [PTvdZ15]. The finite element mesh is sufficiently resolved so that proper discretization of the cohesive zone is ensured. Displacement-driven nominal mode I load is applied by specifying vertical displacements at the corner nodes on the right side of the domain while the corner nodes at the left are fixed as shown in the figure. Both the matrix and the healing particle are assumed to be isotropic and linearly elastic up to fracture. For the sake of simplicity, the material properties (both elastic and fracture) of the matrix and the healing particle are kept the same and the values are given as follows:

$$E^m = E^p = 150 \text{ GPa} , \ \nu^m = \nu^p = 0.25 ,$$
$$\sigma_c^m = \sigma_c^p = \sigma_c^{(0)} = 400 \text{ MPa} , \ G_c^m = G_c^p = G_c^{(0)} = 100 \text{ J/m}^2 ,$$

where $E$ and $\nu$ refer to Young's modulus and Poisson's ratio, respectively, and the superscripts m and p refer to the matrix and the particle, respectively. Since

the properties of the particle and the matrix are assumed to be equal, the original material, as indicated by the superscript 0, refers to either the particle or the matrix depending on location. The interface between the particle and the matrix is assumed to be perfectly bonded and interface fracture is taken not to occur. It is worth pointing out that in general the elastic and fracture properties of the healing particle and the matrix are different, which in fact decide whether a matrix crack would break the healing particle or not. This aspect of a matrix crack interacting with healing particles of different properties compared to the matrix is dealt in detail in [PTvdZ15] but is not relevant for the simulations presented in this section. Instead, the emphasis is placed here on how the crack healing behavior affects the recovery of mechanical properties of the material system. Further, as indicated above, the fracture properties of the healing particle in its initial state are in general different than the properties of the healing material that fills the cracks, which are specified separately as explained in the sequel.

Several parametric studies are conducted to evaluate the behavior of the unit cell and the results in terms of global load-displacement response are reported in the following subsections. In the first subsection, simulations are conducted to study the effect of variations in the fracture properties of the healing material. In the second subsection, a parametric study is performed to understand how does the available amount of healing agent affect the crack healing behavior. In the third subsection, multiple healing events are simulated and the resulting load-displacement response is reported.

### 5.3.1. EFFECT OF PROPERTIES OF HEALING MATERIAL AND HEALING CONDITIONS

The fracture properties of the healing material, formed as the result of the healing process, are often different from the surrounding host material. The fracture properties of the healed zone depend on the time available for healing and the properties of the healing product. A second aspect that is relevant for the healing process is the loading conditions during healing. Healing is a process that typically requires time to occur, and the efficiency of the process is often connected to providing a sufficiently long "rest time" in which the loading rate is zero and chemical reactions have sufficient time to be completed. However, even if a sufficient "rest time" is provided, the (constant) loading state influences the subsequent material response of the healed material. In this section, two representative loading states during healing are considered, namely healing under zero-stress (unloaded) conditions and healing under fixed applied displacement (constant load during healing). Different properties for the healing material are considered for each loading state during healing.

**5**

(a) Time history of the specified displacement.
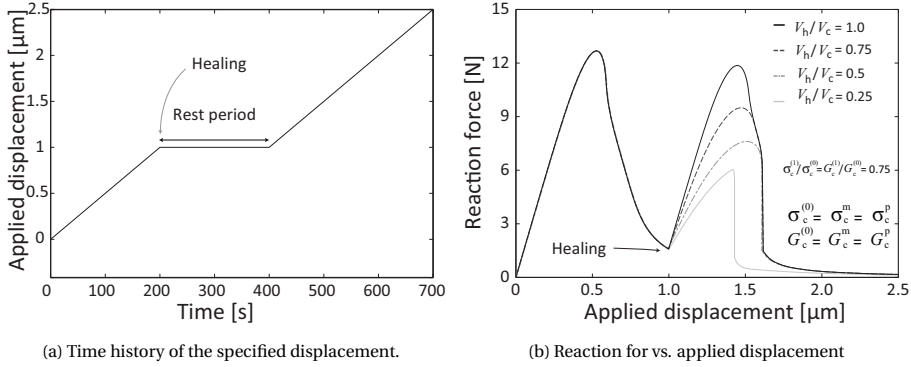


(b) Reaction force vs. applied displacement
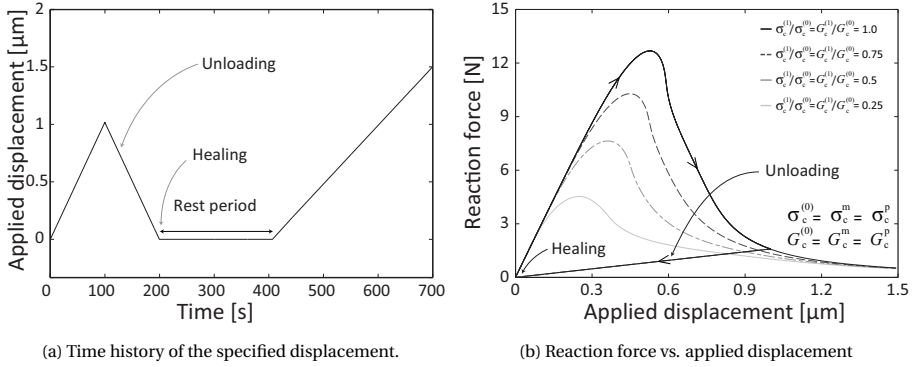
Figure 5.3: Healing under unloaded condition: applied loading to unit cell and reaction force as a function of applied displacement for various values of the fracture properties of the healed material.

### HEALING UNDER UNLOADED CONDITION

In the literature, most experimental studies deal with test protocols in which the sample is unloaded and allowed to return to its unstrained state, hence healing occurs under unloaded conditions [KSW03, BSW02, WTB07, PB05, SPS$^+$08]. In order to analyze the predictions of the model under similar conditions, the unit cell shown in Fig. 5.2 is subjected to a loading and healing sequence as indicated in Fig. 5.3a. Under this loading, the specimen is partially fractured and then unloaded. Healing is allowed to occur in the unloaded condition, which is then followed by reloading of the healed specimen. The response of the unit cell in terms of the applied vertical displacement and the corresponding reaction force is shown in Fig. 5.3b for various fracture properties of the healing material, namely $\sigma_c^{(1)}/\sigma_c^{(0)}$, $G_c^{(1)}/G_c^{(0)}$ = 0.25, 0.5, 0.75 and 1, where the superscript 1 refers to the healing material. As shown in Fig. 5.3b, the curve corresponding to equal properties of the healing and original material predicts a recovery of the response after healing similar to that of the original material. The next three curves correspond to lower values of the fracture properties of the healing material and hence the load-displacement curves fall below that of the original material after healing.

It is to be mentioned that, after healing, recracking occurs along the same path as the initial crack. This is due to the fact the fracture properties of the healing material are lower than or at least equal to that of the original material properties. Nonetheless, if the properties of the healing material are higher than that of the original material, the crack would propagate along a different path which is weaker than the healed zone. However, the recovered load-displacement response would be similar to the one with the same fracture properties, as the crack is traversing along the original material.

(a) Time history of the specified displacement.

(b) Reaction force vs. applied displacement
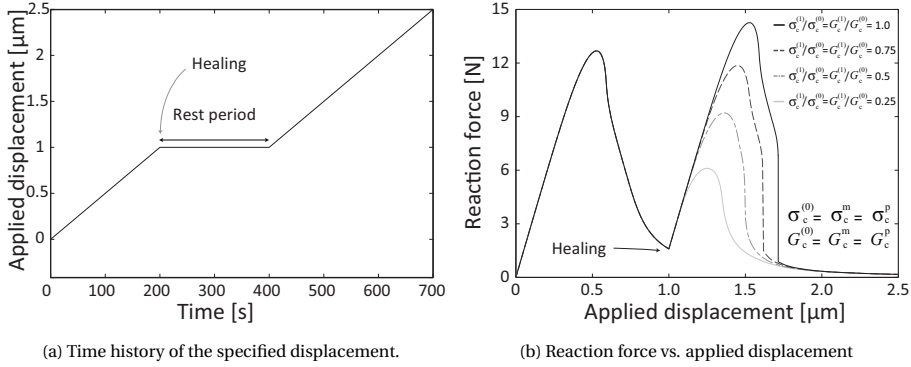
Figure 5.4: Healing under constant loading condition: applied loading to unit cell and reaction force as a function of applied displacement for various values of the fracture properties of the healed material.

## Healing under constant load condition

In situations of practical interest, healing may occur under a non-zero load, which implies that the crack opening is non-zero as the healing material fills the crack gap. To study the effect of the loading state during healing on the post-healing response of the material, simulations are carried out according to the loading sequence shown in Fig. 5.4a. In this case, the specimen is (partially) fractured, allowed to heal at a constant applied displacement and subsequently reloaded. As in the previous case (healing at unloaded conditions), four different fracture properties of the healing material are considered, given by the strength and fracture energy ratios $\sigma_c^{(1)}/\sigma_c^{(0)}$, $G_c^{(1)}/G_c^{(0)} = 0.25$, 0.5, 0.75 and 1. The load carrying capability of the healed specimens is shown in Fig. 5.4b, which indicates the reaction force of the unit cell as a function of the applied vertical displacement.

For each set of material properties of the healing material, the state of the specimen is the same prior to healing. After healing at a constant crack opening profile, the specimen recovers its load-carrying capability as shown in Fig. 5.4a. It can be observed that the post-healing force peak is higher than the force peak of the original material for the case when the healing material has the same fracture properties of the original material. This result is partly due to the equal strain kinematic assumption of the Voigt-like composite model, as indicated in Sec. 5.2.2.1, which tends to overpredict the force response. It is anticipated that a more complex composite model, which preserves both linear momentum and kinematic compatibility, would predict a lower post-healing peak. Although the present model provides an upper estimate of the post-healed behavior, it allows to compare the effect of the state of the material during healing on the post-healing behavior. In particular, the post-healing failure in the case of healing under loaded conditions is more sudden
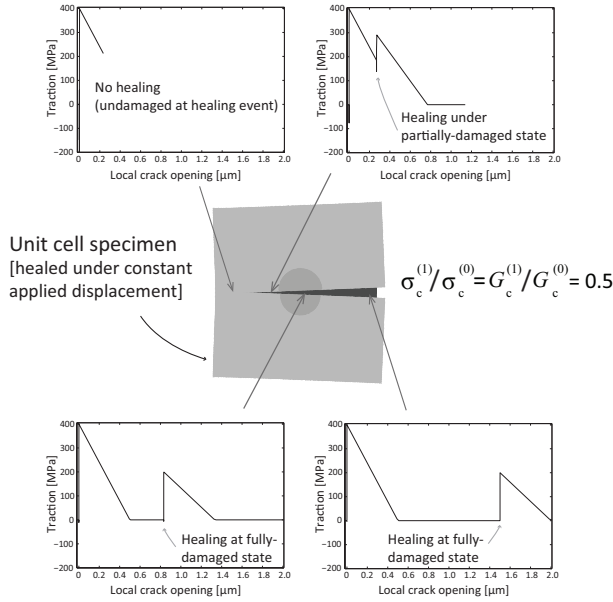
Figure 5.5: Unit cell specimen at the final state of the applied loading given in Fig. 5.4a. Representative local response curves illustrate how the introduction of a shift in the (local) crack opening displacement accounts for the proper origin upon resumption of the load after healing.

(i.e., qualitatively more brittle, see Fig. 5.4b) compared to the case of healing at an unloaded state (see Fig. 5.4b), except when the properties of the healing material are relatively low.

To gain more insight in the healing process under constant crack opening profile, the local response curves at selected locations are shown in Fig. 5.5 for the case when the properties of the healing material are $\sigma_c^{(1)}/\sigma_c^{(0)} = G_c^{(1)}/G_c^{(0)} = 0.5$. As can be observed in the figure, the crack openings at the instant of healing depend on location, with increasing values towards the side where the opening load is applied. Observe that some points undergo healing from a fully-failed state, some from a partially-failed state and some points that are cracked at the end of the loading process experienced no healing since they had not failed at the instant at which healing was activated.

After healing, the effective crack opening displacements become zero in the healed zone due to the displacement shifts introduced in the model to account for crack filling. However, modelling of the crack gap filling and healing is only done implicitly through the shift in crack opening displacements, whereby the new material is not explicitly modelled as an additional material (or mass) entering the system.

(a) Time history of the specified displacement.



(b) Reaction for vs. applied displacement

Figure 5.6: Effect of filling efficiency: applied loading to unit cell and reaction force as a function of applied displacement for various values of healed areas

## 5.3.2. DEGREE OF CRACK FILLING AND HEALING

In the previous subsection, it was assumed that the healing particle, upon fracture, releases an amount of healing agent (denoted as $V_h$) that is sufficient for complete filling of the crack opening volume (or crack opening area in two dimension, denoted as $V_c$). However, depending on the amount of available healing material, the geometrical characteristics of the crack and the mode of transport, it may occur that the crack is only partially filled, which is a key factor affecting the healing characteristics and hence the recovery of mechanical properties. In this section, the effect of the ratio $V_h/V_c$ of healing agent available to the required healing agent for complete filling is studied. Here, the volume of required healing agent for complete crack filling refers to the total crack volume at the instance of healing activation. The ratio considered is generic and its interpretation in a specific self-healing material system requires understanding of its healing characteristics. For instance, the amount of healing material produced as the result of the healing process is directly related not only to the volume of the healing particle, but also the reaction kinetics of the healing process. For example, in one of the extrinsic self-healing systems reported in the literature, the healing agent within the particle produces healing material through increase in volume by oxidation under high temperature conditions [STD+15, PTvdZ15]. Hence, the term $V_h$ means here the volume of the healing product formed as the result of the healing process, which is used for healing the crack. The notion of complete or partial filling, measured by the ration $V_h/V_c$, refers to the amount of crack gap filled with healing material regardless of the fracture properties of the healing material.

Simulations are conducted for four different healing processes with filling efficiencies of $V_h/V_c = 1$, 0.75, 0.5 and 0.25. In all cases the properties of the healing
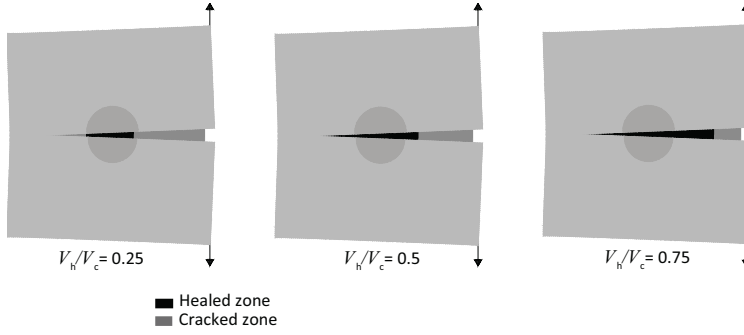
Figure 5.7: Specimen showing the healed cohesive cracks for various degrees of crack filling. For the purpose of clarity, the deformed specimen has a scaling factor of 3

material are taken as $\sigma_c^{(1)}/\sigma_c^{(0)}$, $G_c^{(1)}/G_c^{(0)} = 0.75$. The specimens are loaded according to the sequence indicated in Fig. 5.6a and the corresponding force-displacement curves are shown in Fig. 5.6b. To interpret the results for partial filling, it is useful to indicate the spatial location where healing occurs, which is shown in Fig. 5.7. As indicated in the figure, filling is assumed to take place in the zone adjacent to the healing particle.

The curve shown in Fig. 5.6b corresponding to a complete filling (filling ratio $V_h/V_c = 1$) represents the highest possible recovery of the load-carrying capability for the given fracture properties of the healing material. As expected, the recovery of the load-carrying capability decreases with decreasing filling ratios $V_h/V_c = 0.75, 0.5, 0.25$. One relevant difference between the effect of a decrease in filling efficiency and a decrease in the fracture properties of the healing material for a fixed filling efficiency is that in the latter case the initial slope of the post-healed behavior remains the same for distinct fracture properties whereas in the former case the initial slope decreases with decreasing filling efficiency (compare Fig. 5.4b and Fig. 5.6b). In the simulations shown in Fig. 5.6b, the initial post-healing slope reflects the increase in compliance due to purely geometrical effects. The un-healed portion of the crack facilitates the (elastic) deformation of the specimen. This effect may potentially be used in the interpretation of experimental curves as an indication of partial filling of a crack.

### 5.3.3. MULTIPLE HEALING EVENTS

Some materials with intrinsic self-healing capacity (such as MAX phases), may undergo multiple healing events whereby a crack is healed on multiple occasions [LSK+12, SPM+16]. In extrinsic systems, multiple healing may occur in cases where there is an external supply of healing material, but also in particle-based systems when inactivated particles (or portions of partially activated particles) can still supply healing material for an additional healing event . In this section, it is assumed that the particle in the unit cell shown in Fig. 5.2 is capable of providing sufficient

(a) Time history of the specified displacement.



(b) Reaction for vs. applied displacement
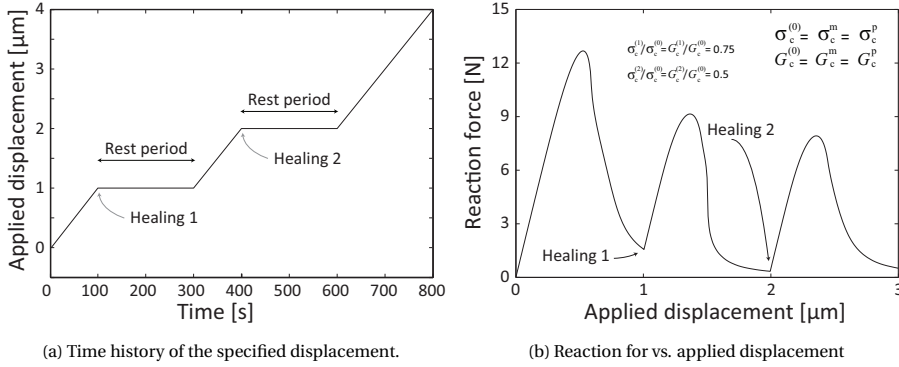
Figure 5.8: Effect of multiple healing: applied loading to unit cell and reaction force as a function of applied displacement for two healing events

healing material for two healing events. The specimen is subjected to a loading and healing process as shown in Fig. 5.8a. The ratio of crack opening volume (or area) to the available healing material volume is assumed to be 1 for both healing events, resulting in complete filling of the crack. The fracture properties of the healing material after the first healing event are taken as 75% of those of the original material, while for the second healing event, the properties are taken as 50% of that of the original material, hence $\sigma_c^{(1)}/\sigma_c^{(0)}$, $G_c^{(1)}/G_c^{(0)} = 0.75$ and $\sigma_c^{(2)}/\sigma_c^{(0)}$, $G_c^{(2)}/G_c^{(0)} = 0.5$. This assumption is meant to implicitly represent a degradation on the quality of the healing material after the first healing event.

The reaction force on the unit cell is shown in Fig.5.8b as a function of the applied vertical displacement. As can be observed in the figure, the load carrying capacity may be (partially) recovered multiple times provided that the self-healing mechanism supplies sufficient healing material for multiple healing events. Although a single healing event can naturally extend the lifetime of a material, a more significant extension can be achieved in a material capable of multiple self healing repairs, even if the quality of the healing material degrades during subsequent healing events. The model developed here may be used for design purposes to optimize the characteristics of a healing particle and/or a cluster of healing particles by further investigating convenient particle characteristics or particle arrangements that provide the capacity of multiple healing events. This may be achieved by, for example, embedding particles large enough to serve as a reservoir for multiple healing events or by placing a cluster of particles that may be activated sequentially as cracks reappear in a material at adjacent locations. Although those studies are beyond the scope of the current work, the present model may be employed to simulate the recovery of strength and fracture energy under complex loading histories.

## **5.4.** SUMMARY AND OUTLOOK

A cohesive zone-based computational framework for analyzing self-healing materials is presented to model the recovery of mechanical properties. Salient features of the composite model are demonstrated through several test simulations. In particular, the capability of the model to simulate multiple healing events and handling different fracture properties of the healing material for each healing event is relevant for analyzing several realistic self-healing materials. The model can be applied for either extrinsic or intrinsic self-healing material systems with an appropriate coupling to healing kinetics in each case.

For a unit cell of an extrinsic self healing material, the simulations show that the recovery of the load carrying capacity upon healing depends both on the fracture properties of the healing material that fills the cracks as well as the filling efficiency, which may be seen as a geometrical characteristic. Further, it is found that the post-healed behavior of a material healed under loaded conditions appears to be more brittle than for a material healed under unloaded conditions, although this conclusion is based on the assumption that the healing material has the same fracture properties in both cases, which may not be necessarily the case in some self-healing materials. The simulations also indicate that the characteristics of the initial post-healing response in a force-displacement diagram may be used as an indicator of the filling efficiency of a healing event whereby an initial response similar to that of the original material corresponds to maximum crack filling efficiency regardless of the fracture properties of the healing material. A decrease in the initial post-healing force-displacement slope compared to the initial slope of the original material is an indication of an incomplete filling process, again regardless of the fracture properties of the healing material.

The developed framework does not explicitly model the crack healing kinetics, rather the results of the healing process are provided as input parameters to the model. Nonetheless, the coupling of crack healing kinetics into the model is in principle straightforward in the form of the amount of healing material produced as the result of the healing process, which is then geometrically related to the crack volume healed. For modelling purposes, it is also possible to treat the properties of the healing material as a variable during multiple healing events to implicitly account for a continuous degradation in the healing quality. In general, the model may be used for designing new self-healing material systems with the capacity of undergoing multiple healing events and, correspondingly, extending significantly the lifetime of a material with minimal external intervention.

# 6

# THERMAL CYCLIC BEHAVIOR AND LIFE TIME PREDICTION OF SELF HEALING THERMAL BARRIER COATINGS

The thermal cyclic behavior of self healing thermal barrier coatings (TBC) is analyzed using the finite element method to develop a life prediction model. To this end, a unit cell based multiscale modelling approach is adopted along with a simplified TGO growth model to study the evolution of cracking and healing.. The fracture and healing process is modelled using the cohesive zone-based healing model along with the crack tracking algorithm. Both the horizontal splat boundaries and TC/BC interface are represented as a sinusoidal curve with its representative amplitude and frequency. Simulations are carried out on a self healing TBC model with random distribution of healing particles subjected to a numerically accelerated thermal cyclic loading condition. Lifetime extension of the self healing TBCs is quantified by conducting the thermal cyclic analysis on conventional (benchmark) TBCs. Parametric analysis on healing parameters such as crack filling ratio and strength recovery of the healed crack are also conducted. The results are presented in terms of crack pattern and number of cycles to failure. It is found that for self healing TBCs with a suitable healing reaction (i.e., cracks being partially filled and a minimal local strength after healing) results in a improved TBC lifetime. In contrast, if the healing mechanism is not activated, the presence of the healing particles is actually detrimental to the lifetime of the TBC. This highlights the importance of a robust activation mechanism for self-healing. In addition to superior crack filling ratio and

healed strength, significant improvement in lifetime is achieved for self healing TBCs
with a higher probability of crack-healing particle interaction.

## 6.1. INTRODUCTION

In this chapter of the thesis, different modelling ingredients developed and discussed
in the previous chapters are combined together to obtain a simulation framework for
analysing the lifetime (i.e, the number of cycles to coating debonding) of the TBC
systems with or without healing particles. In particular, the enhancement in the
lifetime of the self-healing TBC system is quantified and compared with the lifetime
of a conventional TBC system. The simulation framework involves integrating the
following four key modelling aspects

- Setting up a multiscale model of the self-healing TBC with randomly dis-
  tributed healing particles

- Implementation of a model to mimic the TGO layer growth and its associated
  internal stress generation.

- Incorporating the developed cohesive crack healing model with multiple crack-
  ing and healing events

- An efficient crack tracking algorithm which deals with activation of healing
  mechanism and tracks the local history of cracking and healing events.

With the above integrated simulation tool, the objective to conduct thermal cycling
simulations is to evaluate the effects of key parameters such as the distribution of
healing particles, crack filling ratio and properties of healed material phase on the
lifetime of the self-healing TBC system.

In the context of extrinsic self-healing TBCs, most of literature studies are majorly
focussed on understanding the material requirements, oxidation behaviour, depo-
sition and fabrication process of the self-healing TBC [vdZB15, DCS$^+$15, KMZC$^+$16,
NEC$^+$18, CvdZS15, CMB$^+$18, KPTvdZ18, PKTvdZ19]. For instance, types of encap-
sulation process of the healing particles to avoid premature oxidation are discussed
in [CvdZS15, CMB$^+$18]. The effect of mismatch in thermo-mechanical properties on
fracture behavior of self healing TBCs is studied in [KPTvdZ18]. In [PKTvdZ19], the
mechanical behavior of $MoSi_2$/YSZ composite is investigated using finite element
analysis and the influence of healing particle on the overall mechanical performance
is quantified.

On the experimental side, several studies addressed the behaviour of self-healing
TBC systems from various viewpoints [STD$^+$15, NEC$^+$18, NME16, CZvdZ$^+$19]. For
instance, cracking and healing behavior of the TBC coating with healing particles
($MoSi_2$(B)) is studied experimentally in [CZvdZ$^+$19]. The characteristics of the
healing particles for successful healing activation and efficient healing have also been

discussed. Thermal cycling and oxidative behavior of $MoSi_2$/YSZ self healing TBCs produced by spark plasma sintering (SPS) are studied in [NME16, NEC+18].

It is obvious from the literature that, obtaining an efficient self-healing TBC design is difficult due to the various (non-linearly) interacting factors. Further an experiment-driven iterative design process is often time-consuming and expensive. In this regard, there exists a demand to have a tool that can simulate the cracking and healing behaviour of the TBC system, which in turn can be used to achieve an optimal configuration of self-healing TBC. This chapter aims to close such a gap and develops a simulation tool for determining the TBC lifetime and its enhancement due to healing particles.

## 6.2. MODELLING AND SIMULATION SETUP

### 6.2.1. SELF HEALING TBC MODEL

The self healing TBC modelling setup considered in this work is shown in Fig. 6.1. A unit cell based multiscale model is developed in a two-dimensional framework under plane strain condition. The substrate is not modelled explicitly and its effect is enforced through periodic displacement boundary conditions at the right (R) and left(L) edge of the TBC as.

$$
\begin{aligned}
u_x^R - u_x^L &= (1 + v_s)\alpha_s \Delta T W, \\
u_y^R - u_y^L &= 0,
\end{aligned}
\tag{6.1}
$$

where $v_s$ and $\alpha_s$ correspond to Poisson's ratio and the thermal expansion coefficient of the substrate, respectively. The displacement boundary condition at the bottom edge (B) of the TBC unit cell is given by (6.2)

$$
\begin{aligned}
u_x^B &= (1 + v_s)\alpha_s \Delta T x, \\
u_y^B &= 0,
\end{aligned}
\tag{6.2}
$$

For simplicity, the morphology of the TC/BC interface and the splat boundaries are considered to be sinusoidal and it is given by .

$$
y_n(x) = nh + A\cos(x\pi/60)
$$

$$
A = \begin{cases} 20\mu m & \text{if} \quad n = 0, \\ 8\mu m & \text{if} \quad n > 0, \end{cases}
\tag{6.3}
$$

where subscript $n = 0$ refers to the TC/BC interface and $n > 0$ corresponds to the splat boundaries. The spacing between the splat boundaries ($h$) is assumed to be constant with value of 15 $\mu$m. The thickness of the TC and the BC layer are given by $h_{TC}$ = 500 $\mu$m and $h_{BC}$ = 200 $\mu$m respectively. The periodic unit cell is modelled with the appropriate width of $W = 480\mu$m. The healing particles are distributed randomly but

relatively close to the TC/BC interface where the cracks are likely to occur. The TC region where the healing particles are distributed is called the healing layer ($h_L$) with the thickness of 200$\mu$m. The volume fraction and healing particle diameter are fixed with values of 5% and 10 $\mu$m, respectively.

The self healing TBC model is meshed with three noded plane strain triangular element (CPE3). Cohesive elements are inserted in all the inter element boundaries to enable arbitary initiation and propagation of cracks. The fracture and healing behavior in the TC layer is modelled through the cohesive zone-based healing model developed in chapter 5. The domain considered is discretized with a fine mesh close to the TC/BC interface (with a characteristic element size of 1 $\mu$m to predict the converged crack pattern whereas the remaining regions are discretized with a coarser mesh (with a characteristic element size of 2 $\mu$m to reduce the computational cost. More details about the geometry, loading condition and finite element mesh are explained in chapter 4.
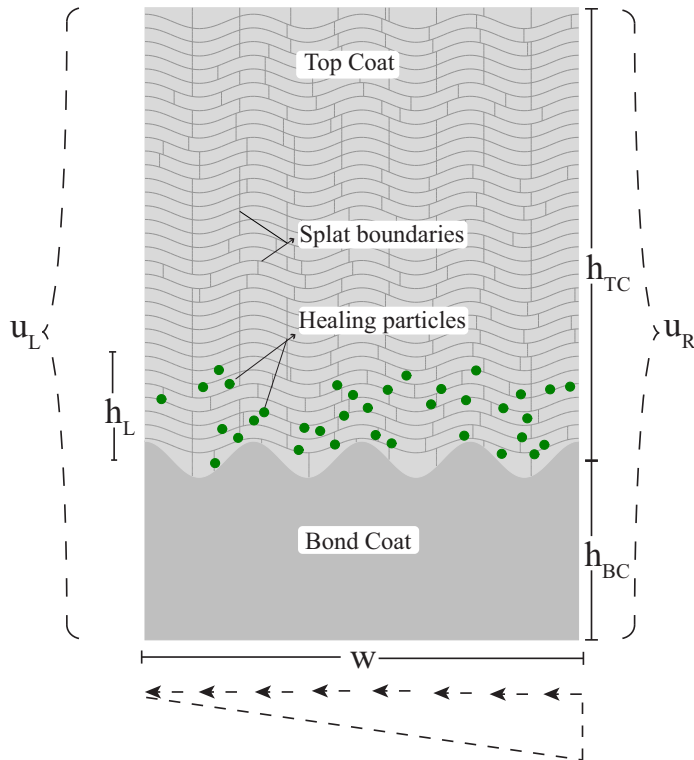


Figure 6.1: Multiscale finite element model of self healing TBC system

### 6.2.2. MATERIAL PARAMETERS

The material parameters of the self healing TBC components are summarized in Table 6.1. Linearly elastic and isotropic material behavior is assumed for all the components. A bi-linear cohesive law is used to model the TBC fracture behavior. The material properties listed in Table 6.1 are equal to the values considered in earlier chapters. The ratio of fracture properties of healed material to the fracture properties of the TC layer is arbitrarily set to 0.75, where this value is taken to represent a healing system with relatively good healing properties but below the pristine material.

Table 6.1: Elastic and fracture material parameters of the self healing TBC components.

| Layers | $E$ (GPa) | $\nu$ | $\alpha$ ($10^{-6}$ 1/°C) | $\sigma_n$ (MPa) | $G_{IC}$ (N/mm) | $\gamma$ |
|---|---|---|---|---|---|---|
| Top coat | 80 | 0.15 | 12.5 | 150 | 0.006 | 4 |
| Bond coat | 130 | 0.3 | 14.5 | 500 | 0.3 | 1 |
| Healing particle | 300 | 0.22 | 9.4 | 200 | 0.16 | 4 |
| TGO | 380 | 0.15 | 7 | 380 | 0.04 | 4 |
| Splat interface | - | - | - | 75 | 0.002 | 4 |
| Substrate | 200 | 0.28 | - | - | - | - |

### 6.2.3. IMPLEMENTATION OF TGO GROWTH

A simplified TGO growth model is implemented in the FEM program Abaqus using the UMAT (user material) subroutine to simulate the TGO evolution with respect to the number of thermal cycles. The model derives its input through experimentally determined growth kinetics, which provides the time history of the TGO thickness evolution (thickness with respect to oxidation time). Two aspects were considered in the TGO growth model. Firstly, the increase in TGO thickness that is modelled by incrementally replacing the BC layer with TGO material. In this model, the TGO is assumed to grow only in the inward direction, i.e., into the bond coat layer. Further, it is assumed that the TGO growth is limited to the dwell phase only. In terms of implementation, the UMAT subroutine will change the thermal and mechanical properties of the BC with the number of thermal cycles using experimentally measured TGO thickness ($h_{tgo}$) values. For the present work, the TGO growth curve [SYZ$^+$17, BHT$^+$08] under isothermal oxidation condition at 1050°C is used to define the $h_{tgo}$. The second aspect in the TGO modelling is to incorporate additional strains associated with the volume changes induced by the TGO growth. As the growth process is considered to be volumetric, a hydrostatic strain component [HTS11] is added to the thermoelastic strain field at the phase changed material points in the TBC. A relatively small isotropic TGO growth strain of $\epsilon_g = 1\text{x}10^{-4}$ is assumed, which is estimated based on residual stresses

Because of the modelling approach, a mixture zone, which is a combination of both BC and TGO material phases, appears during the cycling process in the

simulations. Inside this mixture zone, the constitutive properties in the growth model are represented as the weighted average of constitutive parameters of the BC and TGO layer as follows:

$$\mathbb{C} = \gamma \mathbb{C}_{tgo} + (1 - \gamma)\mathbb{C}_{bc}$$

$$\gamma = \begin{cases} 0 & \text{if} \quad d_c \geq (h_{tgo} + e_s), \\ 1 & \text{if} \quad d_c \leq h_{tgo}, \\ \frac{d_c - h_{tgo}}{d_c} & \text{if} \quad h_{tgo} < d_c < (h_{tgo} + e_s) \end{cases} \quad (6.4)$$

where $\mathbb{C}$ represents the effective mechanical and thermal parameters defined in the TGO growth model. The parameter $\gamma$ gives the volume fraction of TGO at the given material point. For the numerical implementation in a FEM mesh, the value of $\gamma$ is governed by current TGO thickness($h_{tgo}$), the element size ($e_s$) and the distance between the TC/BC interface and the element centroid ($d_c$).

### 6.2.4. CRACK TRACKING ALGORITHM

As previously discussed, the essential condition for a successful healing activation is that the crack needs to open a healing particle. In other words, only those cracks that interact with healing particles are healed. To model this condition in the computational framework it is necessary to have a real-time tracking algorithm for crack initiation and crack growth. In the current simulation set up, the crack tracking algorithm is implemented using an Abaqus-based Python script. The implementation procedure is explained in Appendix B. The script is executed at the end of each heating phase using the Abaqus user subroutine URDFIL.

### 6.2.5. VIRTUAL ACCELERATED THERMAL CYCLING

A typical thermal cycle consist of three distinct loading phases (see Fig.6.2); a heating phase of $\Delta T = 1070°C$ (heating from 30°C to 1100°C) followed by a dwell phase $\Delta T = 0$ for 1 hour and a cooling phase of $\Delta T = -1070°C$ (cooling down from 1100°C to 30°C). Since, the growth of TGO and crack healing process occurs only at high temperature, these processes are limited to the dwell phase of the thermal cycle. Thermal cyclic loading and the associated TGO thickness are shown in Fig. 6.2. Further,the TBC system is assumed to be stress free at the initial heating and dwell phases as these coatings are deposited under high temperature. Thermal cycling simulations are carried out under uniform temperature distribution and explicit modelling of the thermal cycles (fatigue loading). It is important to consider that the model deals with thermally homogeneous steady state conditions and effects of heating rate and dwell time (other than controlling TGO growth step) are not included.

The average lifetime of the TBCs is several hundred cycles, therefore it is computationally expensive to simulate the failure behavior of TBC (cracking and/or healing)
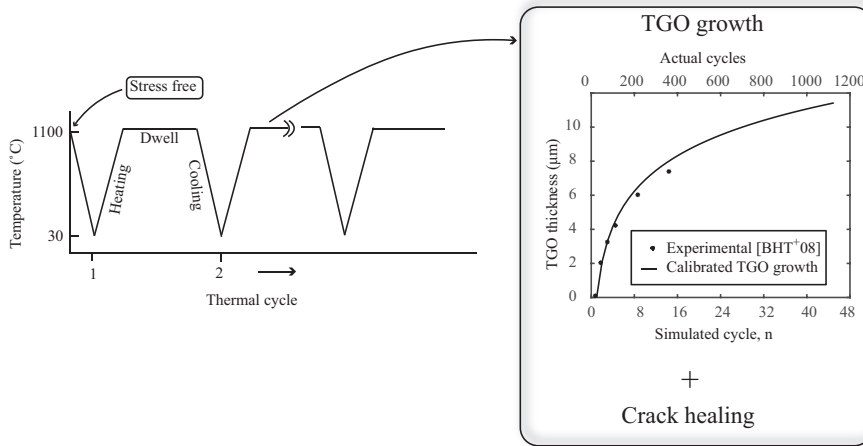
Figure 6.2: Thermal cyclic loading condition

for all the loading cycles. Hence, to reduce the computational time, lifetime analysis is performed under accelerated loading condition with each simulated thermal cycle represents several experimental loading cycles (see Fig. 6.2). The analysis procedure is explained in the flow chart as shown in Fig. 6.3.

## 6.3. RESULTS AND DISCUSSION

Thermal cyclic behavior of self healing TBCs is analyzed and the results are discussed in terms of the fracture pattern and number of cycles to failure (defined as complete delamination). Two sets of analyses are considered for this study. In the first set, simulations are carried out to quantify the extension in lifetime of self healing TBCs compared to the conventional TBCs. Further, the effect of healing particle distribution on lifetime of self healing TBC are also studied. The second set of simulations corresponds to the parametric analysis where the influence of healing parameters on fracture behavior and lifetime of self healing TBCs are analyzed. The cohesive element is assumed to be cracked if it dissipates 10% of its fracture energy. Complete failure of the TBC is defined when 90% of the TC layer detached is from the TGO/BC layer.

### 6.3.1. LIFETIME EXTENSION OF SELFHEALING TBC

Thermal cycling simulations are conducted for five different realisations (ranging from R1 to R5) of self-healing TBC system according to the analysis procedure discussed in the previous section. The volume fraction of the healing particles in the TC layer is fixed at 5% and the particles are randomly distributed in the proximity of the TC/BC interface as discussed in Sec. 6.2.1. The tensile strength and fracture
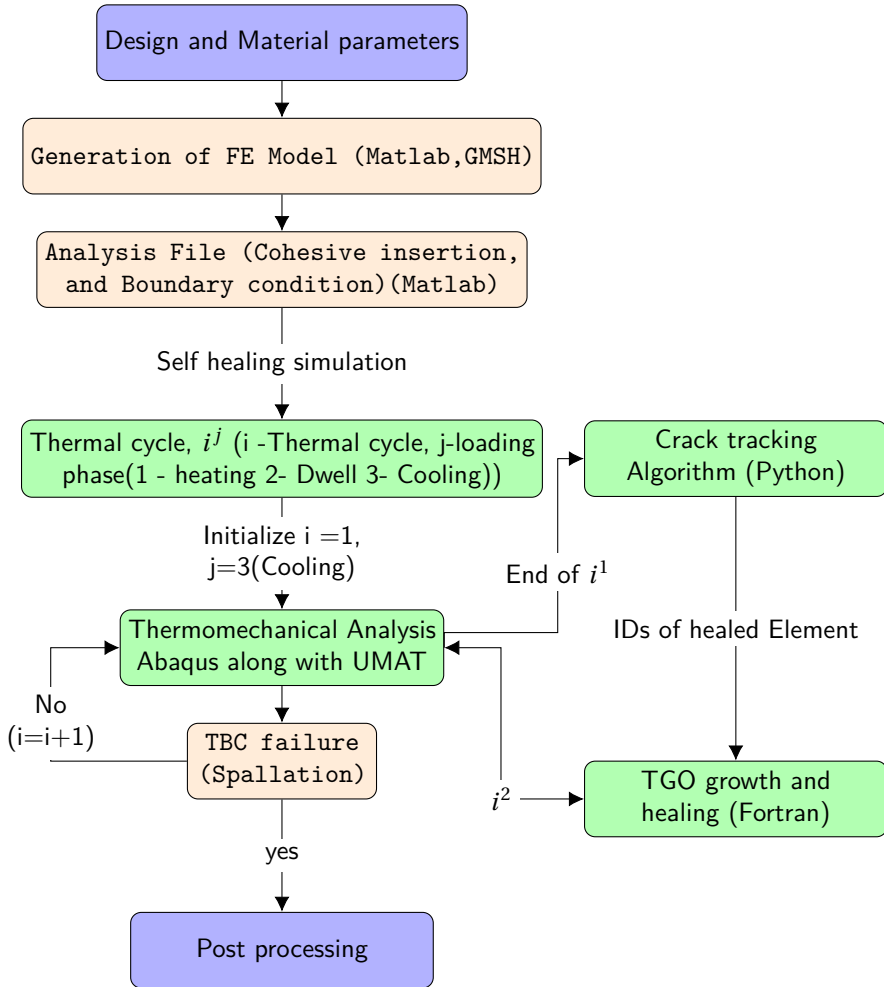
Figure 6.3: Overall simulation procedure for self healing TBC system

energy of the healing material are fixed with the values given by $\sigma_n$ = 112.5 MPa and $G_{IC}$ = 4.5x10$^{-3}$ N/mm. The final failure state of all the TBC realisations are shown in Fig. 6.4 along with the number of thermal cycles required to reach the failure state. In order to quantify the lifetime extension of the self-healing TBC, thermal cycling simulations are conducted for a conventional TBC without healing particles. The final failure patterns and the lifetime of such benchmark TBC are also shown in Fig. 6.4 for comparison. For obvious reason, only one realisation was considered for the conventional TBC without healing particles. The parts of the cracks shown in red

and blue colors correspond to unhealed and healed states respectively.
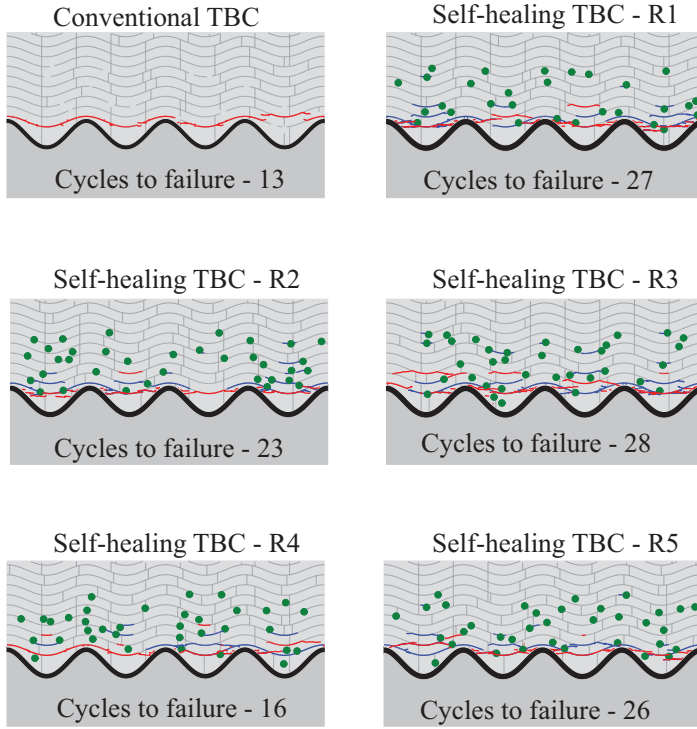


Figure 6.4: Final failure state along with number of cycles to failure of self healing TBC system for five different realisation of the healing particle.

From the results shown in Fig. 6.4, it is clear that, for all the realisations, introducing healing particles extends the number of cycles needed for complete failure when compared with results for the conventional TBC. For the considered five self-healing TBC systems or realisations, the cycles to failure are obtained as 27, 23, 28, 16, 26 as opposed to 13 obtained for the conventional TBC system. It is natural that each realisation of the self-healing TBC results in different lifetime characteristic (cycles to failure), which pertains to the random distribution of the healing particles in each of the five realisations. For instance, the least enhancement in lifetime is observed for the self-healing TBC realisation R4 as compared with the rest of the realisations. This can be attributed to the fact that the interaction between the microcracks and the healing particles are minimal in R4 due to the way in which the healing particles are distributed. Thus, the lifetime extension is dependent on the spatial distribution of healing particles and not just on the amount of healing particles present in the TBC system as measured by the volume fraction.

A complete statistical characterization requires a large number of simulations, which is currently computationally prohibitive, hence the analysis is limited to a relatively small number of realizations.
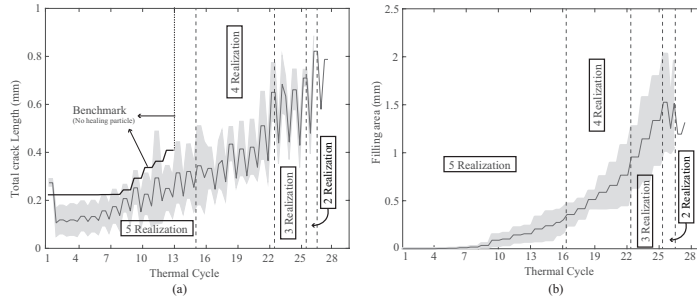


Figure 6.5: Statistical variation of total crack length and crack filling area with the thermal cycles for five different realisation of the self healing TBC system

For better understanding, the results of the simulations for all the realizations and the benchmark case are summarised in Fig. 6.5 in terms of crack evolution history and crack filling area with respect to the number of thermal cycles. It is interesting to note that, upon the completion of the first thermal cycle, microcracks of equivalent length of around 0.2 mm are observed for the benchmark case. This cracking is attributed to the CTE mismatch between the TC and BC layers and their wavy interface. However, with subsequent cycling, these cracks do not evolve further until the TGO growth starts to influence the stress field and cracking process. For instance, for the benchmark TBC, the crack starts to grow only after 7 thermal cycles. After which, the TGO growth process in combination with thermal mismatch drives a phase of gradual crack evolution as seen in Fig. 6.5.a, following which a sudden failure occurs at around 13 cycles, defining the lifetime of the benchmark TBC considered. The crack evolution histories are also plotted for the self-healing TBC systems in Fig. 6.5.a. One interesting feature is that, in self-healing TBCs, the equivalent (or total) length of the microcracks after the first thermal cycle is always higher than that of the benchmark TBC without healing particles. This is expected as the presence of healing particles induces additional stress concentrations that lead to microcracking around the particles, resulting in an increased total length of the microcracks. However, unlike the benchmark TBC, the microcracks start interacting with the healing particles in the self-healing TBCs, resulting in healing and thus reducing the total crack length in the next cycles as can be seen in the figure. Similar to the benchmark TBC, the crack length does not increase further up to a certain number of cycles, after which, it starts to increase due to the additional stresses induced by the TGO growth. It is also worth noting that, not only the lifetime (cycles to failure) of the self-healing TBC is higher, but also the rate of crack evolution is lower in the case of self-healing TBC when compared with the benchmark TBC system.

Such a decelerated crack growth and enhanced lifetime are the direct effects of the crack healing events happening throughout the thermal cycling process. For the considered realisations of the self-healing TBCs, the average extension in the lifetime is about 85%. In Fig. 6.5.b, the crack filling area is also shown, which indicates the history of the degree of healing with the thermal cycling.
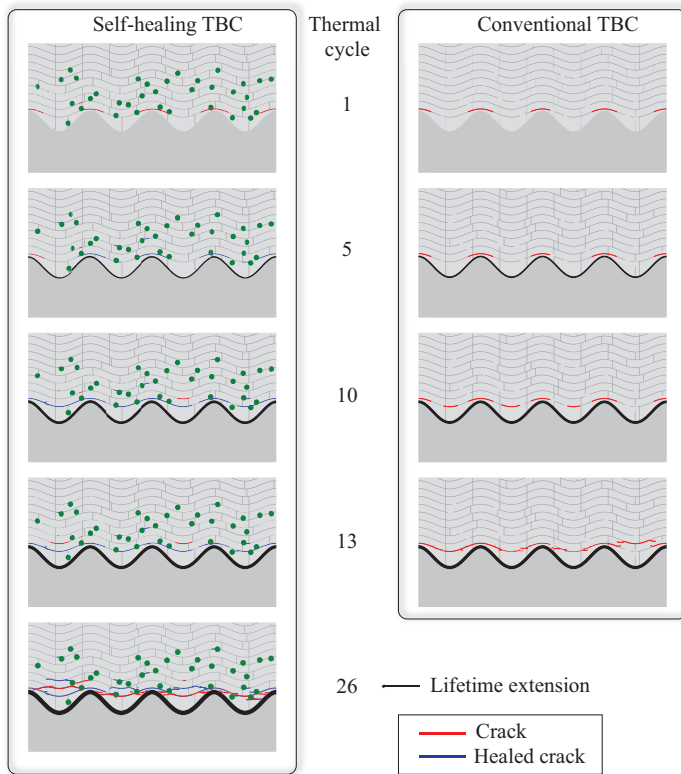


Figure 6.6: Evolution of fracture state of self healing and conventional TBC system at different thermal cycles

In each of the thermal cycling simulations conducted for five realisations, it is important to highlight that multiple healing events occurred during the cycling process. This situation is illustrated for one realisation of the self-healing TBC and the benchmark TBC as shown in Fig. 6.6. In the figure, it can be observed that the failure evolution involves not just cracking and healing, but also multiple recracking and healing events.

### 6.3.2. PARAMETRIC SIMULATION

Parametric simulations are carried out to study the effect of healing parameters such as the length of crack filled by the healing particle and the strength of the healed material on lifetime of self healing TBCs. These parameters significantly influence the damage recovery and thus the lifetime of the self healing TBCs. For effectiveness, the healing parameters are non-dimensionalized with the corresponding geometric/material values. As customary in a parametric analysis, while studying the influence of a given variable, all the other parameters including the healing particle distribution are kept constant. The results are discussed in terms of TBC crack patterns and number of cycles to failure.

EFFECT OF FILLING RATIO (PARTIAL HEALING)

In this section, the influence of the filling ratio defined as the ratio of healed crack length ($L_H$) to the particle diameter ($D_P$) on TBC lifetime is studied. Simulations are carried out for six different ratios given by 0, 1, 2, 3, 4 and $\infty$. The filling ratio of zero corresponds to no healing case whereas the ratio of $\infty$ leads to complete healing of all the cracks connected with the healing particle. In the model, crack filling occurs only in the thermal cycle considered and there is no delayed crack filling in later cycles. In principle, the crack filling ratio is related to the volume expansion due to the decomposition of the healing particle, but also depends on the average crack opening distance and particle volume. In the current model defining the crack filling ratio is used for simplicity. TBC microstructural features such as interface morphology and distribution of healing particles are kept constant. The volume fraction of the healing particle is again fixed with a value of 5%. The results are summarized in terms of crack patterns as illustrated in Fig. 6.7 for a common cycle number (cycle 11) for all filling ratios. From Fig. 6.7, it can be seen that the amount of cracking in TC layer decreases with an increase in filling ratio, as expected. For instance, at the 11th thermal cycle, complete TBC failure is observed for zero filling ratio (no healing) whereas only minimal cracking is observed for the healing ratio of $\infty$ (Complete healing). TBC crack pattern during failure along with number of cycles to failure for different filling ratios are reported in Fig. 6.8. It is also interesting to note that the fracture pattern at failure remains similiar for all the healing ratios considered with the majority of cracking at the splat boundaries close to the TC/BC interface. In terms of TBC life time, the increase in filling ratio leads to increase in cycles to failure as shown in Fig.6.8. However, the predicted number of cycles to failure for the ratios $L_P/D_P = 1,3$ and $L_P/D_P = 3,4$ are same with the values of 15 and 24 cycles, respectively. It is interesting to note that for the self healing TBC with zero healing ($L_P/D_P = 0$), the cycles to complete failure (11 cycles) is lower than the benchmark TBC which fails at 13 cycles (refer Fig. 6.6). This is as stated earlier, because of the additional cracking introduced in the TBC due to CTE mismatch between the healing particles and the TC layer[KPTvdZ18]. For self healing TBC with healing ($L_P/D_P > 0$) the number of cycles to failure remains higher than the benchmark case. The increase in TBC lifetime for $L_P/D_P \geq 1$ is attributed to the partial/complete healing of the

cracks. Thus it can be concluded that the presence of healing particle without healing of cracks or healing activation is detrimental to the TBC performance.

$L_H / D_P = 0$          $L_H / D_P = 1$



$L_H / D_P = 2$          $L_H / D_P = 3$

$L_H / D_P = 4$          $L_H / D_P = \infty$
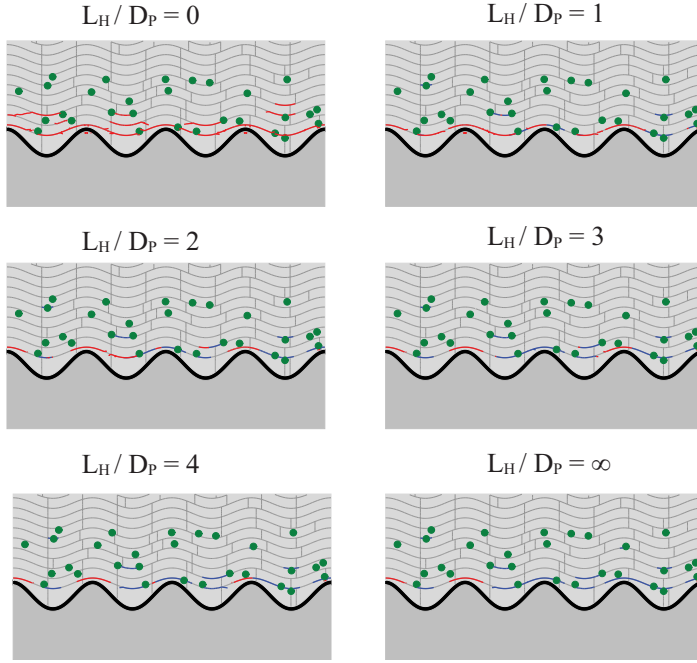
Figure 6.7: Fracture pattern of self healing TBC system at the $11^{th}$ thermal cycle for different crack filling ratios given by $L_H/D_H$ = 0, 1, 2, 3, 4 and $\infty$

### EFFECT OF FRACTURE PROPERTIES OF HEALING MATERIAL

The fracture properties of the healed material plays a crucial role in strength recovery [ZZY+15] and thus in controlling the lifetime of the self-healing TBCs. This effect is studied by varying the healed fracture parameter, which is represented in terms of the fracture ratio ($f$). The parameter $f$ is defined in the present study as the ratio of apparent ductilities of two materials, with the apparent ductility itself being measured as the ratio of the fracture strength to the fracture energy. Hence, the parameter $f$ for the healing material and the TC is defined as the ratio of fracture strength ($\sigma^H$)/fracture energy ($G^H$) of the healed material to the fracture strength ($\sigma_0^{TC}$)/fracture energy ($G_0^{TC}$) of the TC layer. For simplicity, studies are conducted only for the variations in normal fracture ratio ($f_n$) pertaining to local mode I failure. Also, the same fracture ratio is used to define the variations in $\sigma^H$ and $G^H$ the healed material. Simulations are carried out for six different fracture ratios given by $f_n$ = 1.5, 1, 0.75, 0.5, 0.25, 0. The fracture ratio greater than one ($f_n > 1$) represents that the healing material is stronger than the TC layer. Similarly, $f < 1$ represents that
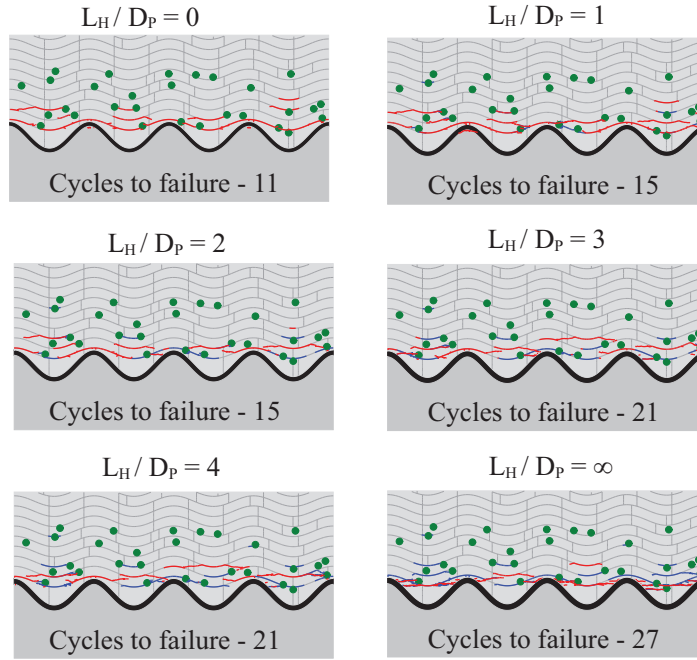
Figure 6.8: Final failure state and number of cycles to failure of self healing TBC system for different crack filling ratios given by $L_H/D_H = 0, 1, 2, 3, 4$ and $\infty$

the healing material is weaker compared to the TC layer. Thermal cyclic simulations are carried out for fixed TBC microstructure and the results are summarized in terms of final failure state and number of cycles to failure for different fracture ratios. The corresponding results results are shown in Fig.6.9.

The number of cycles to failure increases almost linearly for the fracture ratios greater than 0.25. It is also interesting to note that, for the case of stronger healed material ($f_n = 1.5$), a larger crack healed zone appears compared to the other fracture ratios considered. This is due to the fact that the healed region is stronger than the surrounding TC layer and with, subsequent thermal cycles, new crack surfaces are formed in the undamaged region of the TC layer. As may be observed in Fig.6.6, lower fracture ratios ($f_n \leq 0.25$), result in an early TBC failure compared to the benchmark TBC system. This is attributed to the interplay between two phenomena: (i) the additional cracking introduced by the healing particle because of CTE mismatch and (ii) the strength recovery due to healing. For the lower fracture ratios ($f_n \leq 0.25$) the additional damage introduced by the healing particle is more pronounced, which leads to early failure of the self healing TBC. In general, if the fracture properties of the healed material are less than the splat interfaces then the healing particles are detrimental to the self healing TBC.
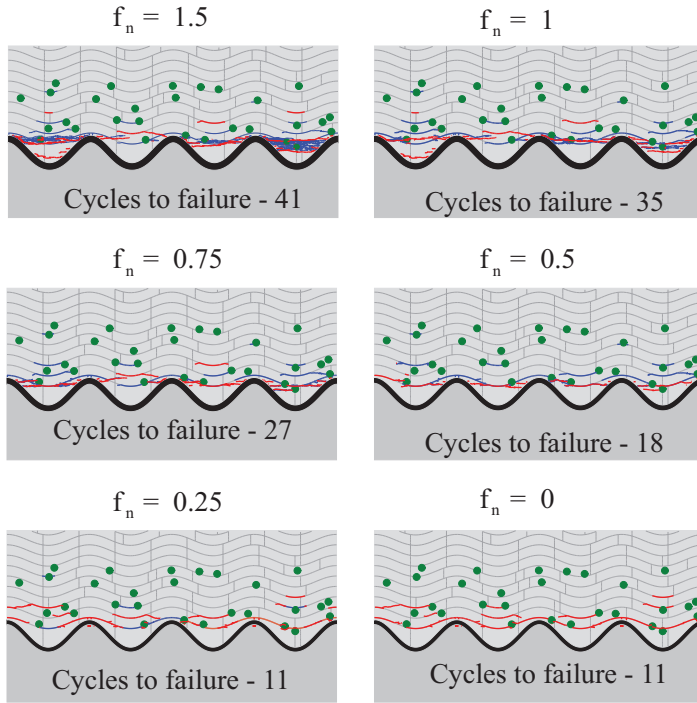
Figure 6.9: Final failure state and number of cycles to failure of self healing TBC system for six different fracture properties of the healed material, $f_n$ = 1.5, 1, 0.75, 0.5, 0.25, 0

## 6.4. Conclusion

Thermal cyclic behavior and life time predicition of self healing TBC were studied using the developed cohesive-zone based crack healing model in a finite element framework and fracture patterns of the self healing TBC life time extension are analyzed in comparison to a conventional TBC system. Parametric simulations are carried out to predict the influence of healing parameters such as crack filling ratio and strength recovery of the healed crack on the lifetime extension of the self healing TBC system. From the self healing simulations the following conclusions can be drawn.

- Self healing TBC shows a significant improvement in lifetime when compared with the conventional TBC. However, for a given volume fraction and particle size the lifetime extension is influenced by the spatial distribution of healing particles.

- The lifetime of the self healing TBC increases with the crack filling ratio due to partial/complete healing of cracks. The number of cycles to failure becomes

higher provided a minimum crack filling ratio is achieved.

- The number of cycles to failure increases linearly with increasing the fracture properties of the healed material. However, a strength of the healed material below that of the splat interface leads to early failure.

- The presence of healing particles in the TBC system without healing and/or healing activation is detrimental to the TBC performance.

In view of optimizing the design of a novel self healing TBC system, it is recommended to focus on maximisation of the crack filling ratio and the fracture properties of the healed material. Healing fracture properties below that of the pristine material still lead to improvements in lifetime. Additional benefits can be achieved when the healing fracture properties rise above that of the pristine material. Further, in view of designing a robust activation mechanism, large numbers of healing particles distributed uniformly with in the first splat interface are also desirable.

**6**

# 7

# APPENDIX

# DETERMINATION OF FRACTURE PROPERTIES BASED ON A WEDGE LOADING TESTING METHODOLOGY

[1]A wedge loaded testing methodology to determine the fracture energy and strength of (semi-) brittle (metallo-)ceramics is presented. The methodology combines a tailored specimen geometry and a comprehensive finite element analysis based on cohesive zone modelling. The use of a simulation-based approach to extract both fracture strength and energy from experimental data avoids the inherent inaccuracies found in closed-form expressions that rely on a priori assumptions about the deformation field. Results from wedge splitting tests on $Ti_3SiC_2$ and $Ti_2AlC$ (MAX phase) materials are used to illustrate the procedure. The simulation-based approach is further validated by comparing the fracture strength and fracture energies predicted by the proposed method and those indicated by a conventional four-point bending fracture toughness test (ASTM standard). The new protocol offers the possibility to measure not only the fracture properties of brittle material in its pristine state but also in the healed state

---

[1]This chapter also appears in the doctoral thesis of Ann-Sophie Farle entitled "Self-healing $M_{n+1}AX_n$-phase ceramics"

## 7.1. INTRODUCTION

Testing procedures to accurately quantify the fracture strength and fracture energy of materials typically depend on a variety of factors such as the material's elastic characteristics (compliant or stiff) and its fracture response (ductile or brittle). The absolute values may also depend on loading rates, the measured primary response variables such as loads and displacements and the post-processing of the recorded data. Ease of sample preparation, insensitivity to non-defined parameters and repeatability of the results also plays a significant role in the design of a testing procedure. For brittle materials, it is also known that the measured fracture properties depend on the ratio between the size of the critical flaw(s) and the zone where the stress concentrates in the sample (e.g., the measured fracture strength in a tensile test would typically be different from that in a bending test). Bending tests have been accepted as the simplest yet least precise test method to determine fracture strength and fracture energy of brittle materials [Ben01, AST16]. Bending tests commonly require controlled pre-cracks, which are difficult to produce and measure in most (semi-) brittle materials [AST16, FM12]. Moreover, this test, assuming a machining induced pre-crack in the material, may overestimate the fracture toughness and is highly sensitive to machining induced surface imperfections [FM12]. The sensitivity to surface flaws furthermore creates the necessity for higher sampling sizes to compensate for measurement error. The wedge splitting test was established by Tschegg [Tsc86]. Wedge-loading to determine fracture properties in concrete and concrete like materials has been performed by Bruhwiler et al. [BW90] but not yet modified and applied to the specific requirements of ceramic materials. In addition to the aforementioned difficulties, the quantification of crack-healing efficiency in self-healing materials requires methods to create stable cracks. Chevron-notched specimens can negate problems caused by pre-cracking attempts so in this sense this sample geometry is generally viewed as an improvement compared to samples without chevrons [AST16]. Furthermore, when setting the requirements for an optimally informative test method, it is clear that an ideal test should not only report the load-displacement data but also the actual crack length at every stage of the cracking process. For the determination of the crack length both optical [CB12] and acoustical methods [WJP16] are available while in specific cases also X-ray tomographic methods [SPM+16] can be used.

Aside from the physical testing requirements defined above, an important aspect of a testing methodology is the interpretation of the measured data. The quantities of interest, fracture strength and fracture (propagation) energy, are typically not measured directly but rather need to be derived from the measured response variables such as loads and actual crack dimensions.. For fracture properties, the traditional approach has relied on using the theory of Linear Elastic Fracture Mechanics (LEFM), which, often in combination with analytical solutions for simple geometries or finite element simulations (FEM) for complex geometries, is used to derive closed-form expressions from which the fracture strength and/or the fracture toughness can

be computed (i.e., a critical value of the stress intensity fracture at which a crack propagates) [BS10, NSRR09]. An alternative approach is to conduct finite element (FEM) numerical simulations of the fracture test using a Cohesive Zone Modelling (CZM) approach [HMP76, SSC13]. In combination with the experimental data, the simulations can be used to extract the fracture properties of the material taking into account the whole fracture process, namely nucleation and propagation of a crack. CZM combines ingredients found in stress-based and energy-based formulations for fracture mechanics. CZM has been implemented in conjunction with cohesive elements and, more recently, within the so-called eXtended Finite Element Method (XFEM). This methodology overcomes some intrinsic limitations of the (traditional) LEFM approach since it can model both nucleation and propagation of cracks. CZM, with either cohesive elements or XFEM, has been applied, for example, in [CBCS11] to predict the fracture behaviour of adhesive joints, in [EM12] for the analysis of delamination in fiber-reinforced polymer (FRP) beams, in [QZvdK13] to simulate the crack propagation in wood, in [XY09] to predict the fatigue crack nucleation and propagation in quasi-brittle materials, in [YWD$^+$13] to estimate the fracture toughness of free standing 8 wt. % $Y_2O_3$-$ZrO_2$ (8YSZ) coatings and in [JJ14] to analyze a specimen geometry to enhance crack stability for brittle materials and to improve closed-form formulas by deriving the so-called geometrical factor for different specimen dimensions. Other relevant work includes [LKK13], where simulations were conducted to predict the fracture properties of asphalt using a semi-circular bend test (SCB), and [LAWDS13] where simulations were used to demonstrate the variability and anisotropy of fracture toughness of cortical bone tissue using the load-displacement curve obtained from the three-point bending tests. While the accurate determination of the fracture properties of pristine (brittle) materials is demanding as it is, with the recent development of self-healing ceramic materials, a new requirement also has to be taken into account, namely that the sample is not split into separate pieces in the determination of the fracture strength and the fracture energy. Only if the crack is contained within the sample, the sample can be exposed to a simple (thermal) healing treatment not requiring uncontrolled manual realignment and clamping of the two fracture surfaces. The test set-up as described here, meets this important requirement. So the aim of the work is to develop a fracture test method and data analysis protocol to determine both the fracture strength and the fracture toughness of a pristine brittle material in such a manner that after initial fracture testing the sample is in a state suitable for subsequent thermal healing and determination of the fracture properties of the healed sample. The current approach is demonstrated for two semi-brittle MAX phase ceramics, which not only have attractive mechanical properties at ambient and high temperatures [Bar01] but also recover their mechanical strength upon high temperature annealing [SPM$^+$16, LSK$^+$12, YWD$^+$13]. In the present analysis we only focus on the determination of the fracture properties in the pristine state.

**7**

## 7.2. EXPERIMENTAL AND MODELLING

### 7.2.1. SPECIMEN MANUFACTURING AND TEST SETUP

The new chevron-notched, wedge-loaded specimen geometry (WLS) is shown in Fig.7.1. The basal half-length is chosen as 0.48 times the longest height of the sample. A curvature with a radius of 52 mm as the base allows sample self-alignment under loading conditions. A chevron notch tip is located at a depth of 10 mm. The contact edges of the notch opening are rounded with a radius of 1 mm to minimize the friction with the loading-wedge. A 90° guide-groove is machined into the side of the sample to reduce the thickness by half. The recommended thickness of 5 mm is within the limits set by the ASTM E647 standard for compact tension specimen [AST13]. In this study, samples with a basal half-length of 12 mm, a height of 25 mm and thickness of 5 mm were used.
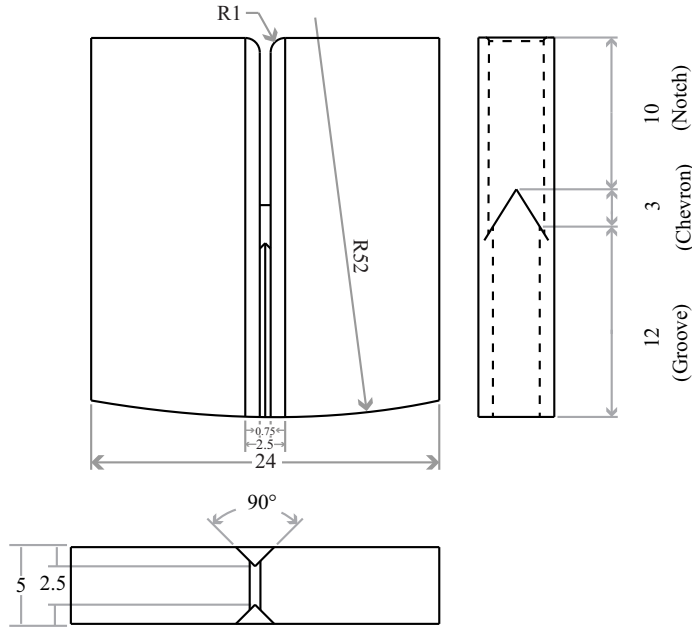


Figure 7.1: Wedge splitting test specimen geometry with dimensions in mm

Samples of $Ti_2AlC$ and $Ti_3SiC_2$ were synthesised by reactive sintering in a spark plasma sintering (SPS) furnace (HP D 25 SD, FCT Systeme GmbH, Germany). Elastic properties were determined by Vickers indentation using a hardness tester (Zwick/Z2.5, Germany). Indents were created by loading the indenter with 5 N/s up to 50 N, holding for 12 s and unloading with 3.7 N/s. All $Ti_2AlC$ and $Ti_3SiC_2$ samples were more than 92 % dense. All machining was carried out by electric discharge machining (EDM) with wire diameters of 0.25 and 0.1 mm.
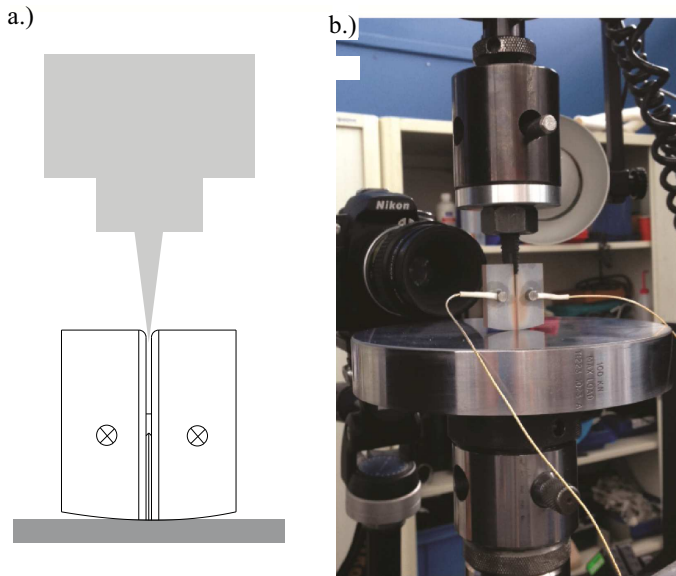
Figure 7.2: Test setup of chevron-notched, wedge-loaded specimen (WLS) with microphone positions indicated (a) schematic and (b) actual test setup.

The test setup is shown schematically in Fig. 7.2. Tests were performed using a 100 kN electro-mechanical load frame (Series 5500R, Instron, USA) that was fitted with a 10 kN load cell to suit the recorded load levels. The sample was placed on a flat stainless steel base-plate without further clamping. The quenched and tempered steel 10° wedge was lowered into the sample grove until it reached a pre-load of approximately 10 N.

Tests were carried out under closed-loop displacement control, with a fixed crosshead displacement rate of 0.01 or 0.1 mm/s. Crosshead displacement signal was calibrated by compression tests with strain gauge control to correct for rig deformation under the applied loads. The crosshead motion was stopped when a load drop of 50 % from peak load was recorded. Upon termination, the crosshead motion was reversed leading to retraction of the wedge. Unloading curves were not recorded.

The recording of the acoustic events during the fracturing was performed with a Physical Acoustics module (PCI-2, 2 channel 40 MHz 18 bit data-acquisition combined with ILS40 pre-amplifiers). Registration and post-processing were executed with the Physical Acoustics AEWin 1.70 (2005) software module. Prior to testing, two microphones were attached with paraffin wax to the right and left of the sample groove to allow registration of acoustic emission signals during the experiments. The sampling rate employed was 2 MHz with a 20 dB amplification factor. An acoustic

**7**

event was recorded if the signal level of any microphone exceeded 5 mV. Every event was separately recorded as a waveform file containing 2048 points at 0.5 $\mu$s intervals. The energies recorded varied in a wide range between 1 aJ to 1 nJ. A cumulative energy as a function of time, termed the "acoustic energy", was obtained through post-processing of the acoustic events. Here, the total acoustic energy is assumed to be proportional to the total amount of fracture introduced in the specimen. Final crack lengths and microstructure were determined by optical microscopy using a digital microscope (Keyence VHX-100, Osaka, Japan) and scanning electron microscopy (SEM), type JSM 6500F (JEOL Ltd., Tokyo, Japan) equipped with an energy dispersive spectrometer (EDS, type: ThermoFisher UltraDry 30 mm$^2$ detector) for X-ray microanalysis (XMA) and with Noran System Seven software package for data acquisition and analysis. Surfaces and cross-sections, prepared by cutting with a diamond wafering blade, were ground using SiC paper up to 4000 grit and polished with diamond suspension up to 1 $\mu$m.

### 7.2.2. Finite element model

The extraction of fracture material properties is based on simulating the actual experimental set up using a Finite Element approach with cohesive zone modelling . The finite element model of the chevron-notched, wedge-loaded specimen (WLS) test set up is shown in Fig.7.3. For computational efficiency, the specimen is modelled as a two-dimensional domain under plane stress assumption. To simulate the three-dimensional features of the specimen, the chevron notch and the groove in the specimen geometry are modelled using a variable thickness. The fracture process is simulated using cohesive elements which were inserted along the along inter-element boundaries to capture the onset and evolution of the fracture process. In the present analysis, cohesive elements are inserted at the interfaces of all bulk elements in the regions where crack(s) are expected to initiate and propagate, in particular at the chevron and groove. A bilinear traction-separation relation [SSC13] is used to describe the local nucleation and crack-opening process within the numerical sample as shown in Figure Fig. 7.3.a and the corresponding finite element mesh is shown in Fig.7.3.b.

A fine mesh is used in the region of interest (groove and chevron) and a coarser mesh is used in other regions. The boundary conditions in the simulations are chosen such that they closely reproduce the testing conditions. The displacement of the top of the wedge is prescribed as a function of time according to the loading rate whereas the bottom of the support plate is modelled as simply-supported. The wedge and the support are included in the simulation as deformable parts. The contact between the wedge and the specimen is modelled as (Coulomb) dry-friction with a surface-based penalty (isotropic) formulation with a coefficient of kinematic friction f. The elastic responses of the wedge and the specimen are modelled using isotropic and linear relations with Young's modulus and Poisson's ratio taken as E$_w$=200 GPa, $v_w$=0.3 and, for the specimens, as follows:

a.)
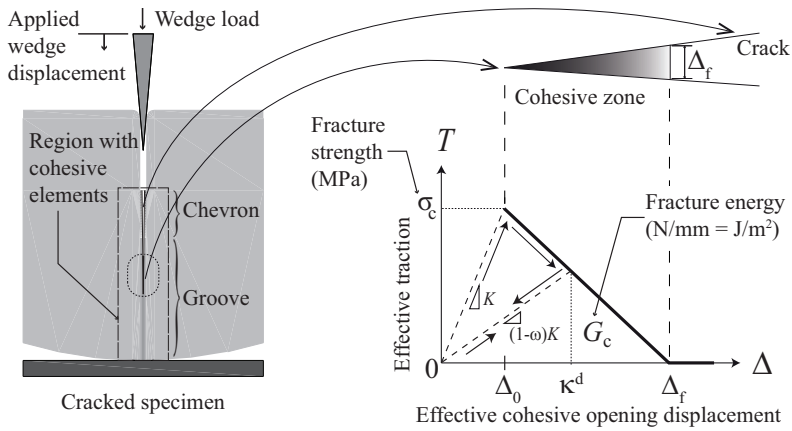


b.)
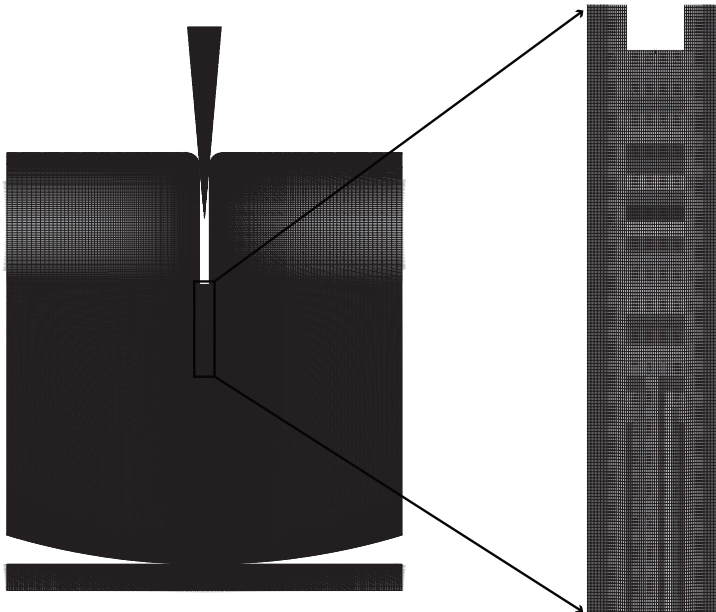


Figure 7.3: (a) Numerical model of wedge splitting test specimen with a bilinear cohesive relation implemented in cohesive elements to simulate the fracture process during testing. The area under the curve corresponds to the fracture energy per unit area required to fully separate the cohesive surface. (b) Finite element mesh of wedge splitting test specimen. The inset shows the elements in the chevron modelled with varying thicknesses.

**7**

Table 7.1: Elastic properties of the specimens

| Specimen | $E_s$ (GPa) | $v_s$ |
|----------|-------------|-------|
| $Ti_3SiC_2$ | 320 | 0.2 |
| $Ti_2AlC$ | 260 | 0.18 |

where the subscript refers to the wedge (w) or specimen (s). The elastic properties of the specimens are obtained from published data [Gil00, BAER00, QGZ$^+$11] and verified with indentation tests whereas the wedge properties are taken from the wedge material's specification. The support is modelled as an elastic material that approximates a rigid body with frictionless contact used at the interface of the support and the specimen. Preliminary simulations including plasticity in both the specimen and the wedge were carried out to determine its likelihood of occurrence and its possible effect on the results. It was concluded that plastic behaviour is confined to a small region close to the cracks and its effect cannot be separated from the cohesive relation (i.e., at the length scale of the simulation, it is possible to model the bulk response of the material as elastic and use a cohesive relation to capture the inelastic behaviour). Since the purpose of the simulations is to determine the fracture properties of the specimen, a parametric analysis was carried out varying the effective fracture strength and the effective fracture energy. In addition, it is known that for a wedge-splitting test, friction can play a significant role [FM12]. Consequently, distinct values of the (kinematic) friction coefficient used in Coulomb's model were considered.

## 7.3. SIMULATION SETUP

To simulate the test, a downward displacement of the top of the wedge is specified. Upon contact with the specimen, the specimen undergoes a loading dominated by an opening mode (mode I), although the actual loads at the crack tip are obtained from the simulation. The corresponding reaction force at the top of the wedge, which is obtained as a result of the simulation, is recorded throughout the simulation. The procedure to extract the fracture material properties is as follows:

1. A preliminary elastic simulation is carried out for different values of the coefficient of friction. The value of for which the initial slope of the simulation coincides with the initial slope of the experimental data to within a desired tolerance is then used for subsequent steps. If the experimental and the simulation responses deviate from a linear curve, then it is recommended to match the average slope until the onset of cracking as measured from the acoustic emission.

2. With a chosen (fixed) coefficient of friction, a parametric analysis including fracture is carried out for different values of the fracture strength and fracture

energy.

3. For each pair of values of fracture strength and energy, the wedge load is obtained as a function of the wedge displacement. This prediction is compared with the experimental response. The actual fracture material properties are taken as those for which the simulation provides the best approximation to the experimental data. In accordance with the CZM approach, the best fit is obtained by comparing the predicted and the experimentally-obtained maximum load and total energy dissipated. As a verification step, the crack length predicted in the simulation is also recorded as a function of the wedge displacement and compared with the experimental data.

## 7.4. RESULTS AND DISCUSSIONS:

### 7.4.1. EXPERIMENTAL RESULTS

The measured wedge load as a function of the wedge displacement for the samples tested is shown in Fig. 7.4.a for $Ti_3SiC_2$ and in Fig. 7.4.b for $Ti_2AlC$. Figures Fig. 7.4.a and Fig. 7.4.b also show the measured crack length and cumulative acoustic signal as a function of the wedge displacement for one representative $Ti_3SiC_2$ sample and one $Ti_2AlC$ sample. The crack growth curve for the $Ti_3SiC_2$ sample shows a slow and controlled crack propagation. For the $Ti_2AlC$ sample, the crack growth is mostly controlled except during the transition from the chevron to the groove where the crack length increased abruptly. However, subsequent crack growth in the groove proceeded in a controlled fashion. In general the following regions of crack growth can be identified:

1. Slow propagation that occurs in the chevron due to the gradual increase in thickness of the specimen.

2. Fast propagation observed in the transition region between the chevron and the groove due to the sudden decrease in the thickness.

3. Subsequent slow propagation in the groove when the crack growth stabilizes because of the constant thickness in the groove. Based on preliminary tests where the loading was interrupted at fixed intervals and the crack length was optically measured (not reported here for conciseness), a reasonably good correlation is found between crack propagation and acoustic energy, which indicates that this parameter can be used to estimate crack length. The use of acoustic emission data to measure onset of crack growth in fatigue testing is further described by Bassim et al. [BLL94], Moorthy et al. [MJR94] and Roberts et al. [RT03].

The experimental results shown in Figures Fig. 7.4 were conducted continuously so the acoustic energy was normalized using only the crack length at the end of the experiment, which was measured by optical and scanning electron microscopy. The

final crack length recorded for the $Ti_3SiC_2$ sample was 9.6 mm and for $Ti_2AlC$ sample was 11.36 mm, measured from the tip of the chevron notch.

According to the crack lengths, determined from acoustic emission data, shown in Fig. 7.4.a and Fig. 7.4.b, crack formation in the chevron occurred before the peak load was reached. Crack development in the chevron notch starts in the early stages of testing, at relatively low load levels. For $Ti_3SiC_2$ samples, as shown in Figure 5a, the peak load appears to coincide with the instant when the crack front moves from the chevron to the uniform groove. For $Ti_2AlC$ samples this transition apparently occurs during a fast propagation stage, so it is not possible to uniquely correlate the peak load and a specific crack length.

As shown in Fig. 7.4.a, the load displacement curves of the individual $Ti_3SiC_2$ samples are relatively close to each other, reaching a peak load at approximately the same wedge displacement. The average peak load for $Ti_3SiC_2$ is approximately 180 N. In contrast, the $Ti_2AlC$ samples showed more variability as observed in Fig. 7.4.b. The peak load was reached at distinct values of the wedge displacement. Consequently, the average peak load for $Ti_2AlC$, which is approximately 210 N, does not exactly coincide with the peak load of the average response, which is slightly lower as shown in Fig. 7.4.b. Nonetheless, the average response is used for comparison purposes with the simulation results as detailed in the next section.

### 7.4.2. Fracture Properties

In accordance with the procedure outlined in Section 2.4, the first step is to determine the coefficient of friction between the wedge and the sample. The wedge load as a function of the wedge displacement for distinct possible values of the coefficient of friction is shown in Fig. 7.5.a for the $Ti_3SiC_2$ samples and in Fig. 7.5.b for the $Ti_2AlC$ samples. The simulations also include the fracture behaviour for reference purposes, although only the initial elastic response is required to determine the value of . For the values considered, the best match for the (average) initial response is attained with a coefficient of friction for the $Ti_3SiC_2$ samples and for the $Ti_2AlC$ samples, which are within the range of published values [Gil00].

With the chosen coefficients of friction, simulations were conducted for distinct values of the fracture strength and the fracture energy. The wedge force as a function of the wedge displacement is shown in Figures Fig. 7.6.a and Fig. 7.6.b for a fixed value of the fracture energy and various values of the fracture strength of, respectively, the $Ti_3SiC_2$ and $Ti_2AlC$ samples. Similarly, Figures 8a and 8b indicate the load-displacement response for a fixed value of the fracture strength and various values of the fracture energy.

From Figures Fig. 7.6.a and Fig. 7.6.b it can be observed that, as anticipated, the fracture strength mostly affects the peak load, but the rest of the curve is somewhat similar for a fixed value of the fracture energy. In contrast, as shown in Figure Fig. 7.7.a and Fig. 7.7.b, both the peak load and the energy dissipated in the process increase with increasing fracture energy for a fixed fracture strength. A comparative analysis

a.)



b.)
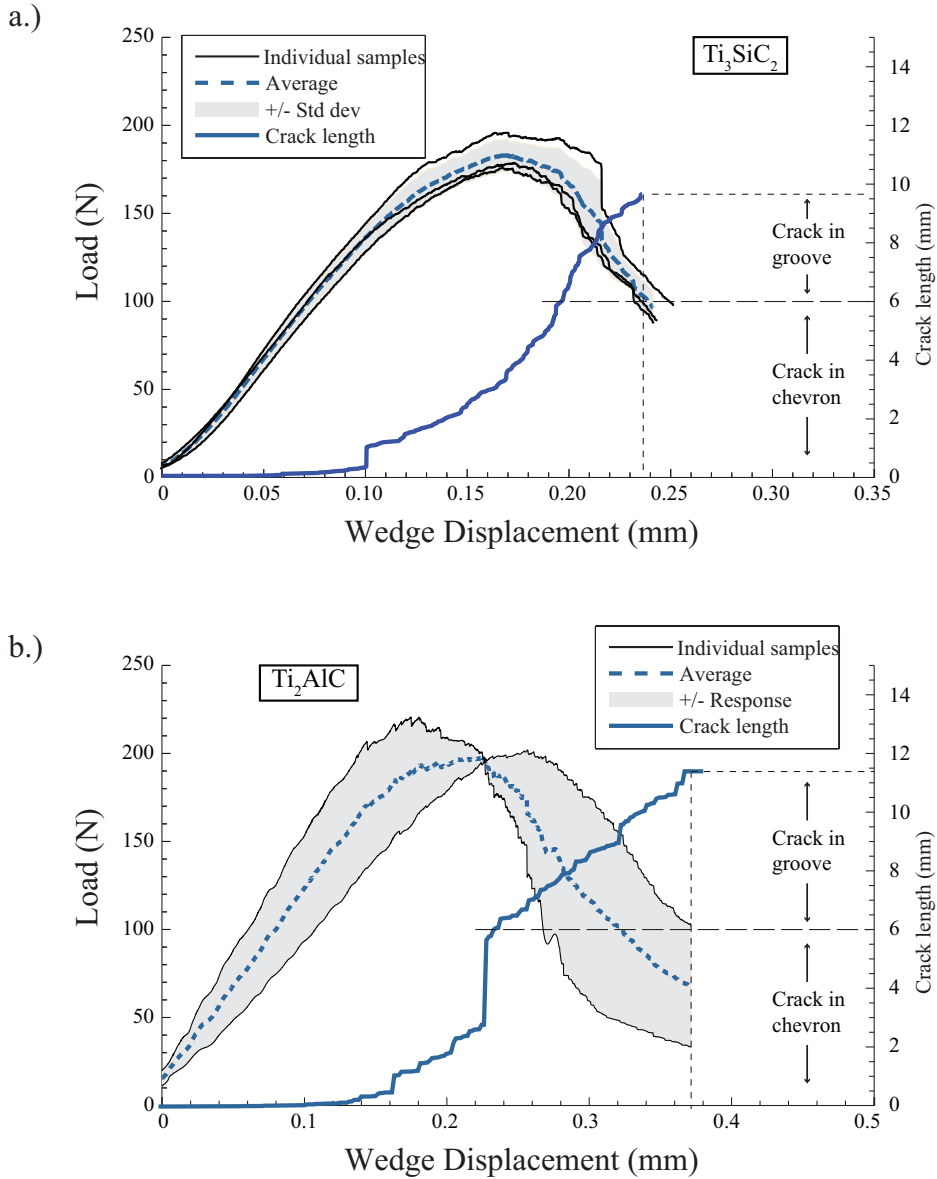


Figure 7.4: Wedge load (left axis) and normalized crack length (right axis) versus wedge displacement for (a) $Ti_3SiC_2$ and (b) $Ti_2AlC$ samples. The dashed blue line represents the average between the samples. The crack length is deduced from the acoustic energy and it is normalized using a directly measured crack length value at the end of the test. The measured crack length for $Ti_3SiC_2$ and $Ti_2AlC$ samples are 9.6 mm and 11.36 mm, respectively

7
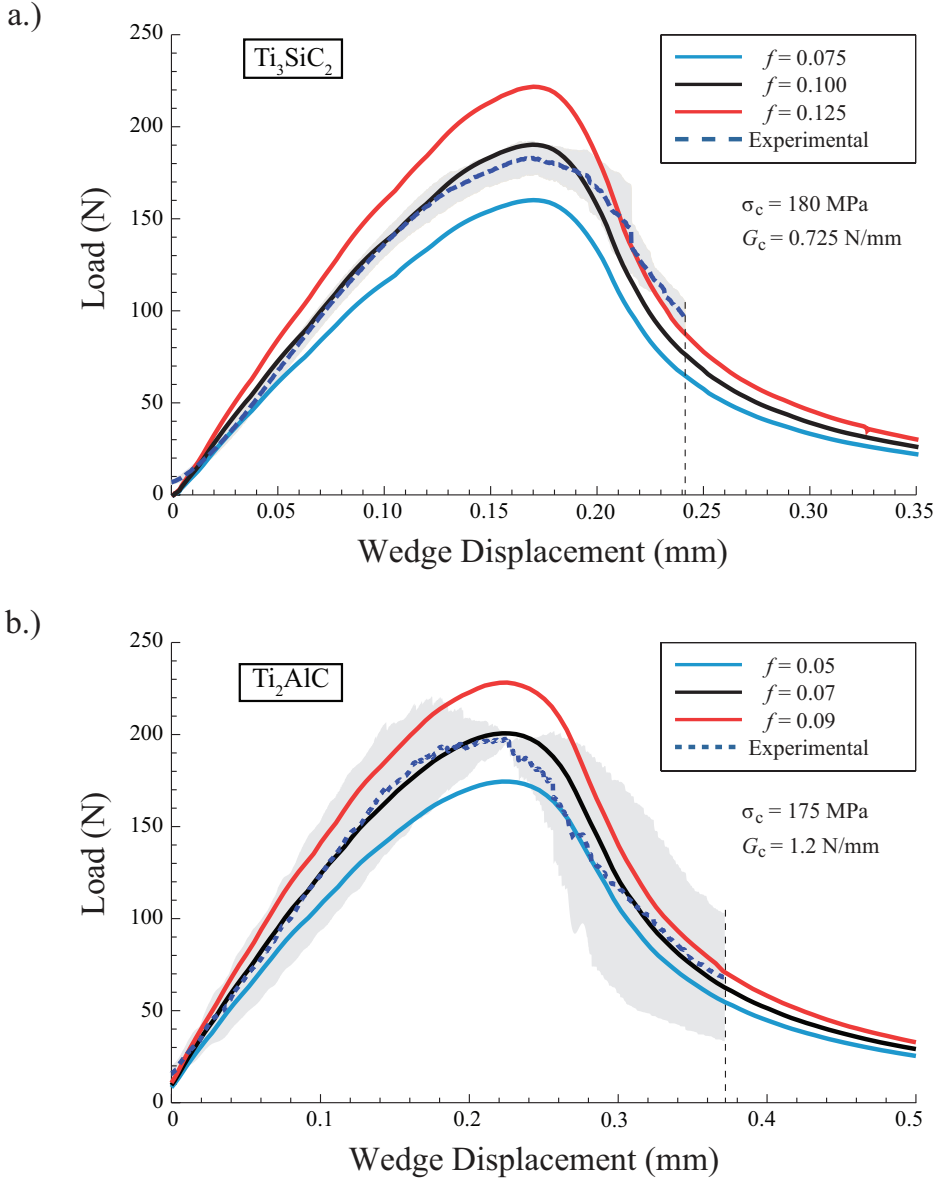
Figure 7.5: Wedge load as a function of wedge displacement for three distinct values of the coefficient of friction between the wedge for (a) Ti$_3$SiC$_2$ and (b) Ti$_2$AlC specimens. In accordance with the geometry shown in Fig.7.3, higher coefficients of friction effectively provide stiffer initial responses.

**7**
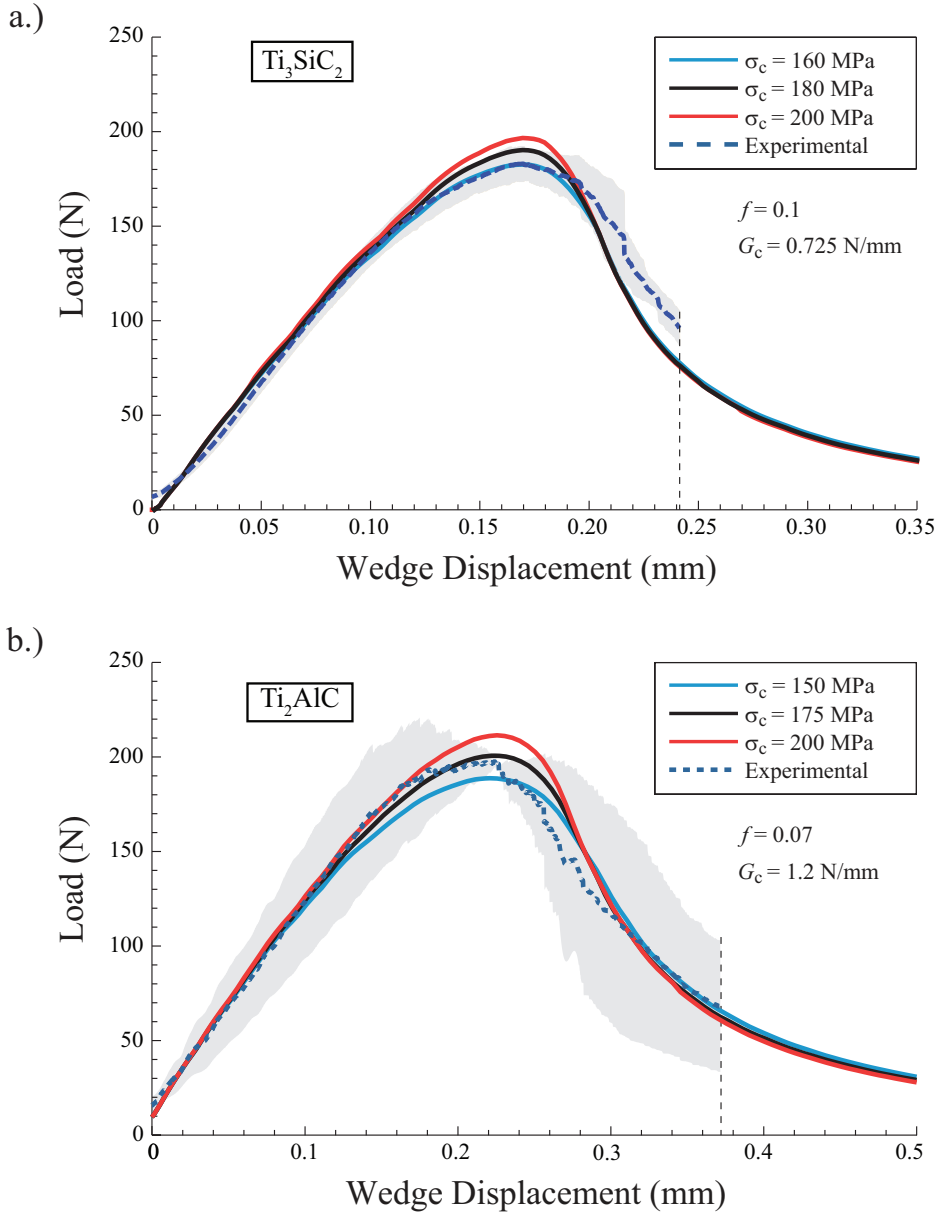
Figure 7.6: Wedge load as a function of wedge displacement for three distinct values of the fracture strength and for a fixed fracture energy of (a) 0.725 N/mm of the $Ti_3SiC_2$ and (b) 1.2 N/mm of the $Ti_2AlC$ specimens. Within the range of values analysed (160 MPa to 200 MPa for $Ti_3SiC_2$ and 150 MPa to 200 MPa for $Ti_2AlC$), the difference in response is mainly reflected in the peak load.

7

a.)



b.)
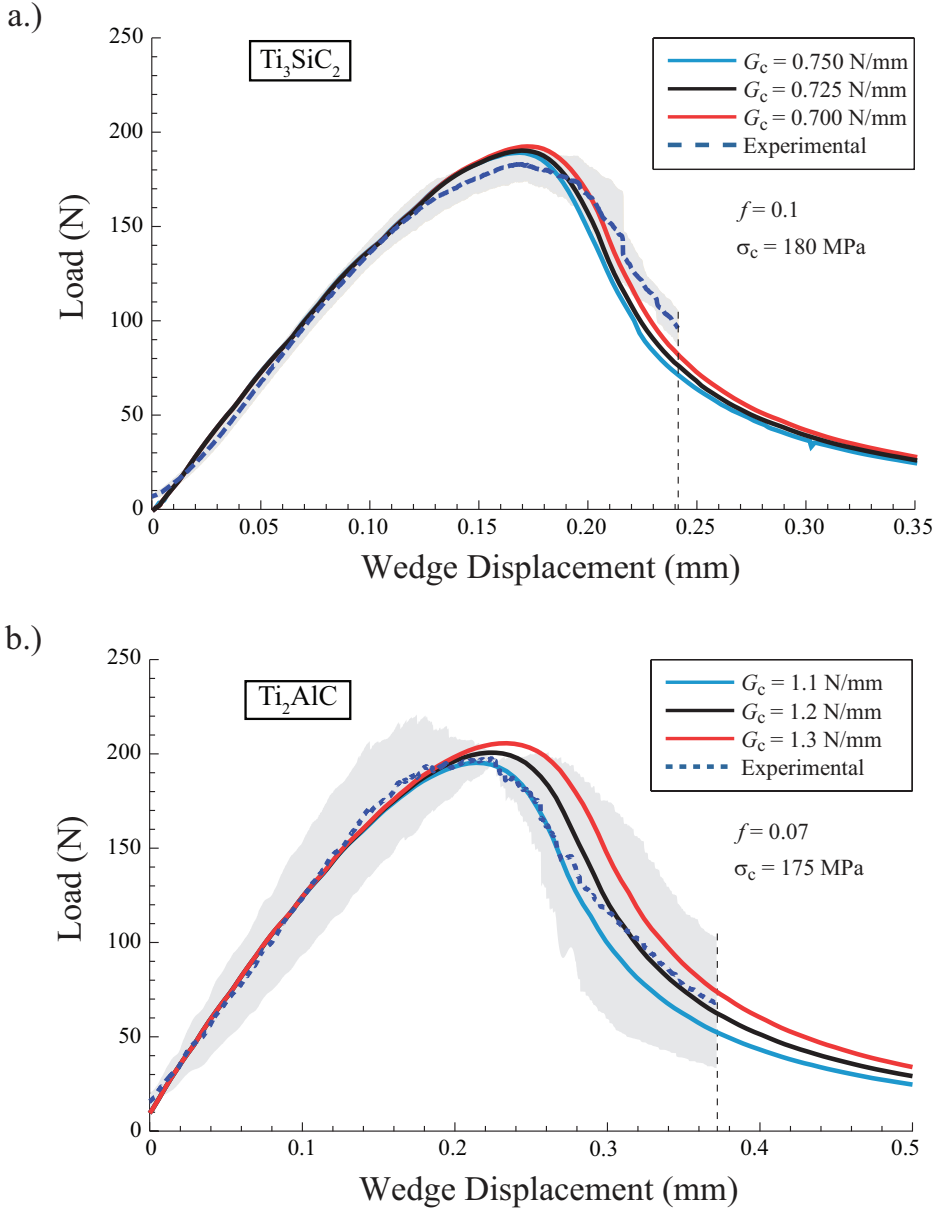


Figure 7.7: Wedge load as a function of wedge displacement for three distinct values of the fracture energy and for a fixed fracture strength of (a) 180 MPa of the $Ti_3SiC_2$ and (b) 175 MPa of the $Ti_2AlC$ specimens. As expected, the effective energy dissipated (measured as the area under the curves) increases for increasing values of the fracture energy. The best fit in terms of energy as well as the peak load is obtained with a (a) fracture strength of 180 MPa and a fracture energy of 0.725 N/mm for $Ti_3SiC_2$ and (b) fracture strength of 175 MPa and a fracture energy of $Ti_2AlC$ 1.2 N/mm specimens.

Table 7.2: Elastic properties of the specimens

| Material | Fracture strength $\sigma_c$ (MPa) | Fracture energy $G_c$ (N/mm) |
|---|---|---|
| $Ti_3SiC_2$ | 180 | 0.725 |
| $Ti_2AlC$ | 175 | 1.2 |

of the results shown in Figures Fig. 7.6 and Fig. 7.7 indicate that the peak load depends both on the fracture strength and the fracture energy. The fracture strength controls the early stage (nucleation) of cracks in the chevron while the fracture energy controls its subsequent propagation throughout the chevron and the groove. From the set of values considered in the simulations, the best fit for the average response of the $Ti_3SiC_2$ and $Ti_2AlC$ samples are as follows:

For $Ti_3SiC_2$, the predicted fracture energy value is within the range of values reported in literature [ERBZK99, Gil00, RBER$^+$02] while for $Ti_2AlC$ the predicted fracture energy is higher than the values reported in the literature [BAER00, WZ13]. To verify the capacity of the simulations to reproduce the experimental results, the predicted and measured crack length as a function of wedge displacement are shown Fig. 7.8 for the same values used in the results shown in Fig. 7.6 (i.e., variable strength) and in Fig. 7.9 for the same values used in the results shown in Fig. 7.7 (i.e., variable fracture energy.

The simulations shown in Fig. 7.8, and Fig. 7.9 indicate that the crack nucleates in the chevron and initially grows linearly as a function of wedge displacement. As the crack front approaches the transition region from the chevron to the groove (see Fig. 7.1, 2 and 3), the rate of growth increases. Subsequently, the growth rate decreases as the crack front further advances into the uniform groove. For the $Ti_3SiC_2$ samples, as shown in Fig. 7.8.a and Fig. 7.8.b, it can be observed that the simulations are in good agreement with the evolution of the crack length as deduced from the acoustic signal. For the $Ti_2AlC$ samples, as shown in Figures Fig. 7.8.b and Fig. 7.9.b, the simulations initially over-predict the crack length (as deduced from the acoustic signal) but, after a sudden crack propagation, the experimental and simulated evolutions approximately coincide. Comparing Fig. 7.8.a and Fig. 7.9.a for the $Ti_3SiC_2$ samples and Fig. 7.8.b and Fig. 7.9.b for the $Ti_2AlC$ samples, it can be observed that for both materials the initial crack length is more sensitive to variations in fracture strength and, conversely, the final crack length is more sensitive to variations in fracture energy.

Using the best fit fracture parameters, it can be seen that the instant when the crack front moves from the chevron to the uniform groove corresponds to a wedge displacement of 0.2 mm for the $Ti_3SiC_2$ samples and 0.25 mm for the $Ti_2AlC$ samples (see Figures 9a,b). Using these values in the horizontal axis in Figures 7a and 7b, respectively, it can be seen that the simulation predicts that the peak load occurs when the crack is still in the chevron (this effect is more pronounced for the $Ti_3SiC_2$

**7**

a.)



b.)



7
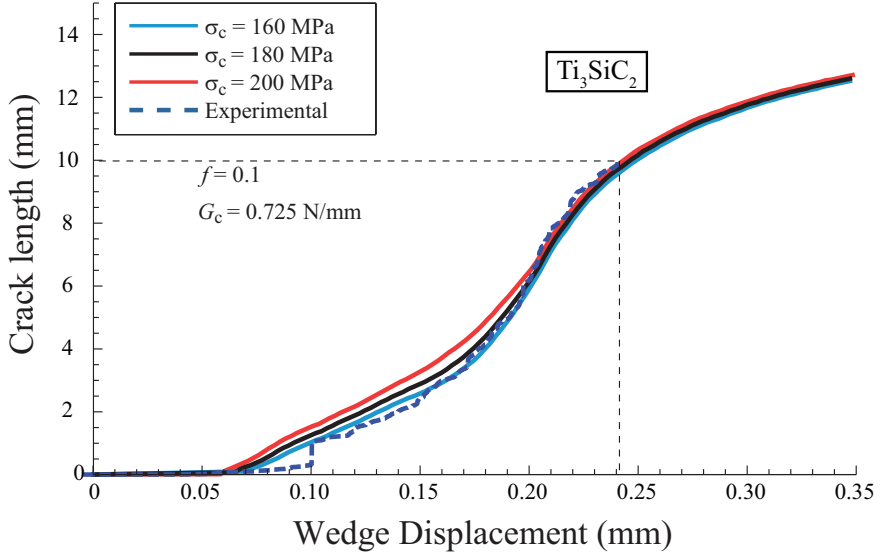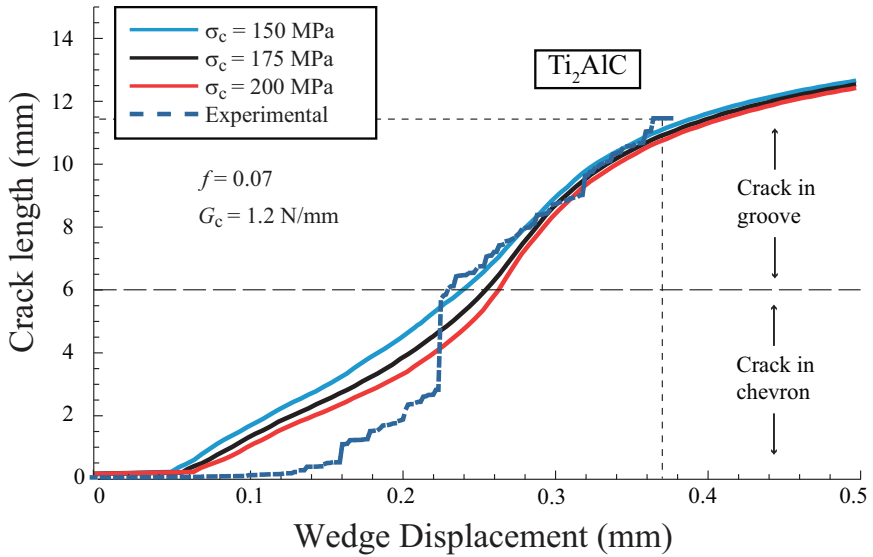
Figure 7.8: Crack length as a function of wedge displacement for three distinct values of the fracture strength and for a fixed fracture energy of (a) 0.725 N/mm for the $Ti_3SiC_2$ and (b) 1.2 N/mm for the Ti2AlC samples.

a.)
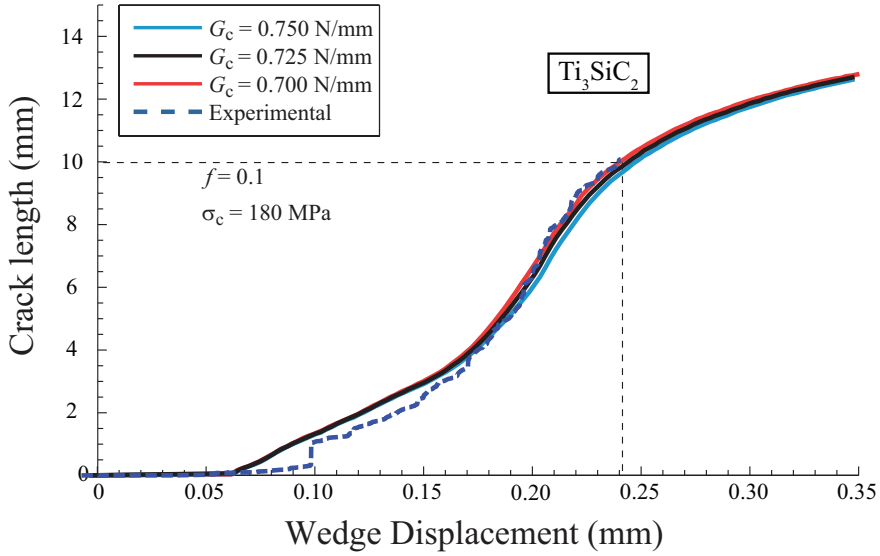


b.)
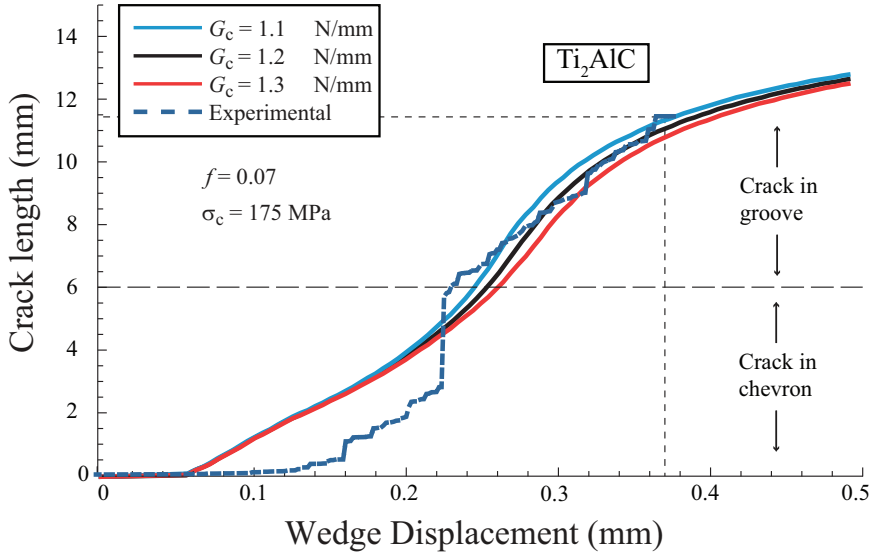


Figure 7.9: Crack length as a function of wedge displacement for three distinct values of the fracture energy and for a fixed fracture strength of (a) 180 MPa for the Ti3SiC2 and (b) 175 MPa for the Ti$_2$AlC samples. The initial crack growth, starting around a wedge displacement of 0.07 mm in the simulations, occurs in the chevron. The crack growth rate as a function of the wedge displacement is initially approximately linear. The subsequent change in slope corresponds to the transition from the chevron to the groove, which approximately coincides with the peak load.

sample than for the Ti$_2$AlC sample).

For the range of fracture strength analysed, the simulations predict a similar total crack length at the end of the loading, which matches relatively well the experimental value. This finding suggests that crack length may be used to estimate the fracture properties, but it may not be sufficiently sensitive to differentiate between distinct values. Differentiation between response curves are amplified as the crack front moves from the chevron to the groove, but the inherent uncertainty of acoustic-based crack length measurement suggests that it is better to extract material properties from the load-displacement curve as indicated above.

### 7.4.3. Comparison of simulation-based approach with a standardized procedure: four-point bending test with chevron-notched specimen.

The methodology described in the present work involves two novel aspects compared to existing (standardized) tests, namely the geometry of the specimen and the simulation-based approach to extract material properties. To cross-validate the simulation-based approach, the method was also applied to a standardized geometry for determining fracture toughness in brittle materials. To this end, a ASTM four-point bending test with a chevron-notched specimen was used as benchmark(Standard C1421-16, see [AST16]).

The comparison is done at the level of the post-processing of the data by comparing the simulation-based procedure and a standardized closed-form expression to extract fracture properties. Since the standardized four-point bending test is designed to extract the critical value of the stress intensity factor under nominal mode I conditions, it is necessary to relate this material property to the fracture energy. Assuming plane stress conditions and a small plastic zone, then the fracture energy can be related to the toughness as

$$G_c = (K_{Ic}^2)/(E_s) \tag{7.1}$$

where E$_s$is the Young's modulus of the specimen. For a given geometry of the chevron-notched specimen used in the four-point bending test, the ASTM standard provides a formula that uses the peak load recorded in the experiment to compute the critical stress intensity factor [AST16]. The ASTM model is plotted as a solid line in Fig.7.10. For the numerical simulations based on the cohesive zone, the procedure is as follows: the fracture properties are given (fracture strength and fracture energy) and the test is simulated. The fracture energy is computed from the critical stress intensity factor and given elastic properties (in this case with a Young's modulus of 280 GPa) while representative values of the fracture strength are chosen. The outcome of the simulation is the peak load, which is indicated in Fig.7.10 (discrete data points) for five values of the fracture strength, ranging from 100 MPa to 500 MPa. For each value of the fracture strength, a fitted curve is indicated to better visualize the predictions of the simulations. From Fig.7.10 it can be observed that

**7**

if the material is sufficiently brittle (i.e., relatively low fracture energy to strength ratio), the ASTM formula and the cohesive-zone simulation-based results provide comparable predictions, albeit for a limited range of fracture strengths. However, for higher values of the fracture energy, typically found in semi-brittle materials, the simulations predict a higher peak load. Note that this is only a qualitative comparison as it is not possible to ascribe a better accuracy to either procedure without access to a third reference approach deemed more precise. However, it can be concluded that for brittle materials (as intended in the ASTM analysis), the two procedures are somewhat similar while for semi-brittle and more ductile materials, the two methodologies provide different results.
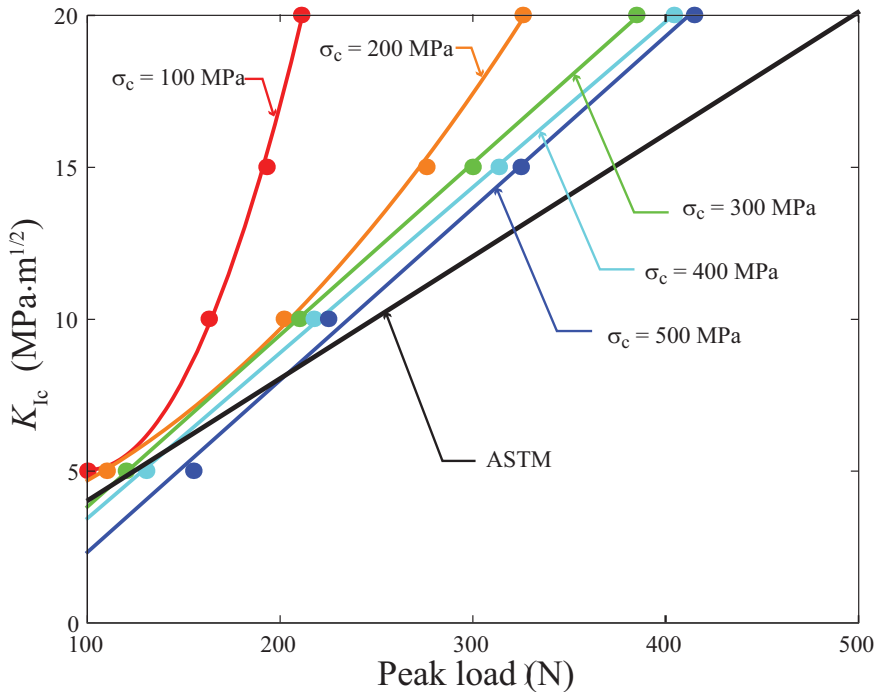


Figure 7.10: Critical stress intensity factor (fracture toughness) in a chevron-notched, four-point bending specimen. The black line is obtained based on ASTM C1421-16 [AST16] using the peak load as independent variable. The circles represent peak loads predicted from cohesive zone-based simulations for given fracture strengths and fracture energies, from which the corresponding critical stress intensity factors are estimated assuming plane stress conditions. The corresponding lines are interpolations of the simulation points.

The chevron-notched, four-point bending test (ASTM E399 [EC13]) was applied to five samples of $Ti_3SiC_2$ and five samples of $Ti_2AlC$ from the same batches as the ones used in the wedge splitting test. The samples were machined from the bulk

specimen by spark erosion and ground to a surface finish of 3 $\mu$m polish. However, it was not possible to achieve stable crack propagation in any sample even for relatively low loading rates. The ASTM standard considers a test to be valid only if stable crack growth can be achieved, hence these (invalid) tests are not reported in detail here. However, it is interesting to mention that the peak loads recorded would have predicted a significantly lower fracture energy compared to the values obtained from the wedge splitting test. It is also relevant to mention that the peak loads for the $Ti_3SiC_2$ samples were consistently lower than those of the $Ti_2AlC$ samples, showing a similar relative ranking as the wedge splitting test (i.e., $Ti_2AlC$ samples are tougher than the $Ti_3SiC_2$ samples). The most important observation, however, is that the wedge-splitting test allowed for a controlled crack growth whereas this was not possible to achieve with the four-point bending test. This demonstrates the significant benefit of the new proposed geometry for the purpose of testing healing efficiency in self-healing materials.

## 7.5. SUMMARY AND CONCLUSIONS

A new chevron-notched, wedge-loaded specimen and testing method are proposed to retrieve the intrinsic fracture properties from semi-brittle materials using matching finite element calculations based on cohesive zone elements. The combination of simple test setup and advanced simulations allows unique and accurate determination of both the crack initiation and the crack propagation properties of (semi-) brittle materials while minimizing commonly necessary simplifications and assumptions. The addition of acoustic emission recording proves to be a strong tool to determine crack initiation and for tracking of crack length extension. One important advantage of the proposed testing geometry and loading is that it allows to control crack growth and prevents full separation of the specimen. This is a critical requirement for testing self-healing materials in order to facilitate healing of the cracked surfaces. This approach was applied in $Ti_2AlC$ samples that were cracked using a wedge-splitting test, healed and re-tested twice. Results of the self-healing testing will be presented elsewhere. The simulations can be used to establish a simple closed-form formula for this geometry based on curve fitting. However, this would require extensive validation before it can be established as a standardized method, which is beyond the scope of the present work.

**7**

# 8

# APPENDIX -B
# CRACK TRACKING ALGORITHM

The real time crack tracking algorithm to determine the condition required for self healing activation is explained below:

---

**Algorithm 1** Crack tracking algorithm

---

**Require:** Total healing volume ($V_T$) , Max. heal length/cycle ($L_{H_{Max}}$) , Activation set ($AS$) - Cohesive elements connected to particle

1: $D_T$ (current cycle) ← Analysis output database      ▷ $D_T$ - Deformed coordinates and element Ids of failed elements in TC

2: $AHP \leftarrow AS \cap D_T$      ▷ $AHP$ - Activated healing particles and corresponding crack locations

3:   **for** $i = 0 : D_T$ **do**

4:     **for** $j = 0 : AHP$ **do**

5:       $HE^j \leftarrow AHP^j$      ▷ $HE^j$ - Elements healed by $j^{th}$ particle

6:       $(A_H{}^j),(L_H{}^j) \leftarrow H_E{}^j, AHP^j$      ▷ $A_H{}^j$ - Healing area, $L_H{}^j$ - Healed length

7:       $V_A{}^j \leftarrow V_T{}^j, A_H{}^j, L_H{}^j$      ▷ $V_A$ - Available healing volume

8:       **Update** $AHP^j$ and $D_T$

9:       **if** $V_A{}^j > 0$ and $L_H{}^j < L_{H_{Max}}$ **then**

10:         **Break** $j^{th}$ loop

11:       **end if**

12:     **end for**

13:   **end for**

14: **return** Ids of healed Elements

---

# REFERENCES

[AA18]     A. Abdul-Aziz.    Durability Modeling Review of Thermal- and
           Environmental-Barrier-Coated Fiber-Reinforced Ceramic Matrix Com-
           posites Part I. *Materials (Basel, Switzerland)*, 11(7):1996–1944, 2018.

[AAR15]    A. A. Alsheghri and R. K. A. Al-Rub.  Thermodynamic-based cohesive
           zone healing model for self-healing materials.  *Mechanics Research
           Communications*, 70:102–113, 2015.

[AIL+01]   A. J. Allen, J. Ilavsky, G. G. Long, J. S. Wallace, C. C. Berndt,
           and H. Herman.  Microstructural characterization of yttria-stabilized
           zirconia plasma-sprayed deposits using multiple small-angle neutron
           scattering. *Acta Materialia*, 49(9):1661–1675, 2001.

[ASM05]    J. Aktaa, K. Sfar, and D. Munz.  Assessment of TBC systems failure
           mechanisms using a fracture mechanics approach.  *Acta Materialia*,
           53(16):4399–4413, 2005.

[AST13]    ASTM E647-13. Standard Test Method for Measurement of Fatigue Crack
           Growth Rates. *American Society for Testing and Materials (ASTM)*, 2013.

[AST16]    ASTM C1421-16.  Standard Test Methods for Determination of Fracture
           Toughness of Advanced Ceramics at Ambient Temperature.  *ASTM
           International*, 15:1–33, 2016.

[AVSL04]   M. Ahrens, R. Vaßen, D. Stöver, and S. Lampenscherf.  Sintering and
           creep processes in plasma-sprayed thermal barrier coatings. *Journal of
           Thermal Spray Technology*, 13(3):432–442, 2004.

[BAER00]   M. W. Barsoum, M. Ali, and T. El-Raghy. Processing and characterization
           of $Ti_2AlC$, $Ti_2AlN$, and $Ti_2AlC_{0.5}N_{0.5}$.  *Metallurgical and Materials
           Transactions A: Physical Metallurgy and Materials Science*, 31(7):1857–
           1865, 2000.

[Bar01]    M. W. Barsoum. *Encyclopedia of Materials: Science and Technology ||
           Physical properties of the MAX phases*, volume 1.  Elsevier, Amsterdam,
           2001.

[BBB+10]   T. Beck, M. Białas, P. Bednarz, L. Singheiser, K. Bobzin, N. Bagcivan,
           D. Parkot, T. Kashko, J. Petković, B. Hallstedt, S. Nemna, and J. M.

Schneider. Modeling of coating process, phase changes, and damage of plasma sprayed thermal barrier coatings on ni-base superalloys. *Advanced Engineering Materials*, 12(3):110–126, 2010.

[BBP+19] G. Boissonnet, G. Bonnet, A. Pasquet, N. Bourhila, and F. Pedraza. Evolution of thermal insulation of plasma-sprayed thermal barrier coating systems with exposure to high temperature. *Journal of the European Ceramic Society*, 39(6):2111–2121, 2019.

[BBvdZS18] L. Boatemaa, J. C. Brouwer, S. van der Zwaag, and W. G. Sloof. The effect of the TiC particle size on the preferred oxidation temperature for self-healing of oxide ceramic matrix materials. *Journal of Materials Science*, 53(8):5973–5986, 2018.

[Ben01] M. Bengisu. *Engineering Ceramics*. Springer-Verlag Berlin Heidelberg, 1 edition, 2001.

[BGL05] E. J. Barbero, F. Greco, and P. Lonetti. Continuum damage-healing mechanics with application to self-healing composites. *International Journal of Damage Mechanics*, 14(1):51–81, 2005.

[BHT+08] T. Beck, R. Herzog, O. Trunova, M. Offermann, R. W. Steinbrech, and L. Singheiser. Damage mechanisms and lifetime behavior of plasma-sprayed thermal barrier coating systems for gas turbines - Part II: Modeling. *Surf. Coatings Technol.*, 202(24):5901–5908, 2008.

[Bia08a] M. Białas. Finite element analysis of stress distribution in thermal barrier coatings. *Surface and Coatings Technology*, 202(24):6002–6010, 2008.

[Bia08b] M. Białas. Finite element analysis of stress distribution in thermal barrier coatings. *Surface and Coatings Technology*, 202(24):6002–6010, 2008.

[BKvdZS16] L. Boatemaa, C. Kwakernaak, S. van der Zwaag, and W. G. Sloof. Selection of healing agents for autonomous healing of alumina at high temperatures. *Journal of the European Ceramic Society*, 36(16):4141–4145, 2016.

[BLL94] M. N. Bassim, S. S. Lawrence, and C. D. Liu. Detection of the onset of fatigue crack growth in rail steels using acoustic emission. *Engineering Fracture Mechanics*, 47(2):207–214, 1994.

[BMHM05] M. Białas, P. Majerus, R. Herzog, and Z. Mróz. Numerical simulation of segmentation cracking in thermal barrier coatings by means of cohesive zone elements. *Materials Science and Engineering A*, 412(1-2):241–251, 2005.

[Boy12]  M.P. Boyce.  Advanced industrial gas turbines for power generation. In *Combined Cycle Systems for Near-Zero Emission Power Generation*, pages 44–102. Elsevier, 2012.

[BS10]  L. Banks-Sills.  Update: Application of the Finite Element Method to Linear Elastic Fracture Mechanics. *Applied Mechanics Reviews*, 63(2), 2010.

[BS17]  M. Bäker and P. Seiler.  A guide to finite element simulations of thermal barrier coatings. *Journal of Thermal Spray Technology*, 26(6):1146–1160, 2017.

[BSS15]  J. Bluhm, S. Specht, and J. Schröder.  Modeling of self-healing effects in polymeric composites. *Archive of Applied Mechanics*, 85(9-10):1469–1481, 2015.

[BSW02]  E. N. Brown, N. R. Sottos, and S. R. White.  Fracture testing of a self-healing polymer composite.  *Experimental Mechanics*, 42(4):372–379, 2002.

[BW90]  E. Brühwiler and F. H. Wittmann. The wedge splitting test, a new method of performing stable fracture mechanics tests.  *Engineering Fracture Mechanics*, 35(1-3):117–125, 1990.

[CAHM08]  Weijie R. Chen, R. Archer, X. Huang, and B. R. Marple. TGO growth and crack propagation in a thermal barrier coating. *Journal of Thermal Spray Technology*, 17(5-6):858–864, 2008.

[CAVM04]  F. Cernuschi, S. Ahmaniemi, P. Vuoristo, and T. Mäntylä.  Modelling of thermal conductivity of porous materials: Application to thick thermal barrier coatings. *Journal of the European Ceramic Society*, 24(9):2657–2667, 2004.

[CB05]  S. R. Choi and N. P. Bansal.  Mechanical behavior of zirconia/alumina composites. *Ceramics International*, 31(1):39–46, 2005.

[CB12]  W. Cai and J. Bisschop.  Optical method for measuring slow crack growth in cementitious materials. *Materials and Structures/Materiaux et Constructions*, 45(11):1613–1623, 2012.

[CBCS11]  R. D. S. G. Campilho, M. D. Banea, F. J. P. Chaves, and L. F. M. D. Silva.  EXtended Finite Element Method for fracture characterization of adhesive joints in pure mode I.  *Computational Materials Science*, 50(4):1543–1549, 2011.

[CBM09] F. Cernuschi, P. Bison, and A. Moscatelli. Microstructural characterization of porous thermal barrier coatings by laser flash technique. *Acta Materialia*, 57(12):3460–3471, 2009.

[CBMS08] F. Cernuschi, P. G. Bison, S. Marinetti, and P. Scardi. Thermophysical, mechanical and microstructural characterization of aged free-standing plasma-sprayed zirconia coatings. *Acta Materialia*, 56(16):4477–4488, 2008.

[CGB+13] F. Cernuschi, I. O. Golosnoy, P. Bison, A. Moscatelli, R. Vaßen, H. P. Bossmann, and S. Capelli. Microstructural characterization of porous thermal barrier coatings by IR gas porosimetry and sintering forecasts. *Acta Materialia*, 61(1):248–262, 2013.

[CMB+18] A. L. Carabat, M. J. Meijerink, J. C. Brouwer, E. M. Kelder, J. R. van Ommen, S. van der Zwaag, and W. G. Sloof. Protecting the $MoSi_2$ healing particles for thermal barrier coatings using a sol-gel produced $Al_2O_3$ coating. *Journal of European Ceramic Society*, 38(7):2728–2734, 2018.

[CMÖ+13] N. Curry, N. Markocsan, L. Östergren, XH. Li, and M. Dorfman. Evaluation of the lifetime and thermal conductivity of dysprosia-stabilized thermal barrier coating systems. *Journal of thermal spray technology*, 22(6):864–872, 2013.

[CS01] N. Chawla and YL. Shen. Mechanical Behavior of Particle Reinforced Metal Matrix Composites. *Advanced Engineering Materials*, 3(6):357–370, 2001.

[CSVdB10] M. V. Cid Alfaro, A. S. J. Suiker, C. V. Verhoosel, and R. de Borst. Numerical homogenization of cracking processes in thin fibre-epoxy layers. *European Journal of Mechanics-A/Solids*, 29(2):119–131, 2010.

[CvdZS15] A. L. Carabat, S. van der Zwaag, and W. G. Sloof. Creating a Protective Shell for Reactive $MoSi_2$ Particles in High-Temperature Ceramics. *Journal of American Ceramic Society*, 98(8):2609–2616, 2015.

[CVS04] X. Q. Cao, R. Vaßen, and D. Stoever. Ceramic materials for thermal barrier coatings. *Journal of European Ceramic Society*, 24(1):1–10, 2004.

[CZvdZ+19] Y. Chen, X. Zhang, S. van der Zwaag, W. G. Sloof, and P. Xiao. Damage evolution in a self-healing air plasma sprayed thermal barrier coating containing self-shielding $MoSi_2$ particles. *Journal of American Ceramic Society*, 102(8):4899–4910, 2019.

[Dar13] R. Darolia. Thermal barrier coatings technology: critical review, progress update, remaining challenges and prospects. *International Materials Reviews*, 58(6):315–348, 2013.

[DARL12] M. K. Darabi, R. K. A. Al-Rub, and D. N. Little. A continuum damage mechanics framework for modeling micro-damage healing. *International Journal of Solids and Structures*, 49(3):492–513, 2012.

[DCS+15] Z. Derelioglu, A. L. Carabat, G. M. Song, S. van der Zwaag, and W. G. Sloof. On the use of B-alloyed $MoSi_2$ particles as crack healing agents in yttria stabilized zirconia thermal barrier coatings. *Journal of the European Ceramic Society*, 35(16):4507–4511, 2015.

[DMG94] Jeanine T. DeMasi-Marcin and Dinesh K. Gupta. Protective coatings in the gas turbine engine. *Surface and Coatings Technology*, 68:1–9, 1994.

[DSZ+13] S. Dong, B. Song, G. Zhou, B. Hansz, H. Liao, and C. Coddet. Multi-layered thermal barrier coatings fabricated by plasma-spraying and dry-ice blasting: Microstructure characterization and prolonged lifetime. *Surface and Coatings Technology*, 236:557–567, 2013.

[DYL+14] H. Dong, GJ. Yang, CX. Li, XT. Luo, and CJ. Li. Effect of TGO Thickness on Thermal Cyclic Lifetime and Failure Mode of Plasma-Sprayed TBCs. *Journal of the American Ceramic Society*, 97(4):1226–1232, 2014.

[EC13] E08-Committee. ASTM E399-12e2 Linear-Elastic Plane-Strain Fracture Toughness $K_{Ic}$ of of Metallic Materials. *ASTM International*, 399:1–33, 2013.

[EM12] S. Esna Ashari and S. Mohammadi. Fracture analysis of FRP-reinforced beams by orthotropic XFEM. *Journal of Composite Materials*, 46(11):1367–1389, 2012.

[ERBZK99] T. El-Raghy, M. W. Barsoum, A. Zavaliangos, and S. R. Kalidindi. Processing and mechanical properties of $Ti_3SiC_2$: II, effect of grain size and deformation temperature. *Journal of the American ceramic society*, 82(10):2855–2860, 1999.

[ESB+13] R. Eriksson, S. Sjöström, H. Brodin, S. Johansson, L. Östergren, and XH. Li. Tbc bond coat–top coat interface roughness: Influence on fatigue life and modelling aspects. *Surface and Coatings Technology*, 236:230–238, 2013.

[ET01] H. E. Evans and M. P. Taylor. Diffusion Cells and Chemical Failure of MCrAlY Bond Coats in Thermal-Barrier Coating Systems. *Oxidation of Metals*, 55(1-2):17–34, 2001.

[Eva11] H. E. Evans. Oxidation failure of TBC systems: An assessment of mechanisms. *Surface and Coatings Technology*, 206(7):1512–1521, 2011.

[FJL+14]  X. Fan, W. Jiang, J. Li, T. Suo, T. J. Wang, and R. Xu. Numerical study on interfacial delamination of thermal barrier coatings with multiple separations. *Surface and Coatings Technology*, 244:117–122, 2014.

[FKT+08]  A. Feuerstein, J. Knapp, T. Taylor, A. Ashary, A. Bolcavage, and N. Hitchman. Technical and Economical Aspects of Current Thermal Barrier Coating Systems for Gas Turbine Engines by Thermal Spray and EBPVD: A Review. *Journal of Thermal Spray Technology*, 17(2):199–213, 2008.

[FM12]  S. W. Freiman and J. J. Mecholsky. Fracture Mechanics Tests. In *The Fracture of Brittle Materials*, pages 32–67. John Wiley & Sons, Inc., 2012.

[GGvP15]  F. A. Gilabert, D. Garoz, and W. van Paepegem. Stress concentrations and bonding strength in encapsulation-based self-healing materials. *Materials & Design*, 67:28–41, 2015.

[GGvP17]  F. A. Gilabert, D. Garoz, and W. van Paepegem. Macro-and micro-modeling of crack propagation in encapsulation-based self-healing materials: Application of XFEM and cohesive surface techniques. *Materials & Design*, 130:459–478, 2017.

[Gil00]  R. O. Gilbert, C. J. and Bloyer, D. R. and Barsoum, M. W. and El-Raghy, T. and Tomsia, A. P. and Ritchie. Fatigue-crack growth and fracture properties of coarse and fine-grained $Ti_3SiC_2$. *Scripta Materialia*, 42(8):761–767, 2000.

[GLHW01]  S. Gu, T. J. Lu, D. D. Hass, and H. N.G. Wadley. Thermal conductivity of zirconia coatings with zig-zag pore microstructures. *Acta Materialia*, 49(13):2539–2547, 2001.

[GMLP17]  M. Gupta, N. Markocsan, X. H. Li, and R. L. Peng. Improving the lifetime of suspension plasma sprayed thermal barrier coatings. *Surface and Coatings Technology*, 332:550–559, 2017.

[GNW13]  M. Gupta, P. Nylén, and J. Wigren. A modelling approach to designing microstructures in thermal barrier coatings. *Journal of Ceramic Science and Technology*, 4(2):85–92, 2013.

[GR09]  C. Geuzaine and JF. Remacle. Gmsh: a three-dimensional finite element mesh generator with built-in pre-and post-processing facilities. *International Journal for Numerical Methods in Engineering*, 79(11):1–24, 2009.

[GS06]  I. Gurrappa and A. Sambasiva Rao. Thermal barrier coatings for enhanced efficiency of gas turbine engines. *Surface and Coatings Technology*, 201(6):3016–3029, 2006.

[GVS04] H.B. Guo, R. Vaßen, and D. Stöver. Atmospheric plasma sprayed thick thermal barrier coatings with high segmentation crack density. *Surface and Coatings Technology*, 186(3):353–363, 2004.

[GvTT+17] F. A. Gilabert, K. van Tittelboom, E. Tsangouri, D. van Hemelrijck, N. De Belie, and W. van Paepegem. Determination of strength and debonding energy of a glass-concrete interface for encapsulation-based self-healing concrete. *Cement and Concrete Composites*, 79:76–93, 2017.

[GW11] S. Gong and Q. Wu. Processing, microstructures and properties of thermal barrier coatings by electron beam physical vapor deposition (EB–PVD). In *Thermal Barrier Coatings*, pages 115–131. Woodhead Publishing, 2011.

[GZZ+19] X. Guo, W. Zhao, Y. Zeng, C. Lin, J. Zhang, X. Guo, W. Zhao, Y. Zeng, C. Lin, and J. Zhang. Effects of Splat Interfaces, Monoclinic Phase and Grain Boundaries on the Thermal Conductivity of Plasma Sprayed Yttria-Stabilized Zirconia Coatings. *Coatings*, 9(1):26, 2019.

[HE02] J. W. Hutchinson and A. G. Evans. On the delamination of thermal barrier coatings in a thermal gradient. *Surface and Coatings Technology*, 149(2-3):179–184, 2002.

[Hil09] T.S. Hille. *Lifetime Modeling of Thermal Barrier Coatings*. PhD thesis, Delft university of technology, 2009.

[HL08] O. Herbst and S. Luding. Modeling particulate self-healing materials and application to uni-axial compression. *International Journal of Fracture*, 154(1-2):87–103, 2008.

[HMP76] A. Hillerborg, M. Modéer, and P.-E. Petersson. Analysis of crack formation and crack growth in concrete by means of fracture mechanics and finite elements. *Cement and Concrete Research*, 6(6):773–781, 1976.

[HST09] T. S. Hille, A. S. J. Suiker, and S. Turteltaub. Microcrack nucleation in thermal barrier coating systems. *Engineering Fracture Mechanics*, 76(6):813–825, 2009.

[HTS11] T. S. Hille, S. Turteltaub, and A. S. J. Suiker. Oxide growth and damage evolution in thermal barrier coatings. *Engineering Fracture Mechanics*, 78(10):2139–2152, 2011.

[HWLL18] J. Huang, W. Wang, S. Lu, X.and Liu, and C. Li. Influence of Lamellar Interface Morphology on Cracking Resistance of Plasma-Sprayed YSZ Coatings. *Coatings*, 8(5):187, 2018.

[IRC+91] Y. M. Ito, M. Rosenblatt, L. Y. Cheng, F. F. Lange, and A. G. Evans. Cracking in particulate composites due to thermalmechanical stress. *International Journal of Fracture*, 17(5):483–491, 1991.

[JEY+17] K. P. Jonnalagadda, R. Eriksson, K. Yuan, X. H. Li, X. Ji, Y. Yu, and R. L. Peng. A study of damage evolution in high purity nano TBCs during thermal cycling: A fracture mechanics based modelling approach. *Journal of the European Ceramic Society*, 37(8):2889–2899, 2017.

[JJ14] B. N. Jaya and V. Jayaram. Crack stability in edge-notched clamped beam specimens: Modeling and experiments. *International Journal of Fracture*, 188(2):213–228, 2014.

[Jon97] R. L. Jones. Some aspects of the hot corrosion of thermal barrier coatings. *Journal of Thermal Spray Technology*, 6(1):77–84, 1997.

[KBK17] A. Keyvani, M. Bahamirian, and A. Kobayashi. Effect of sintering rate on the porous microstructural, mechanical and thermomechanical properties of YSZ and CSZ TBC coatings undergoing thermal cycling. *Journal of Alloys and Compounds*, 727:1057–1066, 2017.

[KECK18] U. Klement, J. Ekberg, S. Creci, and S. T. Kelly. Porosity measurements in suspension plasma sprayed YSZ coatings using NMR cryoporometry and X-ray microscopy. *Journal of Coatings Technology and Research*, 15(4):753–757, 2018.

[KJH13] S. Kyaw, A. Jones, and T. Hyde. Predicting failure within TBC system: Finite element simulation of stress within TBC system as affected by sintering of APS TBC, geometry of substrate and creep of TGO. *Engineering Failure Analysis*, 27:150–164, 2013.

[KK16] V. Kumar and B. Kandasubramanian. Processing and design methodologies for advanced and novel thermal barrier coatings for engineering applications. *Particuology*, 27:1–28, 2016.

[KL09] A. N. Khan and J. Lu. Manipulation of air plasma spraying parameters for the production of ceramic coatings. *Journal of Materials Processing Technology*, 209(5):2508–2514, 2009.

[KMZC+16] J. Kulczyk-Malecka, X. Zhang, J. Carr, A. L. Carabat, W. G. Sloof, S. van der Zwaag, F. Cernuschi, F. Nozahic, D. Monceau, C. Estournès, et al. Influence of embedded $MoSi_2$ particles on the high temperature thermal conductivity of SPS produced yttria-stabilised zirconia model thermal barrier coatings. *Surface and Coatings Technology*, 308:31–39, 2016.

[KPTvdZ18]  J. Krishnasamy, S. A. Ponnusami, S. Turteltaub, and S. van der Zwaag. Modelling the fracture behaviour of thermal barrier coatings containing healing particles. *Materials & Design*, 157:75–86, 2018.

[KPTvdZ19]  J. Krishnasamy, S. A. Ponnusami, S. Turteltaub, and S. van der Zwaag. Numerical investigation into the effect of splats and pores on the thermal fracture of air plasma-sprayed thermal barrier coatings. *Journal of Thermal Spray Technology*, 28(8):1881–1892, 2019.

[KSW03]  M. R. Kessler, N. R. Sottos, and S. R. White. Self-healing structural composite materials. *Composites Part A: applied science and manufacturing*, 34(8):743–753, 2003.

[KT80]  B. H. Kear and E. R. Thompson. Aircraft gas turbine materials and processes. *Science*, 208(4446):847–856, 1980.

[KVG+03]  A. Kulkarni, A. Vaidya, A. Goland, S. Sampath, and H. Herman. Processing effects on porosity-property correlations in plasma sprayed yttria-stabilized zirconia coatings. *Materials Science and Engineering A*, 359(1-2):100–111, 2003.

[KVS11]  M. Karger, R. Vaßen, and D. Stöver. Atmospheric plasma sprayed thermal barrier coatings with high segmentation crack densities: Spraying process, microstructure and thermal cycling behavior. *Surface and Coatings Technology*, 206(1):16–23, 2011.

[KWN+03]  A. Kulkarni, Z. Wang, T. Nakamura, S. Sampath, A. Goland, H. Herman, J. Allen, J. Ilavsky, G. Long, J. Frahm, and R. W. Steinbrech. Comprehensive microstructural characterization and predictive property modeling of plasma-sprayed zirconia coatings. *Acta Materialia*, 51(9):2457–2475, 2003.

[LAWDS13]  S. Li, A. Abdel-Wahab, E. Demirci, and V. V. Silberschmidt. Fracture process in cortical bone: X-FEM analysis of microstructured models. *International Journal of Fracture*, 184(1-2):43–55, 2013.

[LDP15]  C. Lamuta, G. Di Girolamo, and L. Pagnotta. Microstructural, mechanical and tribological properties of nanostructured YSZ coatings produced with different APS process parameters. *Ceramics International*, 41(7):8904–8914, 2015.

[Liu97]  D. M. Liu. Influence of porosity and pore size on the compressive strength of porous hydroxyapatite ceramic. *Ceramics International*, 23(2):135–139, 1997.

[LJY⁺18] X. Li, S. Jiang, Y. Ye, S. Liu, Z. Xu, Y. Tan, and D. Yang. Influence of random pore defects on failure mode and mechanical properties of SiC ceramics under uniaxial compression using discrete element method. *Ceramics International*, 44(18):22271–22282, 2018.

[LJYY16] W. Li, Z. Jiang, Z. Yang, and H. Yu. Effective mechanical properties of self-healing cement matrices with microcapsules. *Materials & Design*, 95:422–430, 2016.

[LKK13] I. M. Lancaster, H. A. Khalid, and I. A. Kougioumtzoglou. Extended FEM modelling of crack propagation using the semi-circular bending test. *Construction and Building Materials*, 48:270–277, 2013.

[LMK⁺14] Z. Lu, S. W. Myoung, E. H. Kim, J. H. Lee, and Y. G. Jung. Microstructure evolution and thermal durability with coating thickness in APS thermal barrier coatings. *Materials Today: Proceedings*, 1(1):35–43, 2014.

[LN03] E. Lugscheider and R. Nickel. Finite element simulation of a coating formation on a turbine blade during plasma spraying. *Surface and Coatings Technology*, 174-175:475–481, 2003.

[LPW04] Y. Liu, C. Persson, and J. Wigren. Experimental and numerical life prediction of thermally cycled thermal barrier coatings. *Journal of Thermal Spray Technology*, 13(3):415–424, 2004.

[LS08] S. Luding and A. S. J. Suiker. Self-healing of damaged particulate materials through sintering. *Philosophical Magazine*, 88(28-29):3445–3457, 2008.

[LSK⁺12] S. Li, G. Song, K. Kwakernaak, S. van der Zwaag, and W. G. Sloof. Multiple crack healing of a Ti$_2$AlC ceramic. *Journal of the European Ceramic Society*, 32(8):1813–1820, 2012.

[LW03] A. Liu and Y. Wei. Finite element analysis of anti-spallation thermal barrier coatings. *Surface and Coatings Technology*, 165(2):154–162, 2003.

[LW19] G. R. Li and L. S. Wang. Durable TBCs with self-enhanced thermal insulation based on co-design on macro- and microstructure. *Applied Surface Science*, 483:472–480, 2019.

[LWMF13] L. Lu, FC. Wang, Z. Ma, and QB. Fan. Anisotropic effect of splat interface on thermal conductivity of plasma sprayed YSZ coating. *Surface and Coatings Technology*, 235:596–602, 2013.

[LYC⁺18] G. R. Li, G. J. Yang, X. F. Chen, C. X. Li, and C. J. Li. Strain/sintering co-induced multiscale structural changes in plasma-sprayed thermal barrier coatings. *Ceramics International*, 44(12):14408–14416, 2018.

[LYLL18]   G. R. Li, G. J. Yang, C. X. Li, and C. J. Li. Sintering characteristics of plasma-sprayed TBCs: Experimental analysis and an overall modelling. *Ceramics International*, 44(3):2982–2990, 2018.

[LYS+91]   T. C. Lu, J. Yang, Z. Suo, A. G. Evans, R. Hecht, and R. Mehrabian. Matrix cracking in intermetallic composites caused by thermal expansion mismatch. *Acta Metallurgica et Materialia*, 39(8):1883–1890, 1991.

[LZC+17]   C. Li, X. Zhang, J. Chen, Y.and Carr, S. Jacques, J. Behnsen, M. di Michiel, P. Xiao, and R. Cernik. Understanding the residual stress distribution through the thickness of atmosphere plasma sprayed (APS) thermal barrier coatings (TBCs) by high energy synchrotron XRD; digital image correlation (DIC) and image based modelling. *Acta Materialia*, 132:1–12, 2017.

[MB06]   P. Michlik and C. Berndt. Image-based extended finite element modeling of thermal barrier coatings. *Surface and Coatings Technology*, 201(6):2369–2380, 2006.

[MBF+06]   M. Martena, D. Botto, P. Fino, S. Sabbadini, M. M. Gola, and C. Badini. Modelling of TBC system failure: Stress distribution as a function of TGO thickness and thermal expansion mismatch. *Engineering Failure Analysis*, 13(3):409–426, 2006.

[MG06]   S. Maiti and P. H. Geubelle. Cohesive modeling of fatigue crack retardation in polymers: crack closure effect. *Engineering Fracture Mechanics*, 73(1):22–41, 2006.

[MJR94]   V. Moorthy, T. Jayakumar, and B. Raj. Acoustic emission behaviour during stage II fatigue crack growth in an AISI type 316 austenitic stainless steel. *Bulletin of Materials Science*, 17(6):699–715, 1994.

[MMM+17]   M. Mutter, G. Mauer, R. Mücke, O. Guillon, and R. Vaßen. Correlation of splat morphologies with porosity and residual stress in plasma-sprayed YSZ coatings. *Surface and Coatings Technology*, 318:157–169, 2017.

[MS12]   J. Malzbender and R. W. Steinbrech. Fracture resistance of atmospheric plasma sprayed thermal barrier coatings. *Surface and Coatings Technology*, 209:97–102, 2012.

[MS13]   J. Mergheim and P. Steinmann. Phenomenological modelling of self-healing polymers based on integrated healing agents. *Computational Mechanics*, 52(3):681–692, 2013.

[MTL91]   T. Mochida, M. Taya, and D. J. Lloyd. Fracture of Particles in a Particle/Metal Matrix Composite under Plastic Straining and Its Effect

on the Young's Modulus of the Composite. *Materials Transactions, JIM*, 32(10):931–942, 1991.

[NEC+18]	F. Nozahic, C. Estournès, A. L. Carabat, W. G. Sloof, S. van der Zwaag, and D. Monceau. Self-healing thermal barrier coating systems fabricated by spark plasma sintering. *Materials & Design*, 143:204–213, 2018.

[NME16]	F. Nozahic, D. Monceau, and C. Estournès. Thermal cycling and reactivity of a MoSi$_2$/ZrO$_2$ composite designed for self-healing thermal barrier coatings. *Materials and Design*, 94:444–448, 2016.

[Now14]	Nowak, W. and Naumenko, D. and Mor, G. and Mor, F. and Mack, D. E. and Vaßen, R. and Singheiser, L. and Quadakkers, W. J. Effect of processing parameters on MCrAlY bondcoat roughness and lifetime of APS–TBC systems. *Surface and Coatings Technology*, 260:82–89, 2014.

[NQB00]	T. Nakamura, G. Qian, and C. C. Berndt. Effects of pores on mechanical properties of plasma-sprayed ceramic coatings. *Journal of the American Ceramic Society*, 83(3):578–584, 2000.

[NSRR09]	D. Nunez, K. S. Surana, A. Romkes, and J. N. Reddy. J-integral for mode i linear elastic fracture mechanics in h, p, k mathematical and computational framework. *International Journal of Computational Methods in Engineering Science and Mechanics*, 10(5):345–369, 2009.

[NSSQ09]	D. Naumenko, V. Shemet, L. Singheiser, and W. J. Quadakkers. Failure mechanisms of thermal barrier coatings on MCrAlY-type bondcoats associated with the formation of the thermally grown oxide. *Journal of Material Science*, 44(7):1687–1703, 2009.

[OAO+18]	S. Ozaki, Y. Aoki, T. Osada, K. Takeo, and W. Nakao. Finite element analysis of fracture statistics of ceramics: Effects of grain size and pore size distributions. *Journal of the American Ceramic Society*, 101(7):3191–3204, 2018.

[OFZ+16]	T. Ouyang, X. Fang, Y. Zhang, D. Liu, Y. Wang, S. Feng, T. Zhou, S. Cai, and J. Suo. Enhancement of high temperature oxidation resistance and spallation resistance of SiC-self-healing thermal barrier coatings. *Surface and Coatings Technology*, 286:365–375, 2016.

[OON16]	S. Ozaki, T. Osada, and W. Nakao. Finite element analysis of the damage and healing behavior of self-healing ceramic materials. *International Journal of Solids and Structures*, 100:307–318, 2016.

[OWY+16]	T. Ouyang, J. Wu, M. Yasir, T. Zhou, X. Fang, Y. Wang, D. Liu, and J. Suo. Effect of TiC self-healing coatings on the cyclic oxidation resistance and

lifetime of thermal barrier coatings. *Journal of Alloys and Compounds*, 656:992–1003, 2016.

[PB05]    J. W. C. Pang and I. P. Bond. A hollow fibre reinforced polymer composite encompassing self-healing and enhanced damage visibility. *Composites Science and Technology*, 65(11):1791–1799, 2005.

[PGJ02]   N. P. Padture, M. Gell, and E. H Jordan. Thermal barrier coatings for gas-turbine engine applications. *Science*, 296(5566):280–284, 2002.

[PKTvdZ17] S. A. Ponnusami, J. Krishnasamy, S. Turteltaub, and S. van der Zwaag. A cohesive-zone crack healing model for self-healing materials. *International Journal of Solids and Structures*, 134:249–263, 2017.

[PKTvdZ19] S. A. Ponnusami, J. Krishnasamy, S. Turteltaub, and S. van der Zwaag. A micromechanical fracture analysis to investigate the effect of healing particles on the overall mechanical response of a self-healing particulate composite. *Fatigue & Fracture of Engineering Materials & Structures*, 42(2):533–545, 2019.

[PLH17]   B. A. Pint, M. J. Lance, and J. A. Haynes. The effect of coating composition and geometry on TBC lifetime. *Proceedings of the ASME Turbo Expo*, 6, 2017.

[Pon18]   S. A. Ponnusami. *Modelling fracture and healing in particulate composite systems.* PhD thesis, Delft University of Technology, 2018.

[PTvdZ15] S. A. Ponnusami, S. Turteltaub, and S. van der Zwaag. Cohesive-zone modelling of crack nucleation and propagation in particulate composites. *Engineering Fracture Mechanics*, 149:170–190, 2015.

[PTZX15]  S. A. Ponnusami, S. Turteltaub, X. Zhang, and P. Xiao. Modelling crack propagation in particle-dispersed self-healing thermal barrier coatings. In S. van der Zwaag and E. Brinkman, editors, *Self Healing Materials: Pioneering Research in the Netherlands*, pages 229–241. IOS Press, Netherlands, 2015.

[QGZ$^+$11] X. K. Qian, Y. P. Gan, Y. Zhou, X. D. He, Y. X. Chen, and S. N. Yun. Structural, elastic and electronic properties of a new ternary-layered Ti$_2$SiN. *Physica B: Condensed Matter*, 406(20):3847–3850, 2011.

[QWW$^+$18] X. Qiao, Y. M. Wang, W. X. Weng, B. L. Liu, and Q. Li. Influence of pores on mechanical properties of plasma sprayed coatings: Case study of YSZ thermal barrier coatings. *Ceramics International*, 44:21564–21577, 2018.

[QZR15] M. S. Quayum, X. Zhuang, and T. Rabczuk. Computational model generation and RVE design of self-healing concrete. *Frontiers of Structural and Civil Engineering*, 9(4):383–396, 2015.

[QZvdK13] L. P. Qiu, E. C. Zhu, and J. W. G. van de Kuilen. Modeling crack propagation in wood by extended finite element method. *European Journal of Wood and Wood Products*, 72(2):273–283, 2013.

[RBER$^+$02] M. Radovic, M. W. Barsoum, T. El-Raghy, S. M. Wiederhorn, and W. E. Luecke. Effect of temperature, strain rate and grain size on the mechanical response of $Ti_3SiC_2$ in tension. *Acta materialia*, 50(6):1297–1306, 2002.

[RE00] A. Rabiei and A. G. Evans. Failure mechanisms associated with the thermally grown oxide in plasma-sprayed thermal barrier coatings. *Acta Materialia*, 48(15):3963–3976, 2000.

[RES04] D. Renusch, H. Echsler, and M. Schütze. Progress in life time modeling of APS-TBC part II: Critical strains, macro-cracking, and thermal fatigue. *Materials at High Temperatures*, 21(2):77–86, 2004.

[RfAMS11] M. Ranjbar-far, J. Absi, G. Mariaux, and D. S. Smith. Crack propagation modeling on the interfaces of thermal barrier coating system with different thickness of the oxide layer and different interface morphologies. *Materials & Design*, 32(10):4961–4969, 2011.

[RT03] T. M. Roberts and M. Talebzadeh. Acoustic emission monitoring of fatigue crack propagation. *Journal of Constructional Steel Research*, 59(6):695–712, 2003.

[SAK08] M. Saremi, A. Afrasiabi, and A. Kobayashi. Microstructural analysis of YSZ and $YSZ/Al_2O_3$ plasma sprayed thermal barrier coatings after high temperature oxidation. *Surface and Coatings Technology*, 202(14):3233–3238, 2008.

[SB03] R. W. Steinbrech and D. Basu. Ceramic based Thermal Barrier Coating (TBC) for gas turbine application: Elastic behaviour of plasma sprayed TBC. *Transactions of the Indian Ceramic Society*, 62(4):192–199, 2003.

[ŠFA$^+$16] B. Šavija, J. Feiteira, M. Araújo, S. Chatrabhuti, JM. Raquez, K. van Tittelboom, E.e Gruyaert, N. De Belie, and E. Schlangen. Simulation-aided design of tubular polymeric capsules for self-healing concrete. *Materials*, 10(1):10, 2016.

[SGD15] I. Sabree, J. E. Gough, and B. Derby. Mechanical properties of porous ceramic scaffolds: Influence of internal dimensions. *Ceramics International*, 41(7):8425–8432, 2015.

[SK01]   I. Sevostianov and M. Kachanov.   Plasma-sprayed ceramic coatings: Anisotropic elastic and conductive properties in relation to the microstructure; Cross-property correlations. *Materials Science and Engineering A*, 297(1-2):235–243, 2001.

[Slo]   W. G. Sloof.   Self-Healing Thermal Barrier Coatings for Prolonged Lifetime (funded by EU-FP7).

[Slo07]   W. G. Sloof. Self Healing in Coatings at High Temperatures. In *Springer Series in Materials Science*, pages 309–321. Springer Verlag, 2007.

[Spa20]   Z. S. Spakovszky. Brayton cycle. Massachusetts Institute of Technology:. *Lecture Notes: Thermodynamics and Propulsion retrieved in*, Apr 2020.

[SPJG03]   K. W. Schlichting, N. P. Padture, E. H. Jordan, and M. Gell.   Failure modes in plasma-sprayed thermal barrier coatings. *Materials Science and Engineering A*, 342(1-2):120–130, 2003.

[SPK01]   K. W. Schlichting, N. P. Padture, and P. G. Klemens. Thermal conductivity of dense and porous yttria-stabilized zirconia. *Journal of Materials Science*, 36(12):3003–3010, 2001.

[SPM+16]   W. G. Sloof, R. Pei, S. A. McDonald, J. L. Fife, L. Shen, L. Boatemaa, A. S. Farle, K. Yan, X. Zhang, S. van der Zwaag, P. D. Lee, and P. J. Withers. Repeated crack healing in MAX-phase ceramics revealed by 4D in situ synchrotron X-ray tomographic microscopy. *Scientific Reports*, 6(1):23040, 2016.

[SPS+08]   G. M. Song, Y. T. Pei, W. G. Sloof, S. B. Li, J. T. M. De Hosson, and S. Van der Zwaag. Oxidation-induced crack healing in $Ti_3AlC_2$ ceramics. *Scripta Materialia*, 58(1):13–16, 2008.

[SR06]   E. C. Schimmel and J. J. C. Remmers.   Development of a constitutive model for self-healing materials.   Technical report, Delft Aerospace Computational Science, 2006.

[SRJB07]   T.. Strangman, D. Raybould, A. Jameel, and W. Baker.   Damage mechanisms, life prediction, and development of EB-PVD thermal barrier coatings for turbine airfoils. *Surface and Coatings Technology*, 202(4-7):658–664, 2007.

[SSC13]   KH. Schwalbe, I. Scheider, and A. Cornec. *Guidelines for Applying Cohesive Models to the Damage Behaviour of Engineering Materials and Structures*, volume 53 of *SpringerBriefs in Applied Sciences and Technology*. Springer Berlin Heidelberg, 2013.

[SSFL05]   U. Schulz, B. Saruhan, K. Fritscher, and C. Leyens. Review on Advanced EB-PVD Ceramic Topcoats for TBC Applications. *International Journal of Applied Ceramic Technology*, 1(4):302–315, 2005.

[SSW04]   P. Strunz, R. Schumacher, Gand Vaßen, and A. Wiedenmann. In situ SANS study of pore microstructure in YSZ thermal barrier coatings. *Acta Materialia*, 52(11):3305–3312, 2004.

[STD+15]   W. G. Sloof, S. Turteltaub, Z. Derelioglu, S. A. Ponnusami, and G. Song. Crack healing in yttria stabilized zirconia thermal barrier coatings. In S. van der Zwaag and E. Brinkman, editors, *Self Healing Materials: Pioneering Research in the Netherlands*, pages 219–227. IOS Press, 2015.

[STH+98]   D. Schwingel, R. Taylor, T. Haubold, J. Wigren, and C. Gualco. Mechanical and thermophysical properties of thick PYSZ thermal barrier coatings: correlation with microstructure and spraying parameters. *Surface and Coatings Technology*, 108-109:99–106, 1998.

[SW05]   J. Singh and D. E. Wolfe. Nano and macro-structured component fabrication by electron beam-physical vapor deposition (EB-PVD). *Journal of Materials Science*, 40(1):1–26, 2005.

[SWQ+18]   Y. Song, W. Wu, M. Qin, D. Li, Y. Liu, S. Ai, and TJ. Wang. Effect of geometric parameter on thermal stress generation in fabrication process of double-ceramic-layers thermal barrier coating system. *Journal of the European Ceramic Society*, 38(11):3962–3973, 2018.

[SWS02]   Jogenden Singh, Douglas E. Wolfe, and Jason Singh. Architecture of thermal barrier coatings produced by electron beam-physical vapor deposition (EB-PVD). *Journal of Materials Science*, 37(15):3261–3267, 2002.

[SYZ+17]   Q. Shen, L. Yang, Y. C. Zhou, Y. G. Wei, and N. G. Wang. Models for predicting TGO growth to rough interface in TBCs. *Surface and Coatings Technology*, 325:219–228, 2017.

[TBH+08]   O. Trunova, T. Beck, R. Herzog, R. W. Steinbrech, and L. Singheiser. Damage mechanisms and lifetime behavior of plasma sprayed thermal barrier coating systems for gas turbines—Part I: Experiments. *Surface and Coatings Technology*, 202(20):5027–5032, 2008.

[THKY90]   M. Taya, S. Hayashi, A. S. Kobayashi, and H. S. Yoon. Toughening of a Particulate-Reinforced Ceramic-Matrix Composite by Thermal Residual Stress. *Journal of the American Ceramic Society*, 73(5):1382–1391, 1990.

[TSBA00]   G. Thurn, G. A. Schneider, H. A. Bahr, and F. Aldinger. Toughness anisotropy and damage behavior of plasma sprayed $ZrO_2$ thermal barrier coatings. *Surface and Coatings Technology*, 123(2-3):147–158, 2000.

[Tsc86]   E. K. Tschegg. Equipment and appropriate specimen shapes for tests to measure fracture values. *Patent AT-390328*, 1986.

[TVG+06]   J. Toscano, R. Vaßen, A. Gil, M. Subanovic, D. Naumenko, L. Singheiser, and W. J. Quadakkers. Parameters affecting TGO growth and adherence on MCrAlY-bond coats for TBC's. *Surface and Coatings Technology*, 201:3906–3910, 2006.

[UKP09]   A. Ural, V. R. Krishnan, and K. D. Papoulia. A cohesive zone model for fatigue crack growth allowing for crack retardation. *International Journal of Solids and Structures*, 46(11):2453–2462, 2009.

[vdZB15]   S. van der Zwaag and E. Brinkman, editors. *Self Healing Materials: Pioneering Research in the Netherlands*. IOS Press, 2015.

[VGS09]   R. Vaßen, S. Giesen, and D. Stöver. Lifetime of plasma-sprayed thermal barrier coatings: Comparison of numerical and experimental results. *Journal of Thermal Spray Technology*, 18(5-6):835–845, 2009.

[VKS01]   R. Vaßen, G. Kerkhoff, and D. Stöver. Development of a micromechanical life prediction model for plasma sprayed thermal barrier coatings. *Materials Science and Engineering: A*, 303(1-2):100–109, 2001.

[VKS+10]   R. Vaßen, H. Kassner, A. Stuke, D. E. Mack, M. O. Jarligo, and D. Stöver. Functionally graded thermal barrier coatings with improved reflectivity and high-temperature capability. *Materials Science Forum*, 631-632:73–78, 2010.

[VSL11]   G. Z. Voyiadjis, A. Shojaei, and G. Li. A thermodynamic consistent damage and healing model for self healing materials. *International Journal of Plasticity*, 27(7):1025–1044, 2011.

[VSLK12]   G. Z. Voyiadjis, A. Shojaei, G. Li, and P. I. Kattan. A theory of anisotropic healing and damage mechanics of materials. *Proceedings of the Royal Society A: Mathematical, Physical and Engineering Sciences*, 468(2137):163–183, 2012.

[VSS09]   R. Vaßen, A. Stuke, and D. Stöver. Recent developments in the field of thermal barrier coatings. *Journal of Thermal Spray Technology*, 18(2):181–186, 2009.

[WFL+15]  L. Wang, Q. Fan, Y. Liu, G. Li, H. Zhang, Q. Wang, and F. Wang. Simulation of damage and failure processes of thermal barrier coatings subjected to a uniaxial tensile load. *Materials and Design*, 86:89–97, 2015.

[WJP16]  T. Whitlow, E. Jones, and C. Przybyla. In-situ damage monitoring of a SiC/SiC ceramic matrix composite using acoustic emission and digital image correlation. *Composite Structures*, 158:245–251, 2016.

[WKD+03]  Z. Wang, A. Kulkarni, S. Deshpande, T. Nakamura, and H. Herman. Effects of pores and interfaces on effective properties of plasma sprayed zirconia coatings. *Acta Materialia*, 51(18):5319–5334, 2003.

[WKG02]  Donald E. Wroblewski, Rajesh Khare, and Michael Gevelber. Solidification Modeling of Plasma Sprayed TBC: Analysis of Remelt and Multiple Length Scales of Rough Substrates. *Journal of Thermal Spray Technology*, 11(2):266–275, 2002.

[WLY+16]  L. Wang, D. C. Li, J. S. Yang, F. Shao, X. H. Zhong, H. Y. Zhao, K. Yang, S. Y. Tao, and Y. Wang. Modeling of thermal properties and failure of thermal barrier coatings with the use of finite element methods: A review. *Journal of the European Ceramic Society*, 36(6):1313–1331, 2016.

[WMS04]  T. Wakui, J. Malzbender, and R. W. Steinbrech. Strain analysis of plasma sprayed thermal barrier coatings under mechanical stress. *Journal of Thermal Spray Technology*, 13(3):390–395, 2004.

[WSZ+18]  L. Wang, F. Shao, X. H. Zhong, J. X. Ni, K. Yang, S. Y. Tao, and Y. Wang. Tailoring of self-healing thermal barrier coatings via finite element method. *Applied Surface Science*, 431:60–74, 2018.

[WTB07]  G. Williams, R. Trask, and I. Bond. A self-healing carbon fibre reinforced polymer for aerospace applications. *Composites Part A: Applied Science and Manufacturing*, 38(6):1525–1532, 2007.

[WWS+11]  L. Wang, Y. Wang, X. G. Sun, J. Q. He, Z. Y. Pan, Y. Zhou, and P. L. Wu. Influence of pores on the thermal insulation behavior of thermal barrier coatings prepared by atmospheric plasma spray. *Materials and Design*, 32(1):36–47, 2011.

[WZ13]  X. Wang and Y. Zhou. Solid-Liquid Reaction Synthesis and Simultaneous Densification of Polycrystalline $Ti_2AlC$ . *Zeitschrift für Metallkunde*, 93(1):66–71, 2013.

[XK11]  J. L. Xu and K. A. Khor. Plasma spraying for thermal barrier coatings: processes and applications. In *Thermal Barrier Coatings*, pages 99–114. Woodhead Publishing, 2011.

[XRH+18]  Y. Xiao, E. Ren, M. Hu, K. Liu, Y. Xiao, E. Ren, M. Hu, and K. Liu. Effect of Particle In-Flight Behavior on the Microstructure and Fracture Toughness of YSZ TBCs Prepared by Plasma Spraying. *Coatings*, 8(9):309, 2018.

[XSKZ14]  W. Xu, X. Sun, B. J. Koeppel, and H. M. Zbib. A continuum thermo-inelastic model for damage and healing in self-healing glass materials. *International Journal of Plasticity*, 62:1–16, 2014.

[XY09]  Y. Xu and H. Yuan. Computational analysis of mixed-mode fatigue crack growth in quasi-brittle materials using extended finite element methods. *Engineering Fracture Mechanics*, 76(2):165–181, 2009.

[Yam08]  Y. Yamazaki. Correlation between the Mechanical Properties and Splat Microstructures of an Air Plasma Sprayed Thermal Barrier Coating. *Journal of Solid Mechanics and Materials Engineering*, 2(10):1275–1286, 2008.

[YCH+08]  F. H. Yuan, Z. X. Chen, Z. W. Huang, Z. G. Wang, and S. J. Zhu. Oxidation behavior of thermal barrier coatings with HVOF and detonation-sprayed NiCrAlY bondcoats. *Corrosion Science*, 50(6):1608–1617, 2008.

[YL97]  D. Yi and C. Li. $MoSi_2$ - $ZrO_2$ composites-fabrication, microstructures and properties. *Doktorsavhandlingar vid Chalmers Tekniska Hogskola*, 261(1328):89–98, 1997.

[YWD+13]  X. S. Yang, J. Wan, C. Y. Dai, Y. Zhang, W. G. Mao, Y. C. Zhou, and C. Lu. Finite element analysis of crack propagation and fracture mechanical properties of freestanding 8wt.% $Y_2O_3$-$ZrO_2$ coatings. *Surface and Coatings Technology*, 223:87–91, 2013.

[YZW+17]  M. Yang, Y. Zhu, X. Wang, S. Guo, J. Hu, L. Zhao, and Y. Chu. Effect of five kinds of pores shape on thermal stress properties of thermal barrier coatings by finite element method. *Ceramics International*, 43(13):9664–9678, 2017.

[ZBT+18]  D. F. Zambrano, A. Barrios, L. E. Tobón, C. Serna, P. Gómez, J. D. Osorio, and A. Toro. Thermal properties and phase stability of Yttria-Stabilized Zirconia (YSZ) coating deposited by Air Plasma Spray onto a Ni-base superalloy. *Ceramics International*, 44(4):3625–3635, 2018.

[ZD05]  J. Zhang and V. Desai. Evaluation of thickness, porosity and pore shape of plasma sprayed TBC by electrochemical impedance spectroscopy. *Surface and Coatings Technology*, 190(1):98–109, 2005.

[ZJV11]    S. V. Zemskov, H. M. Jonkers, and F. J. V.  Two analytical models for the probability characteristics of a crack hitting encapsulated particles: Application to self-healing materials. *Computational Materials Science*, 50(12):3323–3333, 2011.

[ZKS⁺01]   Z. Zhang, J. Kameda, A. H. Swanson, S. Sakurai, and M. Sato.  Effects of porosity and thermal ageing on in-plane cracking behavior of thermal barrier coatings.  In W. J. Meng, A. Kumar, G. L. Doll, Y. T. Cheng, S. Veprek, and Y. W. Chung, editors, *Surface Engineering 2001 - Fundamentals and Applications*, volume 697, pages 95–100. Materials Research Society, 2001.

[ZYG⁺15]   W. Zhu, L. Yang, J. W. Guo, Y. C. Zhou, and C. Lu.  Determination of interfacial adhesion energies of thermal barrier coatings by compression test combined with a cohesive zone finite element model. *International Journal of Plasticity*, 64:76–87, 2015.

[ZYW10]   H. Zhao, Z. Yu, and H. NG. Wadley. The influence of coating compliance on the delamination of thermal barrier coatings. *Surface and Coatings Technology*, 204(15):2432–2441, 2010.

[ZZY⁺15]   H. Zhu, S. Zhou, Z. Yan, J. W. Ju, and Q. Chen.  A two-dimensional micromechanical damage-healing model on microcrack-induced damage for microcapsule-enabled self-healing cementitious composites under tensile loading. *International Journal of Damage Mechanics*, 24(1):95–115, 2015.

# SUMMARY

Thermal Barrier Coating (TBC) systems are protective layers applied to critical structural components of gas turbines operating at high-temperature. A typical TBC system consists of three different layers, namely a ceramic Top Coat (TC), an active Thermally Grown Oxide (TGO) layer and a metallic Bond Coat (BC). The outer ceramic TC that protects the substrate from high temperature gases and an intermediate BC acts as a bonding layer and also provides oxidation resistance to the underlying components by acting as a sacrificial layer. As a result of the oxidation process, TGO layer is formed at the interface between the TC and BC layer. Lifetime of a typical system lies around several hundred cycles after which, a cost and time intensive maintenance operation is necessary to replace the coating in order to continue safe operation of the engine. Earlier research on TBC micromechanical studies have been focussed on evaluating the influence of microstructure on thermo-mechanical properties or stress distribution in the TBC system. Numerical efforts on TBC failure such as modelling the different coating composition, TGO growth process and interface irregularities have been made in the past to predict its influence on lifetime of the TBC system. In this research, microstructural features and a novel self healing TBCs are explored through numerical simulations to predict its lifetime enhancement. The overall objective of this research is to develop a modelling and analysis tool capable of simulating fracture and healing processes in the TBC system. The resulting numerical tool aids in setting up design guidelines for the successful development of the proposed self healing TBC system.

Chapter 1: A brief introduction to Thermal Barrier Coatings (TBC) is presented. Morphology and microstructure of the TBC system associated with the deposition process and major failure mechanisms are explained briefly. Subsequently, the proposed concept of self healing TBC system to extend the life time are discussed, followed by the research objective and modelling approach of the present work. The chapter closes with the outline of the thesis.

Chapter 2: The effect of microstructural porosity on the fracture behavior of the TBC is analyzed using a cohesive elements-based finite element method. A concurrent multiscale approach is utilised whereby the microstructural features of the TBC are explicitly resolved within a computational cell embedded in a larger domain. Within the computational cell, a random distribution of pores is modelled along different layers within the TBC system. Geometric and material parameters such as TGO thickness, pore characteristics (such as aspect ratio, size, volume fraction and

orientation), and TC fracture properties are studied through parametric analyses. The results of the parametric studies are reported in terms of the crack initiation temperature and total crack length, whereby several pore features were found to exhibit a significant influence on the failure behavior. Insights derived from the numerical results can help in understanding the failure behavior of practical TBC systems and further aid in engineering the TBC microstructure for a desired fracture behavior.

Chapter 3: In this chapter, the microstructure specific to the Air Plasm Sprayed (APS) TBC such as splats and pores are modelled explicitly using cohesive elements based finite element method in order to predict its influence on the fracture behavior of the APS TBC system. Splats are modelled as being located on a sinusoidal interface in combination with a random distribution of pores. The influence of splat geometric characteristics (such as the roughness of the planes in which the splats are located and their spacing), porosity and splat material parameter (fracture properties) on TBC fracture behavior are studied systematically. It is found that both the splat boundaries and pores plays a significant role in determining failure characteristics. The results and insights from this study aid in optimizing the processing and spraying parameters for improved performance/lifetime of APS TBCs .

Chapter 4: In chapters 2 and 3 the fracture behavior of conventional TBC system is analyzed extensively. The objective of this chapter is to simulate the fracture evolution in TBC systems with embedded solid healing particles using finite element analysis. Simulations are carried out to investigate the effect of geometric and material properties of the healing particles on the crack pattern. Two different configurations of the unit-cell based TBC were analysed, one with a single pair of healing particles and the other with a random distribution of healing particles. The effects of CTE and strength mismatch between the particles and the TC layer were studied using parametric simulations. Correlations are established between the results obtained from the two simulation setups essentially revealing the effect of spatial distribution and proximity of healing particles on the fracture pattern. The results obtained from the analyses can be utilised to achieve a robust design of a self-healing TBC system.

Chapter 5: In this chapter, a generalized cohesive zone based crack healing model is developed, which can be applied for both intrinsic and extrinsic self-healing materials. A cohesive zone-based fracture mechanics model is extended to model both the fracture and the healing in a unified constitutive relation. The model is capable of simulating property recovery after multiple healing events and is also able to handle different fracture properties for the healing material as compared to that of the original material. The healing kinetics of a material can be coupled to the present model through fracture properties and crack filling behavior to simulate specific materials. Significant features of the healing model are illustrated through

the application of the model to a single particle based self-healing material system. It is shown that the model is suitable for analyzing and optimizing self healing TBCs or for designing new self-healing materials with improved lifetime characteristics based on multiple healing events.

Chapter 6: In this chapter, the modelling ingredients developed and discussed in the previous chapters are combined together to obtain a simulation framework for analysing the lifetime (i.e, the number of cycles to coating debonding) of the TBC systems with or without healing particles. In particular, the enhancement in the lifetime of the self-healing TBC system is quantified and compared with the lifetime of a conventional TBC system. Simulations are carried out on a self healing TBC model with a random distribution of healing particles subjected to a numerically accelerated thermal cyclic loading condition. Lifetime extension of the self healing TBCs is quantified by conducting the thermal cyclic analysis on conventional (benchmark) TBCs. Parametric analysis of healing parameters such as crack filling ratio and strength recovery of the healed crack are also conducted. The results are presented in terms of final crack patterns and number of cycles to failure. The simulations results provide a design targets on healing particle distribution and healing parameters for efficient design of self healing TBC system

Appendix A: In a different context, this chapter discusses a simulation-based approach to extract both fracture strength and energy of (semi-) brittle (metallo-) ceramics from experimental data. A new chevron-notched, wedge-loaded specimen and testing method is proposed to retrieve the intrinsic fracture properties from semi-brittle materials using matching finite element calculations based on cohesive zone elements. The combination of a simple test setup and advanced simulations allows unique and accurate determination of both the crack initiation and the crack propagation properties of (semi-) brittle materials.

# SAMENVATTING

Thermal Barrier Coatings (TBCs) zijn beschermende lagen die aangebracht worden op de kritische onderdelen van gas turbines die op hoge temperatuur moeten functioneren. Een TBC systeem bestaat gebruikelijk uit drie verschillende lagen: een keramische toplaag (Top Coat, TC), een ter plaatse gegroeide laag (Thermally Grown Oxide , TGO) bestaande uit metaaloxides en een metallische hechtingslaag (Bond coat, BC). De keramische TC buitenlaag beschermt het substraat tegen de hete en agressieve gassen. De hechtlaag (BC) zorgt voor hechting van het coating systeem aan de metallische turbine bladen en levert ook bescherming tegen inwendige oxidatie door het afstaan van specifieke legeringselementen. Dit oxidatieproces is verantwoordelijk voor de vorming van de TGO-laag tussen de TC en de BC. De levensduur van een turbine motor ligt meestal op een paar honderd cycli, waarna een dure en tijdrovende reparatie nodig is om de beschadigde coating te vervangen en veilig verder functioneren van de motor te kunnen waarborgen. Eerdere micro-mechanische studies aan TBCs waren gericht op het bereken van het effect van TBC samenstelling op hun thermo-mechanisch gedrag of op het berekenen van de inwendige spanningen. In het verleden zijn ook numerieke studies uitgevoerd om de levensduur van een TBC systeem als functie van de opbouw van de coating, de TGO groeikinetiek en oneffenheden aan het oppervlak te kunnen voorspellen. In het onderzoek zoals beschreven in dit proefschrift zijn micro-mechanische modellen ontwikkeld waarmee de effecten van kenmerkende microstructurele aspecten van conventionele en nieuw te ontwikkelen zelfherstellende TBC's op de levensduur van het systeem in kaart gebracht kunnen worden. Het uiteindelijke doel van dit onderzoek is het creëren van numerieke modellen voor zowel het ontstaan van de schade als het verdwijnen ervan door een zelfherstellende reactie tijdens de opgelegde thermische cycli. Het numerieke model wordt daarmee een instrument voor de ontwikkeling van nieuwe zelfherstellende TBCs op basis van discrete reactieve deeltjes.

Hoofdstuk 1: De geeft een beknopte inleiding in Thermal Barrier Coatings (TBCs). De morfologie en de microstructuur van een TBC wordt kort uitgelegd en gekoppeld aan het depositieproces. Ook worden de meest gangbare bezwijkmechanismes besproken. Daarna word het onderliggende concept van de zelfherstellende coating en de beoogde levensduurverlenging uitgelegd. Ook de doelstellingen van het werk en de gekozen aanpak worden er gepresenteerd. Het hoofdstuk sluit af met een schets van de opbouw van het proefschrift.

Hoofdstuk 2: Het effect van porositeit op het lokale breukgedrag wordt geanalyseerd met behulp van een eindige-elementen methode gebaseerd op cohesieve grenslaag elementen. Een 'concurrent multi-scale' benadering wordt gebruikt waarbij de kenmerkende microstructuren van de TBC expliciet gemodelleerd worden en dat binnen een ruimtelijk gebied omringd door een passend continuüm. Binnen dat gebied zijn de poriën willekeurig, maar wel min of meer laagsgewijs, verdeeld over de ruimte. Het effect van diverse aspecten zoals TGO dikte en porie-kenmerken, zoals onrondheid, afmeting, volume fractie en voorkeursoriëntatie, op het lokale breukgedrag zijn bestudeerd door stapsgewijze variaties in de waardes van de ingangsparameters. De resultaten worden uitgedrukt in twee kentallen: de starttemperatuur voor scheurvorming en de totale scheurlengte. Gevonden is dat poriën een groot effect hebben op beide kentallen hebben. De verkregen inzichten zijn nuttig voor het analyseren van breuken in bestaande TBCs en om te voorspellen welke TBC opbouw aanleiding zal geven tot de ontwikkeling van gunstiger scheurpatronen.

Hoofdstuk 3: In dit hoofdstuk, gaat vooral in op het effect van de kenmerkende microstructuur van TBCs welke door plasma spuiten onder atmosferische (APS) condities verkregen worden. Het gaat daarbij om 'splats' (grenslagen tussen opeenvolgende platgeslagen druppels gesmolten TBC materiaal) en poriën en hun effect op het breukgedrag. De 'splats' en de poriën liggen op sinusvormige vlakken. In de berekeningen werden de hoogte en de lengte van het sinusvormige patroon, de poriekenmerken en de breukweerstand van het matrix materiaal gevarieerd. Uit de resultaten bleek dat zowel de 'splats' als de poriën een belangrijke rol in het uiteindelijke breukgedrag spelen. Deze inzichten helpen om de depositiecondities tijdens het plasma spuiten zo te kunnen instellen, dat een langere levensduur verkregen wordt.

Hoofdstuk 4: Terwijl in de voorafgaande hoofdstukken het bezwijkgedrag van standaard TBC coatings onder cyclische thermische belasting onderzocht werd, richt hoofdstuk 4 zich op het gedrag van TBC's met daarin discrete vaste deeltjes die, eenmaal in contact met een lokale scheur, een (zelf-)herstellende reactie op die scheur kunnen hebben. Eindige-elementen simulaties zijn uitgevoerd om het effect van topologie en materiaalkenmerken op het scheurgedrag te kunnen kwantificeren. Twee configuraties zijn daarbij in detail onderzocht: één waarbij twee deeltjes in het gemodelleerde volume aanwezig waren en één met meerdere deeltjes. De onderzochte variabelen in deze simulaties waren de verschillen in uitzettingscoëfficiënt en het verschil in sterkte tussen de deeltjes en het TBC materiaal. Door beide studies te correleren kon het effect van de ruimtelijke ordening van de deeltjes en in het bijzonder de nabijheid van twee deeltjes uit de totale populatie op het uiteindelijke breukgedrag afgeleid worden. De resultaten van deze analyse zijn nuttige voor het topologisch optimaliseren van het ontwerp van nieuwe zelfherstellende TBC systemen.

Hoofdstuk 5: In dit hoofdstuk, wordt een generiek breuk&herstel model gebaseerd op een cohesieve grenslaagelementen gepresenteerd, dat toegepast kan worden op zowel intrinsiek- als extrinsiek-zelfherstellende materialen. De elementen kunnen op een coherente manier toegepast worden voor zowel het breuk- als het herstelgedrag. Het model is ook in staat het gedrag na meerdere breuk&herstel acties te voorspellen, waarbij zelfs de eigenschappen van het materiaal waarmee de scheur gevuld wordt anders kunnen zijn dan het originele matrix materiaal. Door ook de kinetiek van de herstelreactie in rekening te brengen kan het breuk&herstel gedrag van nieuw te onderzoeken materialen en materiaalcombinaties in detail voorspeld worden. De mogelijkheden van het model zijn voor het geval van één deeltje per gemodelleerd volume verder uitgewerkt en gedemonstreerd. Het model is een belangrijke stap in de modelgebaseerde ontwikkeling van nieuwe zelfherstellende TBC systemen.

Hoofdstuk 6: In dit hoofdstuk, worden de eerder ontwikkelde en beschreven ingrediënten gecombineerd om te komen tot een geïntegreerd model voor het analyseren van de levensduur (d.w.z. het aantal thermische cycli tot het loslaten van de coating) van TBC systemen zonder of met 'healing' deeltjes. Daarbij is met name gekeken of en in welke mate de toevoeging van deeltjes leidt tot een verlenging of verkorting van de levensduur. Hiertoe zijn simulaties uitgevoerd waarbij meerdere deeltjes op enige afstand tot het TGO grensvlak in de matrix aanwezig waren. Speciale aandacht is besteed aan het kwantificeren van het effect van de mate waarin de scheur door het zelfherstellende reactie gevuld werd en dat van de relatieve sterkte van het materiaal in de herstelde scheur. De berekende scheurpatronen worden beschreven in termen van totale scheurlengte en aantal cycli tot complete delaminatie van de TBC. De berekeningen geven de materiaalontwerpers kwantitatieve eisen voor de optimale ruimtelijk verdeling van de deeltjes alsmede van het gewenste gedrag per deeltje.

Appendix A: Die een beetje buiten het onderzoeksveld van dit proefschrift valt, beschrijft een methode om zowel de breuksterkte als de breukenergie van zelfherstellend metallo-keramiek in zowel de originele toestand als na breuk&herstel uit experimentele data te bepalen middels specifieke simulaties. Daarmee valt dit deelonderzoek buiten het hoofdthema van het proefschrift. Het betreft een nieuwe breukmechanische set-up, waarbij een wig in een voorgevormde scheur gedrukt wordt, en aandrukkracht, wigverplaatsing en scheurlengte gelijktijdig gemeten worden. Door de experimentele resultaten te combineren met die van simulaties waarin specifieke materiaaleigenschappen gevarieerd worden, kunnen op unieke en nauwkeurige wijze zowel de kentallen voor scheurinitiatie als voor scheuruitbreiding bepaald worden.

# CURRICULUM VITAE

**Jayaprakash Krishnasamy** was born in Namakkal district in the southern Indian state, Tamil Nadu in the year 1987. After his school education, he went on to pursue a Bachelor of Engineering degree in Aeronautics at Anna University to become the first college graduate in his family. Having graduated with his Bachelor's degree in 2009, he got qualified in Graduate Aptitude Test in Engineering (GATE) examination in 2010 with an All India Rank of 75, which is a national level competitive entrance examination for admission into India's premier engineering institutes. Subsequently, he got admission for Master's program in Aerospace Engineering in India's premier research institute, Indian Institute of Technology, Bombay (IITB) in the Department of Aerospace Engineering. After his graduation, he started working as a Structural Engineer (2012-2014) in Airbus Defense & Space, Bangalore, India. During his tenure at IITB and Airbus, he gradually developed an interest in the field of computational structural mechanics. At the beginning of 2014, he got an opportunity to conduct his doctoral research at the Delft University of Technology in the Faculty of Aerospace Engineering.

# ACKNOWLEDGEMENTS

I would like to take this opportunity to thank for the support I received from the Aerospace Structures and Computational Mechanics group at the Faculty of Aerospace Engineering at Delft University of Technology

I would like to express my sincere gratitude to my supervisor Dr Sergio Turteltaub for his mentorship and guidance throughout the research. I would always cherish the abundant time we spent discussing ideas, some great, some good and rest forgotten. Of his many admirable qualities, his pedagogical approach of explaining complex ideas from basic concepts and attention to detail are somethings that I want to emulate. Beyond our professional relationship, I am also quite fond of our many worldly conversations.

I would like to thank my promotor Prof. dr. Sybrand van der Zwaag. I benefited immensely from his motivation. I am grateful for his help in structuring my thesis and innumerable advice in both the technical and personal front. From him, I would like to inherit the invaluable time management skills.

Thanks to my colleagues and group members Wei Ling, Daniel, Zhi, Jaco for all the social breaks and a fun work environment. Prof. dr. Jan Hol thank you for your support in Abaqus licensing and cluster access. Laura, thank you for your help with all administrative matters.

I would like to acknowledge the financial support provided by the European Union's seventh framework program (FP7) through the NMP SAMBA project (grant number 309849). I extend my sincere thanks to our collaborator and SAMBA program leader Dr W.G. Sloof for his valuable support and interactive discussions.

I would like to thank my roommates and friends for making my life in the Netherlands a fond memory. Sekase, Chetase, Bangase, Thagapps, Wasim, Shaafi, Kamalesh, Krishnamoorthy, Anand, kutty Satish, Vishal, Balaji G, Sanjay, Stephen, Gurunathar, Balaji R, Sandeep, Vivek, Yasser, Murali, Mohan, Mohan anna, Prasanna, Nishant thank you all and lots of love and success in your future endeavours. Thanks in particular to Kamal anna and periya Sathis (my financier :P ) for their generous help and support. Thanks to Christa and Jan for the quality time we spent in Pijnacker.

Special mention to Dr SathisKumar A. Ponnusami(AP), for your invaluable guidance and motivation during my hard times. Throughout our 15-year-old friendship, we have our share of memories; good and bad which I treasure. Hopefully, this lasts our lifetime.

I am extremely grateful to my mom, Jayalakshmi, and my sister, Jayapriya, for their unconditional love and support, without which I wouldn't be where I am today. I am thankful to my in-laws Jayaraj and Jayammal for their ample support. My best friend,

my confidant and love of my life Tamil Illakkiya, who has been there for my ups and downs. Now married and with a beautiful son together, I hope we have a fulfilling life together. Thank you for loving our son twice as hard to make up for me. Finally, my son Ezhil Mugilan, I am sorry that I missed your childhood. I love you immensely and I hope to make up for the lost time.

<div align="right">
Jayaprakash Krishnasamy

Delft,
</div>

# PAPERS AND CONFERENCE PRESENTATIONS

**Journal articles**:

1. J. Krishnasamy, S. A. Ponnusami, S. Turteltaub, S. van der Zwaag. Numerical Investigation into the Effect of Splats and Pores on the Thermal Fracture of Air Plasma-Sprayed Thermal Barrier Coatings. Journal of Thermal Spray Technology. 2019 Dec 1;28(8):1881-92.

2. J. Krishnasamy, S. A. Ponnusami, S. Turteltaub, S. van der Zwaag. Computational investigation of porosity effects on fracture behavior of thermal barrier coatings. Ceramics International. 2019 Nov 1;45(16):20518-27.

3. J. Krishnasamy, S. A. Ponnusami, S. Turteltaub, S. van der Zwaag. Modelling the fracture behaviour of thermal barrier coatings containing healing particles. Materials & Design. 2018 Nov 5;157:75-86.

4. J. Krishnasamy, S. A. Ponnusami, S. Turteltaub, S. van der Zwaag. Thermal cyclic behavior and life time prediction of Self healing Thermal Barrier Coatings, Submitted to International Journal of Solids and Structures.

5. S. A. Ponnusami, J. Krishnasamy, S. Turteltaub, S. van der Zwaag. Assessment of crack driving force in a particulate system using configurational forces- Effect of cohesive zone length scale, article in preparation

6. S. A. Ponnusami, J. Krishnamsamy, S. Turteltaub, S. van der Zwaag. Microstructure-based simulations to quantify the effect of healing particles on mechanical properties of self-healing materials, Fatigue & Fracture of Engineering Materials & Structures. 2019 Feb;42(2):533-45.

7. A. S. Farle, J. Krishnasamy, S. Turteltaub,C. Kwakernaak, S. van der Zwaag, W. G. Sloof. Determination of fracture strength and fracture energy of (metallo-) ceramics by a wedge loading methodology and corresponding cohesive zone-based finite element analysis. Engineering Fracture Mechanics. 2018 Jun 1;196:56-70.

8. S. A. Ponnusami, J. Krishnamsamy, S. Turteltaub, S. van der Zwaag.A cohesive-zone crack healing model for self-healing materials. International Journal of Solids and Structures. 2018 Mar 1;134:249-63.

9. J. Krishnasamy, Muthukumar M, Desai YM, Naik NK. Vibration Induced Fatigue Analysis of [0n/90n] s Simply Supported Composite Plate Under Central Patch Impulse Loading. Journal of Engineering Materials and Technology. 2015 Oct 1;137(4).

10. J. Krishnasamy, Desai YM, Naik NK. Fatigue behavior of [0n/90n] s composite cantilever beam under tip impulse loading. Composite Structures. 2013 May 1;99:255-63.

11. Vinayak BG, J. Krishnasamy, Naik NK. Fatigue behavior of laminated composites with a circular hole under in-plane uniaxial random loading. Materials & Design. 2012 Sep 1;40:245-56.

12. Satapathy MR, Vinayak BG, J. Krishnasamy, Naik NK. Fatigue behavior of laminated composites with a circular hole under in-plane multiaxial loading. Materials & Design. 2013 Oct 1;51:347-56.

**International Conference Presentations & Proceedings**:

1. J. Krishnasamy, S. A. Ponnusami, S. Turteltaub, S. van der Zwaag. "Life time prediction of Self healing Thermal Barrier Coatings", 7th International Conference on Self-Healing Materials ICSHM2019, Yokohama, Japan, June 2019.

2. J. Krishnasamy, S. A. Ponnusami, S. Turteltaub, S. van der Zwaag. "Modelling the Fracture and Healing Behaviour of Self-healing Thermal Barrier Coatings Under Thermomechanical Cycling", ECCM/ECFD 2018, Glasgow, UK, April 2018.

3. J. Krishnasamy, W.G. Sloof, S. van der Zwaag , S. Turteltaub, "Modelling and life time prediction of self-healing thermal barrier coatings based on fatigue life methodology", 6th International Conference on Self-Healing Materials ICSHM2017, Friedrichshafen, Germany, June 2017.

4. J. Krishnasamy, W.G. Sloof, S. van der Zwaag , S. Turteltaub. "Modelling the fracture behavior of thermal barrier coatings in the presence of healing particles", Fifth International Conference on Self-Healing Materials ICSHM2015, Durham, North Carolina, USA, 2015.

5. J. Krishnasamy, W.G. Sloof, S. van der Zwaag , S. Turteltaub. "Modelling fracture in self-healing thermal barrier coatings". European Materials Research Society (EMRS), Warsaw, Poland, Sep 2015.

6. S. A. Ponnusami, J. Krishnasamy, S. Turteltaub, A. S. Farle, W. G. Sloof, Sybrand van der Zwaag, "Crack healing model for extrinsic and intrinsic self-healing materials", European Mechanics of Materials Conference (EMMC15), 2016, Brussels, Belgium.

# LIST OF FIGURES

# LIST OF TABLES